University of Oxford

Department of Materials

Engineering Plasmonic Light Scattering with Thin Dielectric Films

Towards enhanced light trapping and novel sensing elements

DPhil Thesis

1st October, 2015

Author:
Alex Powell

Supervisors:
Dr. Jason Smith
Dr. Andrew Watt
Dr. Hazel Assender

Abstract

Plasmonic research is becoming increasingly focused on the integration of noble metal nanostructures with planar devices to enhance their performance. Whilst the physics of noble metal nanoparticles at a simple interface is well studied, their behaviour inside a thin film structure is not. This work investigates the effect that placement in a thin dielectric film has on the excited modes and the directional scattering from various geometries of nanoparticle; the focus is on the fundamental principles but the application of this work in light trapping and nanoantenna design is also discussed. Research is conducted using finite-difference time-domain simulations and a custom built dark-field Fourier-space microscope, designed to interrogate individual particles and measure their angular scattering in thin films for the first time. It is found that the excited modes, large angle scattering and substrate coupling of the nanoparticles can be manipulated and improved considerably through careful choice of the materials and dimensions of the layers. Scattering from silver nanowires into a substrate is observed experimentally for the first time and an overcoating thin film is exploited to create highly directional emission, which is compared with nanoantennas in the literature. The potential to use this system as a novel sensing element is discussed. Following on from this, the nanocube patch antenna system is reviewed and its operation as a subwavelength plasmonic gas sensor is demonstrated for the first time to test for relative humidity using the Nafion polymer. This easily fabricable system shows superior sensitivities to other single-particle sensors across a range of humidities and simulations predict that by using sharper cubes and different deposition processes a further tripling of the recorded efficiency is achievable. The nanopatch structure can be readily adapted to detect a variety of other gases, and has the potential for integration into photonic circuitry.

Research Outcomes

A List of publications, conference presentations and awards associated with the work in this thesis:

Journal Publications

AW Powell, AAR Watt, HE Assender, JM Smith, *Plasmonic Gas Sensing Using Nanocube Patch Antennas*, Advanced Optical Materials, (2016), doi: 10.1002/adom.201500602

AW Powell, N Hjerrild, AAR Watt, HE Assender, JM Smith, *Directional plasmonic scattering from metal nanoparticles in thin-film environments*, Applied Physics Letters, 104, 081110, (2014)

AW Powell, MB Wincott, AAR Watt, HE Assender, JM Smith, *Controlling the optical scattering of plasmonic nanoparticles using a thin dielectric layer*, Journal of Applied Physics, 113, 184311, (2013)

Conference Presentations

CLEO2015, **Oral**, San Jose, US, May 2015, *Subwavelength Sensing Elements from Film-Coupled Silver Nanocubes*, AW Powell, AAR Watt, HE Assender, JM Smith

Photon14, **Poster**, Imperial College, UK, 2014, *Controlling optical scattering and plasmonic modes of Ag nanoparticles in thin-film structures*, AW Powell, JM Smith

Photon12 , **Poster**, Durham, UK, 2012, *Optimised plasmonic structures for thin-film solar cells*, AW Powell, MB Wincott, AAR Watt, HE Assender, JM Smith

Acknowledgements

There are many people to thank for getting me started, helping me finish and keeping me going during the course of this thesis. Firstly my supervisor Jason Smith, for providing such an excellent example of how good academic science should be conducted, for showing me how to take an idea and run with it for helping me to distinguish between a novel course of action and a dead end. Also thanks for his approachability, his continued faith in me and for fostering such a great research group to be a part of. My co-supervisors Andrew Watt and Hazel Assender were a great help thanks to their insight into polymer science and thin film photovoltaics. Hazel has improved everything I have written by immediately spotting the cracks in my arguments and forcing me to improve the clarity of my writing.

It has been such a privilege to be a part of the PNG group at Oxford: being part of such a talented, fun group of people has made the years fly by. I would like to especially thank Matthew Wincott and Phil Dolan for all their help getting to grips with Lumerical simulations, Aurélien Trichet for teaching me how to perform optical experiments and Dave Coles for helping to develop the NC sensing apparatus and for organising the trip to Sheffield. I would also like to thank all of them for being on hand to help me think through problems, read drafts and plan experiments, for all the fun extracurricular evenings and for all the extra pints when my funding had finished. Sam Johnson, Alex Robertson and Simon Fairclough have also provided invaluable advice and camaraderie over the years. The crew from Queen's College MCR, need a mention too, for making oxford outside the lab such a great town to live in.

My family have always been a backbone of support and the world would be a much lonelier place without them. My father, Dr. John Powell, taught me the joy of asking questions, and my mother Donna gave me the self-confidence to keep asking even when none were forthcoming. My siblings too have always had my back. Finally I have to thank Laura, for all the joy and the laughter, past, present and future, for all the plans and all the adventures and for all the support in harder times. My life is so much richer for you being in it.

This work is dedicated to you all.

Contents

List of Acronyms

AFM	atomic force microscope
APD	avalanche photodiode
CCD	charge-coupled device
DI	de-ionised (water)
EM	electromagnetic
Eq.	equation
FC40	Fluorinert^{TM} liquid FC-40 from 3M
FDTD	finite-difference time-domain
FIB	focussed ion beam
Fig.	figure
FP	Fabry-Perot
F_{subs}	forward scattered fraction
FWHM	full-width half maximum
LSP	localised surface plasmon
n_{air}	refractive index of the upper half-space
n_{film}	refractive index of the film
n_{subs}	refractive index of the substrate
NA	numerical aperture
NC	nanocube
NH	nanohemisphere
NP	nanoparticle
NW	nanowire
OPV	organic photovoltaic
P3HT	poly-3-hexyl thiophene
PCBM	phenyl-C61-butyric acid methyl ester
PEDOT	poly(3,4-ethylenedioxythiophene)
PLL	parrallel
PML	perfectly matched layer
PMMA	Poly(methyl methacrylate)
PRP	perpendicular
PSS	polystyrene sulfonate
PTFE AF	Poly[4,5-difluoro-2, 2-bis(trifluoromethyl)-1, 3-dioxole-co-tetrafluoroethylene]
PV	photovoltaic

PVA	Polyvinyl acetate
PVDF	Polyvinyl Difluoride
PVP	poly(vinyl pyrrolidone)
Qabs	absorption cross section
Qscat	scattering cross section
RH	relative humididy
RI	refractive index
RM	rod mirror
rms	root mean squared
RoC	radius of curvature
SEM	scanning electron microscope
SPCM	single photon counting module
SPP	surface plasmon-polariton
TEM	transmission electron microscope
TE	transverse electric
TM	transverse magnetic
TFSF	total-field scattered-field
z_-	distance from particle center to substrate
z_+	distance from particle centre to film-air interface

Chapter 1

Introduction

The explosion of new research into plasmonics over the last two decades seems to have been on one of the longest fuses in human history. It was about 1700 years between the Romans utilising the optically excited resonances of noble metal nanoparticles to make highly expensive glassware, and the development of a full theoretical description of this behaviour by Gustav Mie at the start of the last century. Close to another century was to pass before the computational and experimental tools were sufficiently advanced to make use of these surface plasmons. At the moment of writing, plasmonics research is a rapidly expanding discipline and is leading to new innovations in many diverse areas of science.

As the field matures, there is an increasing body of work towards producing plasmon-based or enhanced devices that improve upon existing designs and would be suitable for large-scale production. Many of these, such as LED's,[1–3] solar cells[4–10] and various types of sensor[11–14] will be planar devices consisting of multiple thin (< 1 μm) layers. Whilst there has been much research investigating the effect of an interface on the plasmon modes excited in metal nanoparticles, an analysis of the impact of placement within a thin-film structure is currently lacking.

The goal of this investigation is to examine the effects of a dielectric thin film environment on the mode structure and scattering properties of various geometries of

nanoparticle. This research will be conducted with a view to expand fundamental knowledge and to inform and improve the design of plasmonic devices, especially those involving light trapping or directional scattering. A nanoscale patch antenna geometry in the form of a film-coupled silver nanocube separated from a metal sheet by a thin spacer is also utilised to produce a novel subwavelength gas sensing element, which could be expanded to form a large scale metamaterial sensor or integrated into a plasmonic waveguide structure.

In the course of this introduction, the concept of a plasmon localised at the surface of a metal nanoparticle is introduced. A brief tour of some of the history of plasmonics follows, setting the scene for a discussion of the state of play at the time of writing and the motivation for this work. Finally, a description of the structure of the thesis is included to provide an overview of the work carried out.

1.1 Introducing Localised Surface Plasmons

Metal nanoparticles provide a powerful and convenient route to direct electromagnetic energy beyond the limits imposed by aperture diffraction. If one imagines the metal as an extended lattice of positive ionic cores, with an 'electron gas' of conduction band electrons which moves freely amongst them, (known as the Drude, or free electron model for metals) it is possible to gain a conceptual appreciation of why this system is so interesting.

When light is incident upon a metal particle, the force from the electric field pushes electrons to one side, polarising the particle and setting up an internal electric field which opposes this change. (Fig. 1.1(a)) If the field were to vanish at that instant the electrons would wobble back and forth at the resonance frequency of the system until damping overcame their motion. As the electric field of the incident wave is oscillating in time and space, it drives a charge density oscillation confined to the surface of the particle (since in the interior the charge of the electrons and ionic cores cancel each other) and coupled to the driving field; referred to as a localised surface plasmon (LSP).

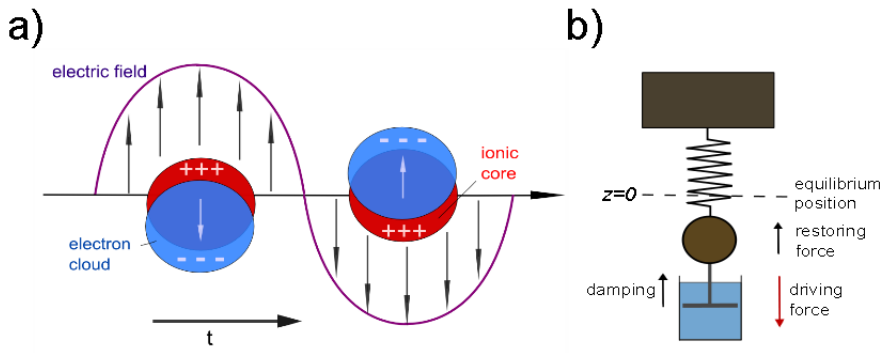

Figure 1.1: (a) Creation of localized surface plasmons by an incident photon; the force on free electrons by the photon's electric field induces a charge separation, which oscillates with the electric field of the light, creating a coupled excitation bound to the surface of the nanoparticle. (b) Highlighting the model of the dipolar mode as a damped, driven linear oscillator with the incident electric field as the driving force, the charge separation supplying the restoring force, and the collisions between electrons with the lattice and the edges of the sphere the damping.

The simplest model of this system is as a driven, damped linear oscillator, where the incident electric field supplies the driving force, the charge separation the restoring force and scattering of electrons from the surface of the particle (along with losses due to radiation) providing the damping (Fig. 1.1(b)). Although not sufficient to explain all their behaviours, this basic model provides a good foundation for understanding LSP's, and will be discussed further in section 2.1.2.

These localised surface plasmons are highly resonant and depend sensitively on the particle size, shape, material and dielectric surroundings. If the particle is made up of a highly conductive material such as gold or silver, there can be a large number of electrons involved, even for ∼10 nm particles and so a significant charge density can be supported at the surface which produces a very strong, highly localised field enhancement, sometimes orders of magnitude greater than that of the incident plane wave.[15] This field enhancement means that plasmonic particles will interact very strongly with incident light and can scatter or absorb light very efficiently. It is mainly these three behaviours: field concentration, extreme sensitivity to the surrounding environment and highly efficient scattering that has fueled the interest in LSP's across such a diverse range of fields.

Surface plasmons can also be excited in, and guided along extended metal structures

such as patterned surfaces, gratings, and strip waveguides.[15–17] These are generally referred to as surface plasmon polaritons, and form an exciting branch of research by themselves. These are discussed briefly in section 2.1.3, but this work focuses on excitations localised within single, or coupled nanoparticles and so a detailed discussion of travelling plasmons does not fall within the scope of this investigation.

1.2 A brief history of plasmons in metal nanoparticles

Colloidal noble metal nanoparticles with the ability to support LSP's can be fabricated using some very basic techniques and have been utilised for a variety of purposes over at least the last 1700 years: The Romans were able to produce some magnificent glassware which was a glowing red when held in front of a light source, and a rather ugly green otherwise, the most famous (but by no means the only) example is the Lycurgus cup (Fig. 1.2 (a) & (b)). The inset to Fig. 1.2 (a) shows a TEM image of the glass in the cup revealing gold and silver colloids of about 60 nm in size. These have a plasmon resonance in the green, so when front-lit, the green backscattering is dominant, but when light passes through the glass from behind, the plasmons *absorb* in the green, leaving a deep, rich red to glow through. This impressive specimen depicts scenes with Dionysus, the god of wine defeating an attacker, and it has been suggested that the changing of the glass from green to red was symbolic of the ripening of grapes and thus had special significance for the cult of Dionysius.[18]

The colour of these glasses depends on the precise size and concentration of the particles, which are extremely sensitive to the proportions and oxidation states of certain precursor elements, and the temperature and reaction time of the glass melt procedure.[18] We can thus surmise that the Romans were able to exercise a significant control over the nanoparticles in glassware, although they were almost certainly not aware of exactly what they were doing. The art of staining glass using metal nanoparticles was rediscovered in the middle ages, and many fantastic examples of medieval windows in churches and cathedrals, such as the one in Fig 1.2 (c), were created by adding different concentrations of gold and silver compounds to glass.[19]

Colloidal nanoparticles also have a more controversial history in medicine: In the Sixteenth Century alchemists produced solutions of gold nanoparticles with a deep blood-red colour, which were thought to have medicinal properties.[20] Even today it is still possible to buy solutions of colloidal gold and silver (Fig. 1.2 (e)) which are marketed as vaguely defined "immune-boosting supplements"[21] although these have been shown to have negative side effects such as skin discoloration[22] and are not legal in many countries.

Figure 1.2: Historical uses for colloidal nanoparticles: (a), (b) The Lycurgus cup, with illumination from the front and rear respectively. The inset in (a) shows a TEM image of the nanoparticles in the glass. (c) A stained-glass window utilising plasmonic nanoparticles. (d) Gold colloids being used as medication in the fifteenth century. (e) Colloidal silver being marketed as a cure-all today.

It was posited that the blood-red solutions and glasses contained very small gold nanoparticles as early as the seventeenth century, and this was proven by Richard Zsigmondy in the late nineteenth century.[23] It was not until a more complete understanding of electromagnetic waves and their interaction with matter was developed that eventually led to Gustav Mie solving Maxwell's equations for light scattering by metal nanoparticles in 1908, proving that the resonances present in these structures are responsible for the ruby-red colour of colloidal solutions.[24]

Throughout most of the 20th century, the field moved forward slowly. Bulk plasmons in

the form of longitudinal electron oscillations were discovered in 1950's and the existence of surface plasmons postulated soon after, although they were not discovered until the 1970's. (See Pelton & Bryant,[25] pp. xv) Around this time work on Raman scattering on rough metal surfaces produced surprisingly intense readings[26] and thus the field of surface-enhanced Raman spectroscopy (SERS) was born. Aside from this field (which remains one of the biggest success stories of plasmonic enhancement) work in plasmonics progressed only slowly, until the end of the century, when the development of better electron microscopes, improved synthesis of colloidal particles and other synthesis techniques such as electron beam lithography, enabled the creation of well controlled structures on the nanoscale which could be studied systematically. Improved computers and numerical simulation techniques complemented these developments and in the early part of the 21st century plasmonic structures started to be used in fields as diverse as light trapping for photovoltaics,[4, 5, 27], biological tagging,[11, 28] sensing[29, 30] and photonic circuitry.[31]

1.3 Motivations and outcomes

While there remains a wealth of fundamental science to explore, as the field has matured there has been a growing interest in utilising the properties of localised surface plasmons in working components and devices. One area of particular significance is to use the strong scattering efficiencies of plasmons in metal nanoparticles to redirect light into or out of planar devices, the main applications for this being antireflection coatings, light trapping for photovoltaic (PV) cells, emission enhancement for LED's and directional emission for single emitter detection and photonic circuitry. A second area which has seen a huge amount of interest is the utilisation of surface plasmons to create a new class of optical sensor, with high sensitivity, subwavelength mode volumes and fast reaction times.

Some of the key elements of these fields are outlined here briefly to provide a context and motivation for this investigation. The contributions made within this project to each field is outlined. This section is intended as an introduction only and further

discussion of the literature is included within the relevant chapters.

1.3.1 Metal nanoparticles in planar structures

In the mid-nineties, Stuart and Hall demonstrated that a layer of noble metal nanoparticles on the surface of a silicon-on-insulator photodetector led to a significant increase in the photocurrent.[32] This was attributed to the plasmons excited in the nanoparticles scattering incident light preferentially into the high-index substrate, acting as an antireflection coating and thus increasing the absorption of the device. Catchpole and Atwater[5] later showed that such particles also scatter a large fraction of normally incident light to large angles, leading to increased path lengths within the active layer, (as shown in Fig. 1.3) and further contributing to the improved absorption.

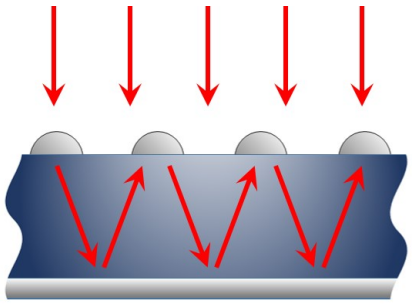

Figure 1.3: Light trapping in a solar cell - incident radiation is scattered to large angles by plasmonic particles at the surface of the cell, increasing the path length and the confinement of light within the active layer, and thus improving the absorption of the cell.

This behaviour has led to many investigations utilising an array of plasmonic scatterers for light trapping in solar cells. The antireflection effect and the increased path length in the device improves the absorption and allows for a thinner active layer, which in turn reduces carrier recombination losses.[33] This has led to many successful examples of enhanced power conversion efficiencies,[34–43] improved absorption,[7, 44, 45] and short-circuit current,[42, 46] as well as attracting significant media attention.[47–49]

This is not the entire story however: in reality, any plasmonic structures present will be sandwiched between layers in the planar stack that constitutes the finished device. For more traditional bulk Si cells this could effectively mean only a change in the dielectric environment of the particle as the layers are so thick. However, thin-film cells, attractive due to their cheap material and processing costs and made from everything from amorphous silicon,[50, 51] to polymers,[52–54] to quantum dots,[55, 56] are be-

coming increasingly popular.[57] All of these designs have been shown to benefit from plasmonic light trapping, but as the layers can be anywhere from 10 - 1000 nm thick, to understand the behaviour of plasmonic particles in these structures, the interference of incident and scattered light in the layers must be taken into account. Whilst several studies have indicated that it is possible to improve light trapping performance through selective NP placement within an existing structure, or by the use of additional thin layers,[58–60] an investigation into the mechanics behind this is currently lacking.

For applications such as single-photon detection, optical wireless communications, and photonic circuitry, it is generally highly important to be able to produce well-defined, directional emission to couple effectively between the near field of an antenna and distant sources or detectors.[61–65] The placement of dipolar emitters within a thin-film is known to alter the directionality of emission,[66, 67] although the effect on scattering from metallic particles has yet to be investigated and this could provide an easily fabricable route to increased directionality for plasmonic optical antennas.

In order to address the gap in understanding regarding the effects of thin-film structures on plasmonic nanoparticles, this investigation examines the case of individual silver NP's, within a dielectric thin-film under both white-light and monochromatic excitation. This is the first time an analysis of plasmon scattering in thin films has been carried out, and is conducted with a view to enhance fundamental understanding of this system and to provide a toolkit to aid and improve the design of planar thin-film devices containing plasmonic particles, with a focus on light trapping for solar cells and nanoantennae.

The parameter space is explored in detail using finite-difference time-domain (FDTD) simulations, numerical modelling and practical experiments. In particular a novel dark-field Fourier-space microscope is designed and constructed to observe the directional scattering from metal NP's in thin films for the first time. The effect of film thickness and refractive index, along with particle position and geometry on the excited modes and their spectral and directional scattering are examined in order to produce a complete understanding of this structure. It is found that through careful choice of

materials and film parameters, the scattering efficiency, the fraction of light scattered forwards into the substrate and to large angles leading to enhanced path length can be improved. A special focus is given to nanowires due to their ability to scatter light into a tightly confined angular range, and the utilisation of this behaviour for sensing and optical nanoantennas is investigated.

1.3.2 Novel plasmonic sensors

One of the earliest applications for surface plasmons was their use in detecting the presence of an analyte from small changes to their dielectric environment, and this is one of the few examples of a plasmonic technology that has been successfully commercialised.[68, 69] Optical sensors are generally of interest due to their fast response times, compatibility with technologies such as optical fibers and the multiple choices for signal retrieval they offer. Surface plasmons are an excellent sensing platform due to the high field concentration produced in subwavelength volumes, which makes them very sensitive to their dielectric surroundings. Whilst there has been much success in producing plasmon sensors in liquid environments, this generally relies on a refractive index change, which is often much smaller and therefore more difficult to detect in gas sensing. NP's in a matrix which interacts with a specific chemical leading to a local RI shift around the particles have shown some potential, [70–76] but require a large surface area, reducing their usefulness compared to other optical technologies. The use of localised plasmons in individual particles is attractive due to their tiny mode volumes meaning they have the potential to detect individual processes,[77] and potentially map changes with subwavelength precision.[78] There is also significant interest in creating a sensing architecture that could be integrated with photonic circuitry to produce an on-chip nanoscale sensor.[79–81]

Nanocube patch antennas can be fabricated using straightforward planar deposition techniques, can operate as a metamaterial[82] or a subwavelength element[83–85] with scope for excitation via plasmonic waveguides.[86] In the second half of this investigation the potential for a silver nanocube separated from a silver film by a thin spacer to

operate as a novel plasmonic gas sensor is explored. As a proof of concept the operation of the system as a relative humidity (RH) sensor was tested using the Nafion polymer from Dupont which expands with increasing humidity. The optical scattering spectrum was observed to shift with RH as the spacer expanded and a sensitivity was recorded which is superior to other single NP humidity sensors above ∼50 % RH, on a platform that can be adapted to detect a variety of other gases.

1.4 Thesis outline

The main body of the thesis will be structured as follows:

Chapter 2 describes the fundamental theory of localised surface plasmons in metal nanoparticles. Starting from Maxwell's equations, the free electron model of metals is introduced and used to describe the origin of bulk and surface plasmons, before focusing on localised plasmons. A simple model for dipolar charge oscillations in a uniform field will be described before introducing Mie theory and higher order terms. The effect of changing particle size and dielectric environment is discussed, as well as the excitation of Fano resonances between modes. Finally the effect of moving away from a spherical geometry of particle is introduced.

Theoretical considerations more specific to the various elements of the research in this investigation are outlined in **chapter 3**. A model detailing the effect that interference can have on dipolar emission in thin film structures is presented and its utility for plasmonic studies described. The influence of a substrate on the modes of a particle is discussed along with the formation of hybrid modes, with a focus on flatter particles. A discrete dipolar approximation is then utilised to describe the angular emission from extended particles at an interface. Finally the interaction of flat-sided particles and a metal substrate is examined in a different light and modelled as an optical patch antenna and the accuracy of this model is reviewed.

With a solid grounding of the problem at hand and the theory necessary to approach it, **chapter 4** describes the materials and methods used in the coming chapters. Finite-

difference time-domain simulations are introduced and the general theory behind these related. The polymers and particles used in all experiments are defined, along with the sample preparation techniques. The custom-designed optical microscopes created for this investigation are detailed along with the calibrations and refinements required to obtain the results of scattering from individual nanoparticles that follow.

Chapter 5 presents the results of an investigation into the effect of a dielectric thin film structure on the spectral and directional scattering properties of spherical silver particles in a dielectric thin-film. FDTD simulations, experiments and the theoretical models described in chapter 3 are used to probe the parameter space and provide a holistic description of the system which would serve as a toolkit for anyone seeking to utilise metal nanoparticles in thin-film structures. It is found that careful tuning of the parameter space can reduce backscatter and Fano losses, which is important for light trapping and antireflection applications. The structure also enables some tuning of the scattering directionality and power, which is of interest for nanoantennas and single emitter detection. The discussion focusses on the fundamental science, but the implications for potential applications, especially light trapping for photovoltaics, and optical nanoantennae are highlighted where relevant.

Building upon this framework, **chapter 6** broadens the investigation to discuss the effect of particle shape, focusing on flatter and longer particles that can be fabricated using bottom-up procedures. The effect of the film structure on the plasmon modes of Ag nanocubes and hemispheres is investigated in the near and far field using FDTD. The influence of film thickness and particle shape on the scattering directionality is also examined. The ability of wires in a thin film to scatter light into a confined angular range is compared to other methods in the literature, and suggestions are made for the utilization of a thin film structure to improve the results of several other approaches. The effect film thickness has on the angular scattering is applied to suggest a novel sensor design and some preliminary experimental results and simulations are discussed.

The last phase of this report moves away from dielectric structures and in **chapter 7** a

proof of concept investigation into the use of the optical patch antenna system described in chapter 3 as a subwavelength gas sensing element is elucidated. The chapter begins with a review of plasmonic gas sensors and then a discussion of the expansive properties of the Nafion polymer which forms the active layer of the sensor. The tunability and sensing ability of the system is investigated both as a peak shift of the resonant mode and as a variation in scattering intensity with red laser excitation. The limitations of the sensitivity are then discussed. Simulations are conducted to investigate methods to improve the sensor and future work detecting other gases and integration with photonic circuitry is considered.

Chapter 2

Localised Surface Plasmons in Spherical Particles

The aim of this chapter is to familiarise the reader with the physics of localised surface plasmons. Starting from first principles, the dielectric function of a metal is determined using the free electron model, and the origins of bulk plasmons and surface plasmon polaritons at a metal interface discussed. The idea of a localised surface plasmon, where the charge density wave is confined to the surface of a nanoparticle is introduced. By approximating the particle as small compared with the wavelength of incident light, expressions for the dipole resonance and its response to changes in environment and particle size are derived. The limits to this model are discussed, and aspects of Mie Theory are brought in to build a more complete conceptual understanding. The interference between modes to produce a Fano effect which can be observed in the directional scattering of individual nanoparticles is examined and discussed. Finally the behaviour of particles which deviate from perfectly spherical geometry is introduced. By the end of this chapter the reader should have a good understanding of the origins and behaviours of surface plasmons in spherical and nanoparticles in an isotropic medium.

Several sources have been used to research this chapter, which have been referenced throughout, but there are a few key texts that the author would recommend as further reading to expand on the physics descibed. The textbooks by Maier[15] (2007), Pelton & Bryant[25] (2013), Bohren & Huffman[87] (1998), Kumar[88] (2013) and Sarid & Challener[16] (2010) are recommended.

2.1 From Maxwell's Equations to Surface Plasmons

2.1.1 Maxwells Equations in bulk media

A classical description of the interaction between light and metal nanoparticles must have its foundation in Maxwell's equations. A classical approach is justified in this report since the high density of free carriers in noble metals results in energy levels with negligible spacing compared to thermal vibrations at ambient temperatures. From this starting point the plane wave dispersion relation and an expression for polarisability of materials will be defined. In SI units, Maxwell's equations can be written:

$$\nabla.\mathbf{D} = \rho_f \tag{2.1a}$$

$$\nabla \times \mathbf{E} = -\frac{\partial \mathbf{B}}{\partial t} \tag{2.1b}$$

$$\nabla.\mathbf{B} = 0 \tag{2.1c}$$

$$\nabla \times \mathbf{H} = \mathbf{J}_f + \frac{\partial \mathbf{D}}{\partial t} \tag{2.1d}$$

Where c is the speed of light in free space, $\mathbf{J}_f$ is the free current density and ρ_f is the free charge density in the medium. The displacement field $\mathbf{D}$ is related to the electric field, $\mathbf{E}$, and takes into account the polarisability of the materials due to free and bound charges:

$$\mathbf{D} = \epsilon_0 \mathbf{E} + \mathbf{P} \tag{2.2}$$

Where **P** is the polarisation density of the material which takes into account the permanent and induced dipole moments present. This expression highlights the relationship between the displacement field, the incident electric field and the polarization of the material, a key step to understanding the charge separations which produce LSP's. An equivalent relation, can be defined between the magnetic field **H** and the magnetic induction **B**, but as no natural materials are magnetic in the optical regime, magnetic effects are considered negligible throughout this investigation.

In the absence of any sources (moving electric charges), Maxwell's equations can be combined to produce the wave equation in a medium of permittivity ϵ:

$$\nabla^2 \mathbf{E} = \frac{\epsilon}{c^2} \frac{\partial^2 \mathbf{E}}{\partial t^2} \tag{2.3}$$

With general solutions expressed as a linear superposition of monochromatic plane waves: $\mathbf{E} = \mathbf{E}(\omega) \exp(\imath(\mathbf{k}.\mathbf{r} - \omega t))$ Running these solutions through the wave equation a dispersion relation can be obtained:

$$\mathbf{k}^2 = \frac{\epsilon \omega^2}{c^2} \tag{2.4}$$

These relations, along with appropriate boundary conditions will describe how waves behave at an interface of two media of differing ϵ. For a plane wave travelling in free space, encountering a material ϵ_1, if $\epsilon_1 > 0$ EM waves will be able to propagate beyond the interface as usual, but if $\epsilon_1 < 0$ (e.g. Ag & Au at optical frequencies) the only electromagnetic (EM) field penetrating the material is evanescent and so EM waves are not able to pass through.

For materials where some attenuation of the radiation is present, $\epsilon(\omega)$ is complex and expressed as $\epsilon(\omega) = \epsilon_1(\omega) + \imath\epsilon_2(\omega)$, which can then be used to determine the real and imaginary parts of the refractive index. For non-isotropic materials the permittivity can also take the form of a tensor. In this investigation, all dielectrics are assumed to be isotropic and non-absorbing, which is appropriate for the very thin, optically

transparent films used, and so ϵ will always have a real, scalar value.

2.1.2 The free electron model for metals

For metals, the behaviour of $\epsilon(\omega)$ can be modelled quite accurately using the assumption of the Drude, or free-electron model, in which electrons are considered a free, non-interacting gas amidst a fixed lattice of ionic cores. Bloch's theorem describes the wavefunction of such an electron as the product of the periodic potential of the lattice and a plane-wave envelope function, and the Schrödinger equation for an electron in a crystal can be shown to be equivalent to that of an electron in free space, with the slight correction that an effective mass must be defined for a given material, although in metals such as silver and gold this is very close to the free electron mass. (See Pelton & Bryant,[25] pp. 5-7)

The motion of a free electron gas, driven by an external field, with damping from collisions with other electrons and the lattice can be expressed as a damped harmonic oscillator:

$$m\frac{d^2\mathbf{x(t)}}{dt^2} + \frac{m}{\tau}\frac{d\mathbf{x(t)}}{dt} = -q\mathbf{E}(t) \tag{2.5}$$

Where m is the effective mass for an electron, τ is a decay time which accounts for electron scattering and $\mathbf{E}$ is the total electric field generating force in the material including contributions from external fields and internal polarizations created by these. Since an electron will be induced to motion by a driving field, $\mathbf{E}(t) = \mathbf{E}(\omega)\exp(\imath(-\omega t))$, any induced polarization will oscillate at the same frequency, and the position of an electron (assuming the field is polarized along the x-axis) can be described: $\mathbf{x}(t) = \mathbf{x}(\omega)\exp(\imath(-\omega t))$. Putting this through the oscillator equation of motion (Eq.2.5) gives:

$$x(t) = \frac{q\mathbf{E}(t)}{m(\omega^2 + \imath\omega/\tau)} \tag{2.6}$$

This electron motion induces a polarization density, $\mathbf{P}$ in the bulk metal as there is a charge separation of the negative electrons from the positive cores:

$$\mathbf{P}(t) = -qx(t)N \tag{2.7}$$

Where N is the free electron density. From the expression relating polarization to displacement field, (Eq. 2.2) the Drude form of the dielectric function of a free-electron metal can be determined:

$$\epsilon_r(\omega) = 1 - \frac{\omega_p^2}{\omega^2 + \imath\omega/\tau} \tag{2.8}$$

Where the bulk plasma frequency is defined as:

$$\omega_p = \sqrt{\frac{q^2 N}{\epsilon_0 m^*}} \tag{2.9}$$

Here m^* is the effective mass of electrons in the metal and ω_p can be understood as the natural frequency of free oscillations in the electron sea, if we assume that all electrons move in phase. A quanta of these oscillations is named a *plasmon*, or specifically in this case a *bulk* plasmon, which distinguishes it from the surface plasmon polaritons described in the next section. For large frequencies, $\omega\tau >> 1$ and using eq. 2.4 the dispersion relation for bulk plasmons can be written:

$$\omega^2 = \omega_p^2 + c^2 k_x^2 \tag{2.10}$$

These oscillations share many properties with density waves found in gaseous plasmas, hence the name, although since the density is much higher in metals than a gaseous plasma, so too is the natural frequency. Bulk plasmons take the form of compression waves of free electrons in the metal, and cannot couple to transverse electromagnetic waves due to their longitudinal nature as shown in eq. 2.10, and are only excited through

the impact of high energy electrons.[15]

This model only describes free electron behaviour, and in gold and silver there are transitions between the d-band and the conduction band which are extremely significant in determining the dielectric function of the material, leading to significant differences between the measured and Drude values for $\epsilon(\omega)$ at optical frequencies, as shown in Fig. 2.1. These transitions result in additional damping to plasmon resonances, and can be described using an extension of the Drude approximation where atoms are modelled as damped, driven oscillators with certain natural frequencies, $\omega_{0,i}$, which approximate the interband transitions. Away from these values, the restoring force is practically zero and the model is the same as the Drude model. Any number of transitions, i can be described in this way and the general form for the dielectric constant is written:

$$\tilde{\epsilon}_r(\omega) = \tilde{\epsilon}_\infty(\omega) - \omega_p^2 \sum_i \frac{f_i}{\omega_{0,i}^2 - \omega^2 + \imath\omega/\tau_i} \tag{2.11}$$

Where f_i is the oscillator strength of the i^{th} transition and $\tilde{\epsilon}_\infty$ is a constant used to account for the offset produced by resonances at frequencies outside the region of interest.

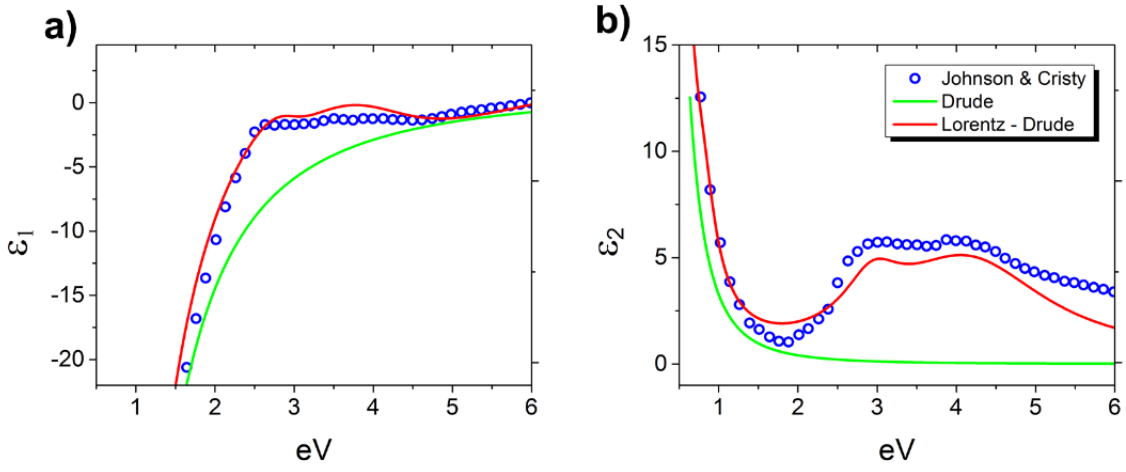

Figure 2.1: The real, a) and imaginary, b) components of the dielectric function of gold as calculated using the Drude (green line) and Lorentz-Drude (red line) models, produced using the code produced by Ung et al.[89] Measured results (blue circles) calculated from Johnson and Christy.[90]

In figure 2.1(b), it can be seen that the metal (gold in this case) has very strong absorption at low energies, and moderate absorption at higher energies due to inter-band transitions, with a 'window' in between. At low energies, where the response of the material is not affected by inter-band transitions, and can be considered as metallic, the free-electron approximation is a good fit to the data. In regions where transitions occur, the model of the atoms as damped, driven oscillations described in Drude-Lorentz gives a good fit. The dielectric function helps define the energy of the plasmon resonances of a metal structure, as discussed in the next two sections. Interband transitions occur at different energies for different metals, and it turns out that silver has the largest window in the optical regime with minimal absorption loss, which makes it the most efficient metal for optical plasmonics although gold is often used due to its greater chemical stability.

2.1.3 Surface plasmons at planar interfaces

The termination of a bulk metal by an interface with a dielectric medium results in the formation of charge oscillations which are strongly bound to the surface. These 'surface plasmons', or more correctly 'surface plasmon polaritons' (SPP's), still take the form of longitudinal electron density waves, although in contrast to volume plasmons these are coupled to the electromagnetic field of incident light, hence the 'polariton' in the name. SPP's propagate along the metal-dielectric interface and their electric field decays exponentially with distance from this boundary.

Figure 2.2 shows an interface in the $x-z$ plane at $z = 0$ between a metal with dielectric constant $\epsilon_m(\omega)$ and some dielectric $\epsilon_d(\omega)$ upon which is launched an SPP propagating in the $x-$direction. By considering a wave propagating along the metal surface and applying boundary conditions for an interface, the dispersion relation for a transverse magnetic (TM) SPP can be found (see Maier[15] pp 21-30 for a complete derivation) which takes the form:

$$k_x^2 = \frac{\epsilon_d \epsilon_m \omega^2}{(\epsilon_d + \epsilon_m)c^2} \tag{2.12}$$

Expressions for a dispersion relation in the z-direction can also be used to show that k_z is imaginary in both directions and thus the field along this axis decays exponentially from the interface. The propagation length for a travelling SPP can be determined from the imaginary component of the dielectric function of the metal. Repeating this procedure for a transverse electric (TE) polarised wave demonstrates that no surface modes can exist at this polarization.

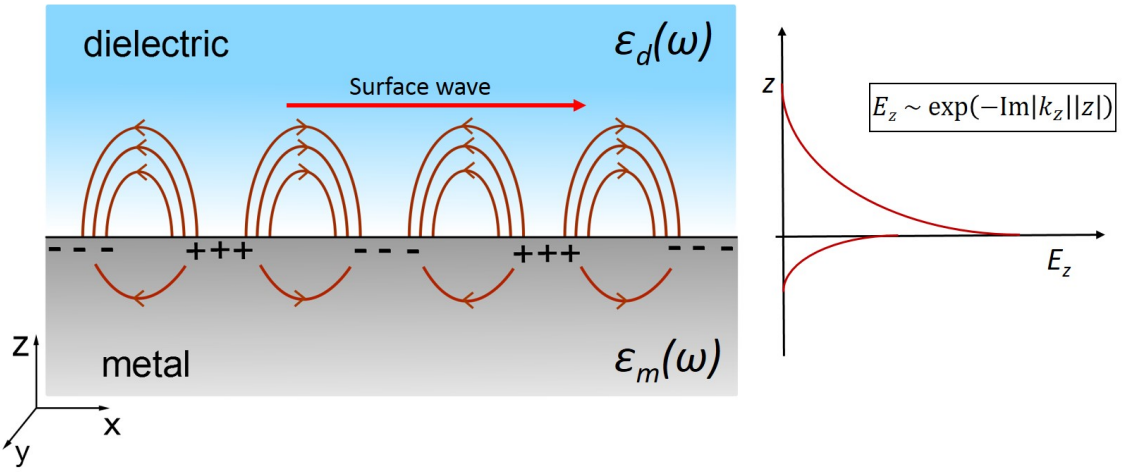

Figure 2.2: Showing the form of a surface plasmon polariton at the interface of a metal and a dielectric. A coupled electron density/EM wave propagates along the interface with the electric field decaying exponentially away from the interface into both materials.

It can be seen by comparing equations 2.4 & 2.12 that for $k_x, \omega > 0$ there will always be a momentum mismatch between a plane wave in free space and surface plasmon. Therefore SPP's at a bare, planar interface cannot be exited by direct illumination and a means to overcome the momentum mismatch is required, which is often provided by a surface roughness or grating structures.[16, 88]

2.2 Plasmons confined in individual particles

Bulk plasmons can be excited in the interiors of metals by particle injection, and when the material is terminated at an interface, illumination can excite tightly bound surface

plasmons which propagate along the surface with the help of some texturing to overcome the momentum mismatch. For an individual nanoparticle, the geometry of the particle provides the required momentum, but the excited plasmons are not propagating as there is nowhere for them to go - they are confined to the surface of the NP and reflected between the edges. Thus in discrete nanoparticles the plasmon waves excited are standing waves, which possess discrete resonances depending on the geometry of the particle.

2.2.1 Spherical particles and the quasistatic approximation

The simplest nanoparticle is a homogenous, isotropic metal sphere, of radius a. If it is assumed that a is small, it can be stated that the electric field from an incident plane wave with electric field, $\mathbf{E}(t)$ is constant across the entirety of the particle, so there is a time dependence to the field about the NP, but no spatial variation across its volume. This is referred to as the quasi-static approximation (QSA), and is appropriate for small particles where the radius $d \sim 0.01\lambda$, but can also provide useful insight into the behaviour of larger particles.

To describe the behaviour of a particle under incident illumination, expressions for the electric field both inside and outside the particle must be found and the Laplace equation for the potential, $\nabla^2\Phi = 0$ solved. The geometry of the situation is described in Fig.2.3. For a driving field polarized along the z-axis the electric potential, $\Phi = -Ez$, or in polar co-ordinates, $\Phi = -Er\cos(\theta)$. The solutions to Laplace's equation are spherical harmonics, which have the general solution:

$$\Phi_{in}(r,\theta) = \sum_{l=0}^{\infty} A_l r^l P_l(\cos(\theta)) \tag{2.13}$$

inside the sphere where $r < a$ and :

$$\Phi_{out}(r,\theta) = \sum_{l=0}^{\infty} B_l r^{-(l+1)} P_l(cos(\theta)) - E_0 r cos(\theta) \tag{2.14}$$

outside, where $r > a$. Here l defines the order of the mode, A_l, B_l are mode order dependent coefficients and P_l are Legendre polynomials: solutions to Laplace's equations using spherical boundary conditions. Here Φ_{in} is the potential of the net charge separation in the particle, and Φ_{out} is the sum of the driving field and the field produced by the internal potential, accounting for charge screening by the surrounding medium, represented by the amplitude B_l.[15]

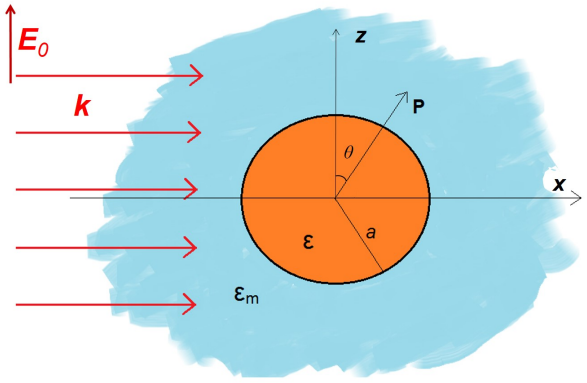

Figure 2.3: Showing the geometry used for quasi-static calculations. A homogeneous sphere in an isotropic environment is placed into an electrostatic field that varies temporally but not spatially, which induces a polarization in the sphere.

At the surface of the sphere, the tangential component of the electric field and the radial components of the displacement field, **D** are constant, allowing expressions relating A and B to be found and to solved for various orders of l. As the incident field is independent of positon, it can only couple to the first-order, dipolar mode and so for $l = 1$:

$$A_1 = \frac{-3\epsilon_d E_0}{\epsilon_m + 2\epsilon_d}, \qquad B_1 = \frac{(\epsilon_m - \epsilon_d)E_0 a^3}{\epsilon_m + 2\epsilon_d} \tag{2.15}$$

There is no $l = 0$ term as this would represent a net charge of the particle. Higher order terms that appear when the field is not equal across the particle diameter are not explained by the quasistatic approximation.[15]

It has been stated that B_l describes the amplitude of the field in the surrounding medium produced by the induced charge separation in the sphere. Since LSP's are due

to a concentration of charge at the surface, the dipolar moment of the charge separation can be written:

$$\mathbf{p} = 4\pi\epsilon_0\epsilon_m a^3 \frac{\epsilon_d - \epsilon_m}{\epsilon_m + 2\epsilon_d}\mathbf{E}_0 \tag{2.16}$$

Introducing the concept of the polarizability, α where:

$$\mathbf{p} = \epsilon_0\epsilon_m\alpha\mathbf{E}_0 \tag{2.17}$$

The polarizability, α is found to be:

$$\alpha = 4\pi a^3 \frac{\epsilon_d - \epsilon_m}{\epsilon_m + 2\epsilon_d} \tag{2.18}$$

This is a key result and shows a similar form to the Clausius - Mossotti relation, which describes the polarizability of a system of two homogenous materials with different dielectric constants.[15, 25] This arises from acknowledging that the local field is the sum of the driving field and the polarization of both the dielectric *and* the metal sphere (the so-called Lorentz field). It is clear that the polarizability has a resonance condition of $\epsilon_d = -2\epsilon_m$, defined exclusively by the dielectric constants of both the sphere and the surroundings. This is known as the Frölich condition. There is therefore a strong dependence of the resonance wavelength on the dielectric surroundings, which is what makes these LSP's so interesting for sensing techniques.

One of the most interesting consequences of this resonantly enhanced polarization is the concomitant enhancement in the efficiency with which a metallic nanoparticle will scatter and/or absorb light. This is due to the strong electric field of the separated charges allowing the NP to interact with the field of incident radiation much more strongly than an unpolarised particle of equivalent cross-section. By considering the electric and magnetic fields of the induced dipole, the absorption, scattering and overall extinction cross sections can be derived from the dipole moment and the Poynting vector

of these fields:[91]

$$Q_{scat} = \frac{k^4}{6\pi}|\alpha|^2 = \frac{8\pi}{3}k^4a^6\left|\frac{\epsilon_d - \epsilon_m}{\epsilon_m + 2\epsilon_d}\right|^2 \tag{2.19a}$$

$$Q_{abs} = k\,\mathtt{Im}\,[\alpha] = 4\pi k a^3\,\mathtt{Im}\left[\frac{\epsilon_d - \epsilon_m}{\epsilon_m + 2\epsilon_d}\right] \tag{2.19b}$$

$$Q_{ext} = Q_{scat} + Q_{abs} \tag{2.19c}$$

In these expressions the absorption scales with a^3, or the volume, V and the scattering scales with a^6, or V^2. The scattering scales with the square of the volume as scattering is a dual process involving the absorption and then re-emission of the light. For small particles, absorption dominates the extinction, but this will be overtaken by scattering as the primary extinction mechanism as particle size increases.

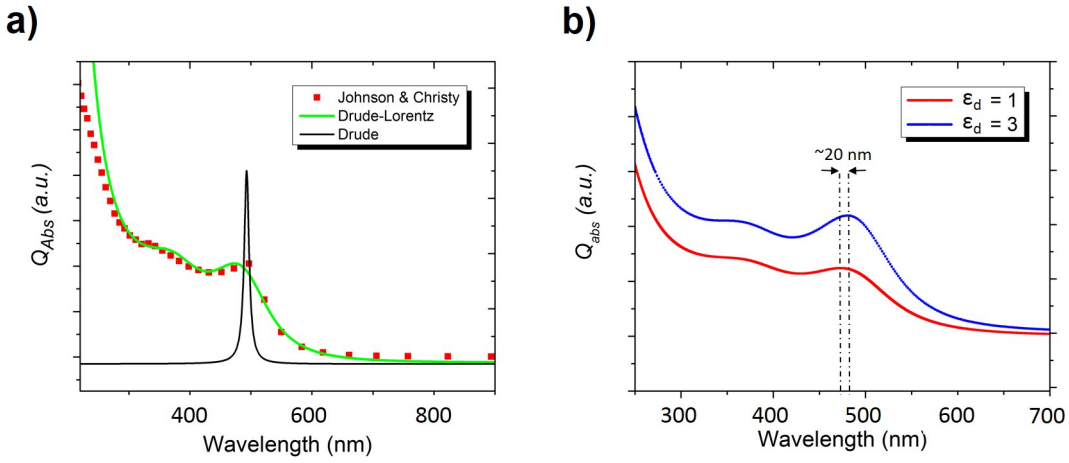

Figure 2.4: (a) The Absorption cross section of a 20 nm gold nanoparticle calculated using the quasi-static approximation with dielectric values for the metal taken from the Drude and Drude-Lorentz approximations and from experimental data. (b) Absorption cross-section calculated using Drude-Lorentz values for different dielectric media surrounding the particle.

In Fig.2.4(a) the absorption cross section for a 20 nm Au NP in free space is plotted using ϵ_m values determined from the Drude approximation (equation 2.9), the Drude-Lorentz method (equation 2.11), and experimental values taken from Johnson and

Christy.[90] It can be seen that the Drude method predicts the correct wavelength for the plasmon resonance of the particle, although it greatly overestimates its strength. The experimental values and the Drude-Lorentz method show good agreement, and show that as well as the plasmonic peak around 500 nm, the dominant feature for shorter wavelengths is the strong interband absorption, which can be problematic for applications such as plasmonically enhanced solar cells.

Figure 2.4 (b) shows the impact of changing the dielectric surroundings of the particle. Since the absorption scales with k, and $k \sim \sqrt{\epsilon_d}$, there is a general increase in the absorption cross section across the spectrum. The second effect is that the increase in ϵ_d signifies an increase in the polarizability of the surrounding medium, which results in a reduction of the restoring force of the plasmon oscillation inside the particle, leading to a reduction in resonance frequency, or a redshifting as can be observed.

In summary: Using a simple model of a metal as a free electron gas amongst a fixed lattice of ionic cores, an understanding of how the electrons interact with incident light to create surface plasmons has been reached. Describing the particles as small compared to the wavelength of incident light, it is possible to explain many of their scattering behaviours, including the increasing significance of scattering compared with absorption for larger particles, redshifting of the peak with increasing dielectric constant of the surroundings and the impact of metal choice on the dipolar peak.

This understanding of the optical behaviour of the NP's is a good description for small spherical particles, and can be used to understand several trends that will affect particles of all shapes and sizes. However, this is far from the entire story and there are effects associated with larger particles that are not accounted for in this model. For large particles, short wavelengths and/or high-index materials, the assumption that $a << \lambda$ does not hold, and so there will not be a constant electric field amplitude across the particle, so higher order spherical harmonics will be excited and a more complete description is required.

2.2.2 Mie theory and higher order terms

In one of the most important papers of the 20th century, Gustave Mie presented in 1908 a complete theory of the scattering and absorption of electromagnetic radiation by a metal sphere, which takes into account the spatial dependence of the electric field, leading to the excitation of higher order terms, and phase retardation within the particle. Starting from Maxwell's equations in spherical co-ordinates, an incident plane wave is written in terms of spherical harmonics, and the degree to which these overlap with the spherical harmonic modes supported by the geometry of the particle is calculated.[92] Mie theory is a far-field technique and measures the net change of energy as light traverses the particle, and so in this case it is scattering and extinction that are determined directly. Thus we can obtain expressions for the cross-sections as: [87]

$$C_{ext} = \frac{2\pi}{|\mathbf{k}|^2} \sum_{L=1}^{\infty} (2L+1)\, \mathtt{Re}\left[a_L + b_L\right] \tag{2.20a}$$

$$C_{scat} = \frac{2\pi}{|\mathbf{k}|^2} \sum_{L=1}^{\infty} (2L+1)\left(|a_L|^2 + |b_L|^2\right) \tag{2.20b}$$

$$C_{abs} = C_{ext} - C_{scat} \tag{2.20c}$$

Where a_L and b_L are functions describing how the Ricatti-Bessel functions of the geometry (for a spherical harmonic order L) interact with the electric and magnetic components of an incident plane wave due to the free-space wavelength and refractive indices of both the particle and the surrounding medium. The overall cross-section is a summation over all the resonant excitations, L, which draws together the different harmonics: $L = 1$ is a dipole, $L = 2$ is a quadrupole etc. Choosing only $L = 1$ in the summation brings us back to a similar expression to the quasi-static approximation described in equation 2.19a, with a slight alteration to account for radiation

damping.

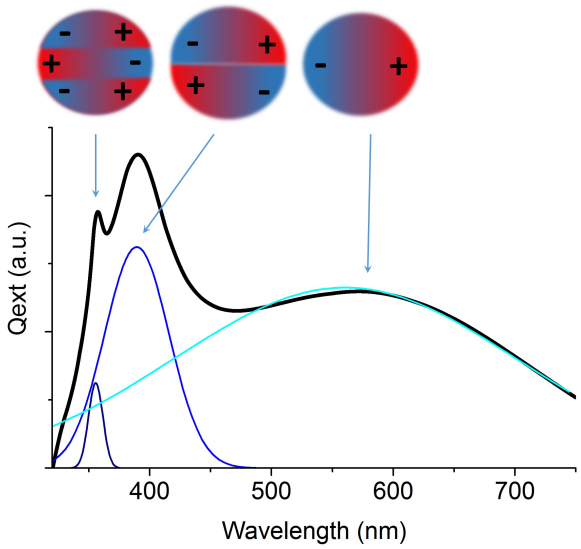

Figure 2.5: Scattering cross-section spectrum for a 150 nm silver nanosphere in air. The contributions from individual modes determined from curve fitting and sketches of the electron charge distribution for each mode are also shown.

Mie theory takes into account that the particle will occupy a finite space and will not experience a uniform field. Different wavelengths will excite different resonant modes in the NP according to its geometry and these will each make their own contribution to the extinction characteristics. This is highlighted in figure 2.5 which shows the calculated extinction (absorption + scattering) cross sections for a 150 nm nanoparticle, highlighting the individual excited modes which make up the overall pattern and displaying the charge distributions associated with each mode.

Mie theory provides a complete description of the absorption and scattering properties of spheroidal nanoparticles in isotropic media, as well as describing their far-field angular scattering behaviour. In this regard it is an absolute triumph, and one of the cornerstones of plasmonics and nanotechnology in general. However, in this investigation, we are interested in the behaviour of a variety of particle shapes, often in quite complex environments, and it is therefore more expedient to use other, more versatile numerical methods. The majority of the simulations in this thesis have therefore been conducted using Finite-Difference Time-Domain (FDTD) software, the basics of which are described in chapter 4. Thus a more in-depth discussion of the origins of Mie the-

ory is not appropriate here and we move instead to look at some of the implications of this theory. For a full derivation of equation 2.20 the reader is referred to Bohren & Huffman[87], or to some excellent and lively discussions in the more theoretical theses of Burrows[93] and Trügler.[94]

2.3 The plasmonic parameter space

Whilst the mechanics of Mie theory will not be discussed, it is worthwhile examining its predictions as to how altering the parameter space of a spherical NP in an isotropic medium affects the plasmon resonances. This is the simplest case imaginable and so is worth considering before moving on to more complex scenarios in future chapters. At present, the resonances are dependent on: particle size, surrounding dielectric, and choice of metal.

2.3.1 Particle size

Particle size is an extremely important parameter for determining the spectral behaviour of noble metal nanoparticles. For particles smaller than ∼50 nm, altering the size has a limited effect on the restoring force and mainly affects the damping.[95] As the particle size increases, dissipative losses, largely due to scattering of the free electrons at the particle perimeter, are reduced, therefore the damping is lessened and the resonance peak is seen to become stronger and narrower, resulting in the scaling factors observed in equation 2.19a.

As particle size increases, additional retardation mechanisms such as dynamic depolarisation and radiation damping become significant[96, 97]. Dynamic depolarisation occurs when the particle size is such that the conduction electrons across the particle no longer move entirely in phase, which leads to a reduction of the overall polarisation[98] and eventually produces non-dipolar charge separations. This dephasing causes a weakening of the restoring force and thus a movement of the plasmon resonance to lower frequencies, redshifting the extinction peak with increasing particle diameter.

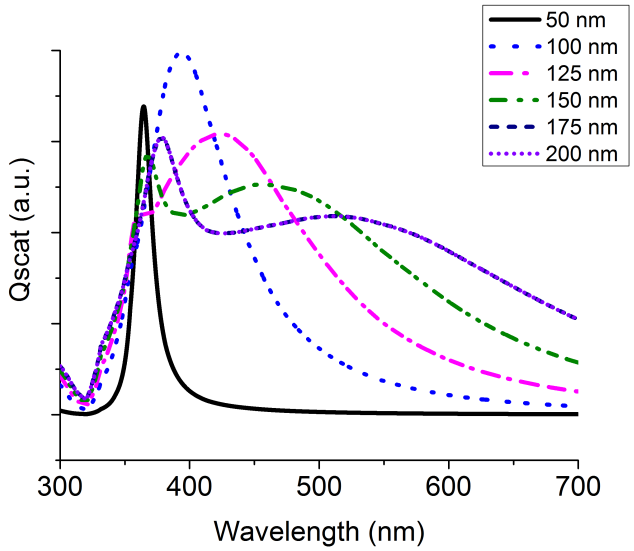

Figure 2.6: Scattering cross-section of silver nanoparticles in air with varying diameter, showing the redshifting and broadening of the dipolar peak as particle size increases as well as the excitation of higher order resonances.

As equation 2.19a showed earlier, scattering becomes increasingly important for larger particles. Scattering represents a re-radiation of the energy that was used to excite the LSP and so a loss of vibrational energy for the plasmon; referred to as radiation damping. As the particle size is increased the scattering increases and therefore the radiation damping until an equilibrium is reached. This creates a broadening of the resonance peak, along with some loss in magnitude, leading to weaker scattering cross sections across a greater portion of the solar spectrum. Figure 2.6 demonstrates these effects - for smaller particles, increasing the size increases the scattering peak, whereas for larger NP's a strong redshift is seen due to dynamic depolarisation and the peaks weaken and broaden due to radiation damping. It is clear from fig. 2.7(a) that altering the size of an NP, affects higher order peaks in a similar way to the dipolar contribution, although the size sensitivity is reduced as the mode order increases.

The peak radiative efficiency (figure 2.7(b) which describes how much of the light that interacts with the particle is scattered, compared to the total extinction, increases with NP size and tends toward unity as the scattering ($\sim a^6$) comes to dominate absorption ($\sim a^3$). Once again, this increases slightly slower with size for high order modes compared with a dipole as small changes in size are less significant for larger particles.

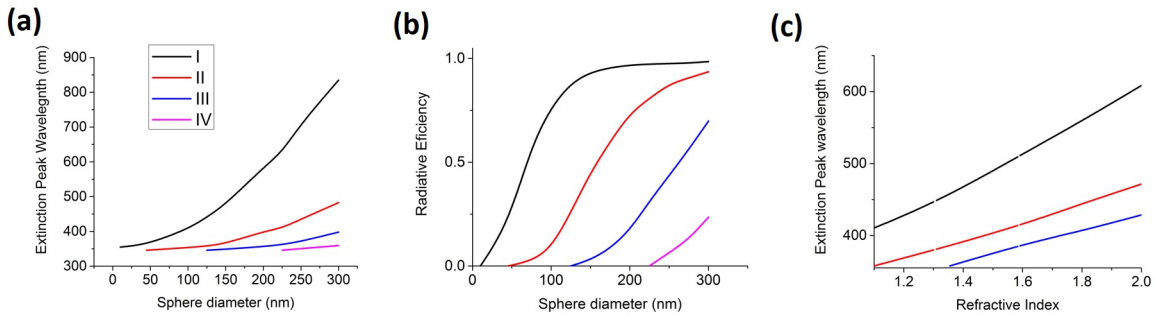

Figure 2.7: Effect of the diameter of an Ag sphere in free space on (a) the resonance wavelength and (b) the radiative efficiency of the dipolar (I) and higher order modes. (c) Effect of the refractive index of the surrounding dielectric on the resonance wavelength of a 100 nm sphere.

Surrounding media

Equation 2.18 describes how the field around a NP is dictated by the polarisability of both the particle and its surroundings. When a charge separation is induced in the particle, the medium surrounding the particle will polarise to oppose the particle's field, thus reducing the net polarisation and the restoring force. Materials with a higher dielectric function (refractive index) will polarise more strongly, creating a greater reduction in the restoring force and therefore the resonance peak will redshift as the refractive index of the particle's environment increases.[95] Figure 2.7(c) shows that higher order modes respond to RI changes in a similar manner to the dipole, but once more show themselves to be more resilient to changes in their surroundings. An increase in the dielectric constant surrounding the particle will also result in a reduction of the wavelength in that media and an increase in the relative size of the particle, and thus the damping effects described in the previous section will also be observed.

Particle Material

The plasmonic response of a MNP is dictated by the dielectric functions of the particle and that of the surroundings. For the majority of common dielectric environments, only certain metals achieve the condition $\epsilon = -2\epsilon_m$ needed to sustain a surface plasmon resonance around the optical spectrum. This limits the choice of metals down to quite a small number, although more work is being done on alloying and multi-layered NP's

to try and expand upon the restrictions that this creates.[99–101]

Another deciding factor in the material choice is the non-plasmonic processes that may lead to loss of efficiency, the most significant of these being interband transitions between the d-band of a noble metal and the conduction band. These behave much like the bandgap in semiconductors and can even lead to a weak photoluminescence in bulk metals.[102] They are even more important in confined structures- since as the number of atoms is reduced, these bands become more defined and absorb light more effectively.

Due to its dielectric properties, silver will support the strongest plasmon resonance in the optical regime but is often replaced by gold in many applications due to its greater chemical stability. However, gold suffers badly from absorption due to interband transitions across a large part of the spectrum, (see Fig. 2.4) which compromises its usefulness in many applications[103]. Silver also suffers from some interband losses that can damage performance, but there are far less significant in the visible region than for gold. Aluminium behaves quite differently to the noble metals due to increased interior damping and displays lower, broader peaks[104], but also much less absorption at short wavelengths, for which it is becoming a popular choice for enhancements in thin-film solar cells.[105–107]

2.4 Fano resonances in Mie Theory

In systems where scattering occurs due to both a background process across a broad spectrum, and a resonant process at a discrete energy, interference between the two amplitudes produces an asymmetric lineshape known as a Fano resonance. This behaviour is observed in many quantum and classical systems and is a fundamental property of coupled oscillators.[108] The amplitude of the background continuum varies slowly with increasing energy, whilst the amplitude of the discrete process is small except for near the resonant energy, where it spikes rapidly and undergoes a phase shift of π as the resonance is crossed. This dramatic phase shift leads to constructive and destructive

interference between the two states at either side of the resonance energy, producing the characteristic asymmetrical lineshape.

As can be seen in Fig. 2.5, the different modes of a spherical NP can fulfill the requirements for Fano resonances to occur, as each angular momentum channel produces very different amplitudes and line widths. In most cases the broad dipolar mode behaves as a continuum and the quadrupole as the discrete resonance, although for large NP's or a high RI environment, the quadrupole can also act as the continuum and interfere with higher order terms as shown in Fig. 2.8(b).

From the description of particle scattering from Mie theory in equation 2.20(b), it is clear that the overall scattering is a sum of the intensities of the various resonances and interference between modes will not be observed in the total scattering efficiency of a solid, spherical NP. It is worth noting that this *can* be observed in total scattering for more complex particles such as nanoshells, where the hybridisation of modes between the two edges of the shell (see section 3.3) can produce the required interference.[109] For the NP's considered here, an observable that is sensitive to interference must be chosen. The most obvious solution is to examine the efficiency with which a particle scatters light forwards and backwards with respect to the direction of the exciting radiation.

The backwards and forwards scattering cross sections are (Bohren and Huffman[87]):

$$Q_{BS} = \frac{2\pi}{|\mathbf{k}|^2} \left| \sum_{L=1}^{\infty} (2L+1) (-1)^L [a_L - b_L] \right|^2 \tag{2.21a}$$

$$Q_{FS} = \frac{2\pi}{|\mathbf{k}|^2} \left| \sum_{L=1}^{\infty} (2L+1) [a_L + b_L] \right|^2 \tag{2.21b}$$

Where the $(-1)^L$ term in C_{BS} and the summation of terms before squaring in both cases allows for the interference between modes. Both terms are plotted as a function of driving frequency in Fig. 2.8(a).

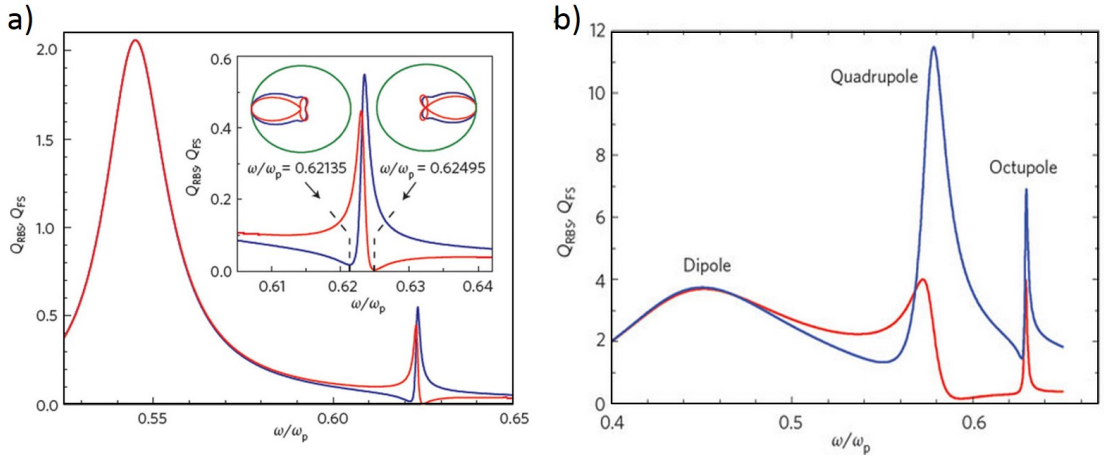

Figure 2.8: Adapted from Luk'yanchuk et al.[110] (a) Radar back scattering efficiency (Q_{RBS}; red) and forward scattering efficiency (Q_{FS}; blue) cross-sections versus normalized frequency ω/ω_p calculated using equation 2.21. The dielectric permittivity ϵ is described by the Drude formula. The size parameter, $q = 0.7$, where $q = \omega a/c$. Inset shows polar scattering diagrams near the quadrupole resonance of a plasmonic particle. Red lines shows linearly polarized light; blue lines represent non-polarized light. (b) Radar back scattering (red) and forward scattering (blue) cross-sections versus normalized frequency with the larger size parameter of $q = 1.7$.

The inset to Fig. 2.8(a) displays the asymmetric Fano lineshapes about the quadrupole resonance, showing a dramatic change in the directionality of the scattering about this wavelength. In Fig. 2.8(b) it can be seen that for a larger particle, interference between the higher order terms also has the same effect. This behaviour has been studied in detail by Luk'yanchuck et al.[110–112] who calculated the energy flow about the particles to further explain this behaviour. They found that the interference between incident and scattered radiation generated a complex near-field pattern with singular points and optical vortices which lead to either strong enhancement or suppression of the electromagnetic nearfield at different locations around the particle, amounting to constructive and destructive interference in the forward and backwards scattering observed in the farfield.

Forwards and backwards scattering is difficult to observe for single particles in a uniform environment, but has been observed in various investigations for substrate supported NP's.[113–115] Fano resonances in plasmonic structures are currently of great interest in biological sensing, metamaterials and nonlinear plasmonic devices.[116] Many plasmonic light trapping studies have observed a drop in forward scattering around the

quadrupole,[27, 39, 41, 98, 117, 118] which, coupled with this mode's weaker radiative efficiency makes it very difficult to achieve any enhancements at shorter wavelengths. The backscattering produced by Fano resonances can therefore be a significant source of loss and a way to mediate this behaviour would be extremely beneficial for plasmonic light trapping.

2.5 Non-spherical particles

The shape of a plasmonic nanoparticle is a key parameter for determining the behaviour of the LSP's excited within it. Changes in geometry result in changes in the polarizability of the metal structure, producing changes in the restoring force, which will affect the plasmon resonance. The concentration of the electric field due to the plasmon excitation will be affected by the particle shape, which dictates its sensitivity to changes in its surroundings. Chen et al. found that particles with sharper edges had significantly greater sensitivity to a change in the surrounding refractive index than round NP's.[119] This can be explained due to the 'lightning rod effect' where electric fields are more highly concentrated for high aspect ratio particles, which can be derived from the quasistatic approximation. (For further reading see Maier[15] or Bohren & Huffman[87])

Most shapes with a high degree of symmetry (which tends to be the case for wet synthesized particles, with the notable exception of triangular nanodisks[78, 120]) tend to support at least a dipole and a quadrupole mode, although the relative strengths of each can be enhanced or suppressed by the particle geometry as will be seen in section 6.1. This investigation is mostly concerned with the way in which particles interact with a substrate and a thin-film structure, which is discussed in detail in the next chapter and in chapter 6 and so further discussion about the general effects of particle shape will be analysed in terms of their interaction with the substrate. For further reading on this topic, the reader is referred to the work of Kelly,[97] Chen[119] and Mock,[121] or the book chapter by Rivera et al.[122]

2.6 Conclusions

This chapter has presented an overview of the physics and behaviours of localised surface plasmons. Starting from Maxwell's equations, the Drude free-electron model was derived and the excitation of bulk charge oscillations, and surface plasmons at a metal interface inferred. To investigate localised surface plasmons, standing electron waves inside a particle were considered using the quasistatic approximation. This simple model produces an excellent description of the plasmonic behaviour of small particles, and can be used as a conceptual guide for many of the trends observed in larger NP's. Mie theory was introduced as a numerical method to effectively describe plasmon behaviour in spherical particles leading to a discussion of the effect of radiation damping and dephasing and the behaviour higher order modes, including the Fano resonances which arise due to interference between modes and can be observed in the directional scattering. The effect of particle shape was introduced at the end of the chapter.

All of the models in this chapter have described the behaviour of plasmonic nanoparticles in isotropic media. Whilst there are many uses for metallic NP's in liquids, especially in many biological applications, the focus of much plasmonic research (including this project) is based around NP's in planar structures. Thus the effect of substrates and other surroundings must be taken into account, as it will be seen that these can influence the plasmonic behaviour profoundly. The next chapter will build upon the work presented here to describe the effect of substrates and more complex planar environments on the mode structure and scattering behaviour of a variety of particle shapes.

Chapter 3

Models of dipoles in films and particles at interfaces

Placing a metal nanoparticle in any environment that differs from the perfectly transparent and isotropic dielectric described in the last chapter will have a marked effect on the way the particle interacts with incident illumination. This introduces a whole new parameter space which is only beginning to be explored and made use of. NP's at interfaces and in thin films are of especial interest and as the following chapters demonstrate, placement within a thin film can lead to scattering properties that could benefit a variety of applications.

This chapter aims to introduce and describe the tools needed to investigate the effect of a thin-film structure on plasmonic scatterers. It begins with a description of the effect of a thin-film on directional emission from a dipolar charge separation and how this has been used to improve light collection from single emitters. The dipole approximation is expanded to consider the emission properties of long particles such as wires. The chapter then moves beyond the single mode to discuss the effect of moving particles near to an interface and the formation of hybrid modes, with a focus on flatter particles and nanocubes. Firstly the effect of a dielectric is considered and then a metal surface.

Finally, the behaviour of silver nanocubes as optical patch antennas is discussed in detail.

3.1 Dipole emission in multilayered structures

It has long been known that the radiation pattern of an electric dipole is modified when in close proximity to a dielectric interface. This effect was first investigated by Sommerfeld[123] at the start of the twentieth century in order to understand the emission pattern of a radio antenna located close to the earth's surface. There has been a recent revival of interest in this problem in fields such as quantum computing and metrology, where directional emission into well defined modes is crucial due to the low photon count for the single emitters generally used in these applications.[124]

To achieve this directionality, it was suggested by Koyama[125] to place dipolar emitters at the interface between a low and a high index dielectric; due to the higher optical density of states, most of the light would be channeled into the high index material in a well defined radiation pattern - so the structure would act like a kind of optical antenna. This achieved some success, with 86% of light coupled into the high-index layer, but this was still not sufficient for usage in most high-sensitivity quantum applications.

It did however help initiate the interest in light trapping for photovoltaics: an array of silver nanoparticles positioned above the active layer was found to reduce the reflection for high index layers like silicon and gallium arsenide and increase the path length of light in the substrate and thus enhance the absorption of the cell.[5, 60] The dipolar mode (or similar hybrids which will be discussed in section 3.3) is generally utilised for this purpose due to its higher radiative efficiency[104, 126] and many arrays are designed to minimise the excitation of the more strongly absorbing high-order modes.

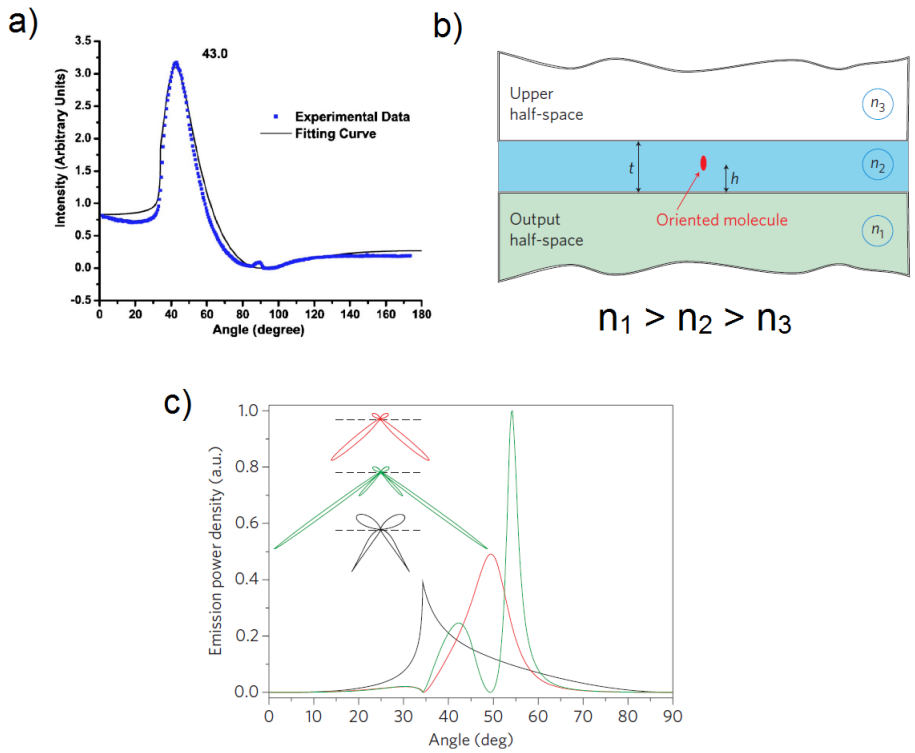

Figure 3.1: a) Reproduced from Luan et al. (2006)[67] The radiation pattern for randomly distributed dye molecules in a PMMA layer above a high index lens. b), c) Reproduced from Lee et al. (2011)[66]. The structure devised by Lee et al. and the radiation pattern for (black line) a dipole at a distance of 5 nm from an air-sapphire (n=1.787) interface, (red & green lines) dipoles in the structure shown in b) with middle layer thickness, t=350 nm and 600 nm, respectively.

The impact of thin-films on fluorescent dipolar emitters has also been investigated. Luan et al.[67] found that spin coating dye molecules in a thin PMMA film onto a high index hemispherical lens produced a highly structured radiation pattern (figure 3.1a), which depended strongly on the thickness of the film. This effect was utilised by Lee et al.[66] who aligned dipolar emitters perpendicular to the interfaces in a thin PVA film above a high index substrate, as shown in figure 3.1b). The refractive index of the substrate was 1.787 and the film 1.492. The upper layer is air with n=1. The emission pattern is extremely sensitive to the thickness of the films above the molecules, as shown in figure 3.1c). The aim of this structure is to get single emitters to radiate strongly into the structure within a well-defined pattern, and using a thickness of 350 nm a 96 % collection efficiency was achieved.

3.1.1 The origins of altered radiation patterns

This section examines the interference due to reflection and refraction of light emitted by a dipolar source placed within a thin film structure such as that used by Luan and Lee, and the effect this has on its angular scattering properties. Ways in which this behaviour could be advantageous for photovoltaic light trapping and nanoantenna applications are also discussed. Much of the work describing the mechanics of this system was produced by Lukosz,[127, 128] and Neyts[129] and the description here follows their methods closely.

For a dipole in a layer in an arbitrary multilayered stack, we can write the total power, F supplied by the dipole (including that lost to absorbing media) at a given wavelength as:

$$F = \int_0^\infty K(\kappa)\, d\kappa^2 \tag{3.1}$$

Where κ is the component of the wave-vector in the plane of the layer and K is the power density per unit $d\kappa^2$. This power density can then be converted into power density per solid angle, then re-arranged to find the power density as a function of the angle from the normal, α :

$$P_+(\alpha) = \frac{k_+^2 sin\alpha_+}{\pi} K_{+,T}(\kappa) \tag{3.2}$$

Here $K_{+,T}$ is the power transmitted (not absorbed) into the upper half-space. With an appropriate choice of input parameters this relation will produce directional emission plots such as those seen in Figure 3.1.

For a situation where the dipole is located at distances z_+ and z_- from the interfaces of the emitting medium of thickness t, as shown in figure 3.2, the power density takes the form:

$$K_{\pm,T}(\kappa) = \sum A \left[\frac{\beta^2}{k^3 k_z} \frac{(1 \pm a_+)(1 \pm a_-)}{1 - a} \right] \tag{3.3}$$

Where k_z is the component of the wavevector inside the film oriented along the z-axis, A is a constant and β is equal to a component of the wave vector, both are dependent on the dipole orientation. $a_\pm$ are the Fresnel reflection coefficients for each interface, referenced to the location of the dipole antenna in the layer: a_+ relates to interference due to reflection from the upper (film-air) interface and depends on the distance to this interface from the dipole centre, z_+. Equally, a_- refers to the lower interface. These values can be written:

$$\begin{aligned} a_\pm^{TM,TE} &= r^{TM,TE} exp(2jk_z z_\pm) \\ a^{TM,TE} &= a_+^{TM,TE} a_-^{TM,TE} = r^{TM,TE} r^{TM,TE} exp(2jk_z t) \end{aligned} \tag{3.4}$$

Equation 3.3 takes a different form for TM and TE emission for emitters perpendicular or parallel to the plane of the structure. For a dipole at an alternate orientation, or a random array, the final K value will possess a component from both orientations.

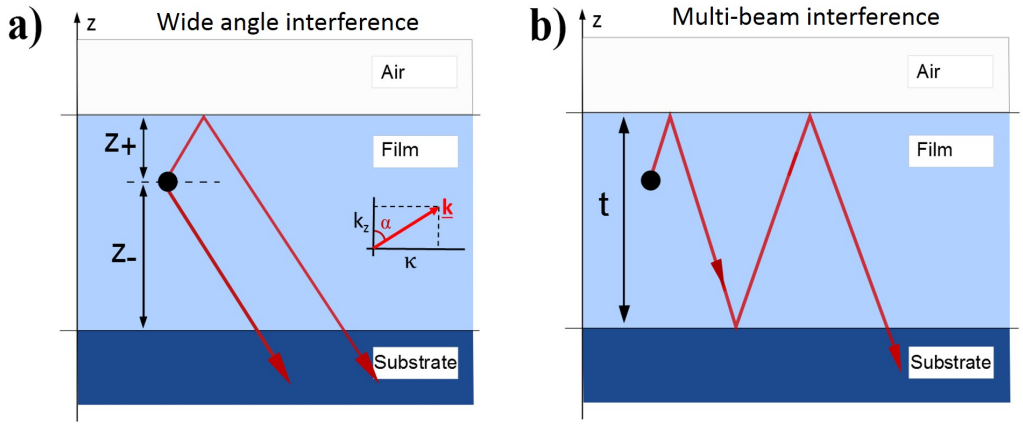

Figure 3.2: Structure of a light-emitting thin-film device illustrating the two major interference mechanisms in a multi-layered structure that dictate the radiation pattern outside the structure. The k-vector of a plane wave with a contribution k_z parallel to the z-axis and κ parallel to the layers is also shown. The dipole is located at a distance z_- from the interface at the substrate side of the film and z_+ from the interface at the air side.

This equation contains the effect the quasi-cavity has on the radiative properties of the system, concentrated in the $\frac{(1\pm a_+)(1\pm a_-)}{1-a}$ term, which represents the interference effects of the layers. As shown in figure 3.2, there are two types of reflective interference present: wide-angle interference (Figure 3.2a) between directly emitted and reflected light with the same k-vector, and multiple-beam interference, from radiation that is repeatedly reflected between two surfaces (Figure 3.2b). The wide-angle interference given by the $(1 \pm a_+)(1 \pm a_-)$ term can be seen to be strongly dependent on the properties of each interface and the distance of the emitter from this interface, whereas the multiple beam interference, described by $\frac{1}{1-a}$ in equation 3.3 is more dependent the overall thickness of the emitting layer.

For the power density emitted into the substrate, where $n_{air} < n_{film} < n_{subs}$, it can be demonstrated that wide angle interference due to reflections from the film-air interface is the dominant interference mechanism, and the transmitted power follows the relation:

$$K_{subs,T} \propto |(1 \pm a_+)|^2 \propto 1 + r^2 + 2rcos(2k_{film}z_+cos(\alpha)) \tag{3.5}$$

showing that the interference for light emitted into the substrate is dependent only upon angle, wavelength, the refractive indices and the distance from the air-film interface. Thus the refractive index of the layers and the thickness of the films can be used to effectively tune the angular scattering, which is discussed in detail in chapter 5. The only part of the relation which is altered by the thickness is the $cos(2k_{film}z_+cos(\alpha))$ term, which dictates the relationship between angular dipolar emission/scattering and the height of the film above the particle. Figure 3.3(a) shows the evolution of this term for a dipole aligned parallel to the interface, whilst 3.3(b) shows the complete interference term from eq. 3.5, from $z_+ = 0$ nm, equivalent to a bare interface, in which case there is no contribution from the film, up until $z_+ = 500$ nm, showing an increasing number of interference minima and maxima at large angles with increasing z_+, leading to the increasing number of lobes seen in the angular scattering in Fig. 5.10, which will be important for tuning the directivity and light trapping behaviour of light

scattered from metal nanoparticles in chapters 5 & 6.

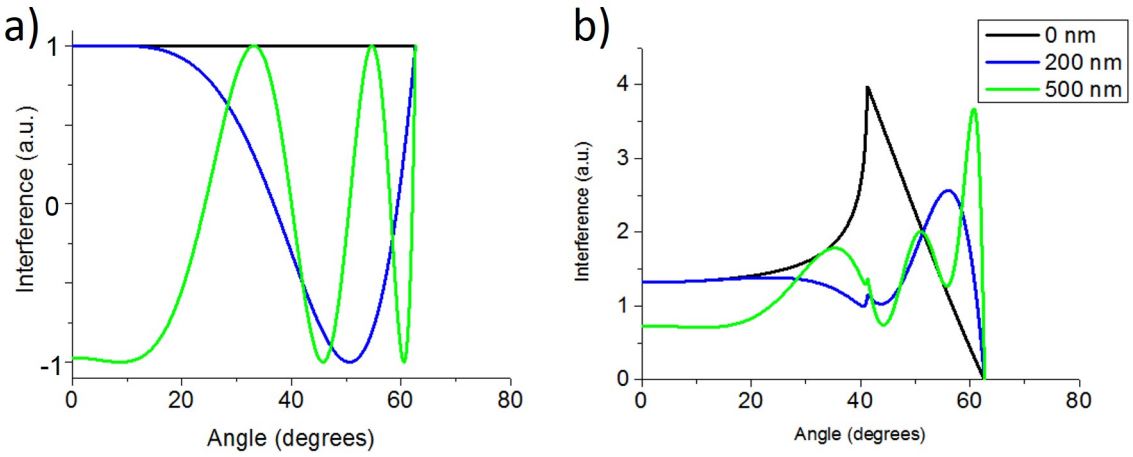

Figure 3.3: Showing the partial (a) and complete (b) thickness-dependent interference term for wide-angle reflection for z_+ = 0 - 500 nm (z_- = 50 nm).

From this model, the effect of the layer properties on the directional emission of a dipole in a thin film can be seen, and the mechanisms controlling the angular scattering patterns understood. The dipolar mode is generally the most radiatively efficient and thus of the most interest for light trapping applications. However, as will be described in section 3.3 in many particles near an interface the mode produced is a hybrid and the electric field of the resonance is not identical to that of a dipole. There can therefore be some deviation from this model, but description of the interference from a dipole in a thin-film structure is useful to explain many of the trends observed in chapters 5 & 6. Alongside an understanding of the excited modes of a NP from Mie theory in the last chapter, this model forms an important part of the toolkit for a conceptual understanding of the effect a thin-film structure has on the behaviour of surface plasmons in metal nanoparticles.

3.2 Plasmons in nanowires

Nanowires (NW's) are an interesting geometry because the extension along one axis allows them to support both SPP modes and LSP modes depending on the method and polarisation of excitation. As well as being of significant fundamental interest, this leads

to a number of potential applications, and the plasmon modes of NW's have been the subject of numerous recent experimental and theoretical reports.[130–133] The ability to wet synthesise NW's has led to explorations of their use as plasmon waveguides for optical circuitry, potentially reducing the need for more difficult top-down synthesis, although finding a facile way to position them remains a problem. NW's have been coupled to nanocrystals and used as optical antennas,[62, 64, 65, 134] been coupled to plasmonic and photonic waveguides[79, 135] and utilised in light trapping for PV.[136] Some of their unique far-field scattering properties have been explored theoretically[133, 137] and experimentally;[137–139] in free space and at a bare interface, but the influence of more complex environments has not yet been researched.

This investigation is principally concerned with the directional scattering properties of NW's and so in this section the modes excited in a wire for different incident polarisations will be detailed, and a model describing their far-field angular emission will be presented.

Considering a nanowire in free space, with light incident at 90^o to the axis of the wire: when the polarisation is also perpendicular to the axis (PRP polarisation), there is a charge separation along the length of the nanowire, as shown in Fig. 3.4(a), equivalent to an extended dipolar separation or a line of dipoles oriented perpendicular to the axis with negligible spacing between them.

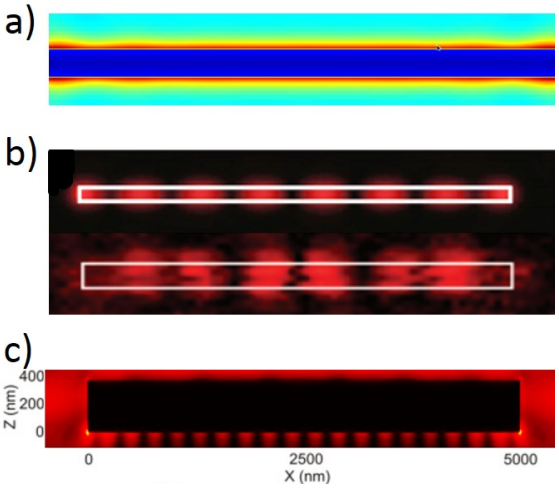

Figure 3.4: (a) Simulated electric field around a 100 nm thick NW for PRP excitation. (b) From Dorfmüller et al[130]: Simulated magnitude (top) and measured modes (bottom) for 1270 nm long, 40 nm thick wires with PLL excitation in a SNOM configuration. (c) From Miljković et al[133]: simulated electric field intensity for thick (320 nm) nanowires supported at an air-glass interface.

The more interesting case is shown in Fig. 3.4(b): Here the incident radiation is polarized parallel (PLL) to the axis of the wire, which leads to an excitement of SPP waves along the wire's length. For NW's more than a few hundred nanometers

long, the dipolar mode will now be deep in the IR or the microwave spectrum; in the optical regime standing wave modes are observed along the length of the wire. In this case the nanowire behaves like a Fabry-Perot (FP) cavity for plasmons, and in Fig 3.4(c) resonances can be observed at wavelengths corresponding to FP mode orders along the length of the wire. For PLL polarisation, the plasmon modes can be thought of as a line of dipoles oriented parallel to the wire axis.

The representation of nanowires as a set of equivalent point dipoles (the discreet dipole approximation) arranged in a line the same length as the wire was used by Sersic et al[137] to obtain a theoretical description of the radiation pattern. For normally incident light, the dipoles representing each volume element are excited in phase, with equal incident amplitude and equal polarisation, dictated by the incoming radiation. The slight phase difference in the far field from the emission of these dipoles due to their geometric separation leads to an interference effect, which is represented in the far field by multiplying the dipole radiation pattern by a form factor dictated by the wire dimensions.

The equation for a spherical wavefront is:

$$\mathbf{E}(\theta,\phi) = \frac{E_0 e^{ikr}}{r} \tag{3.6}$$

Where E_0 is the initial amplitude, and r is the distance from the point source. It has been shown that the back aperture field of a high-NA, aplanatic objective can be taken as the field on a sphere of radius f, the focal length of the objective.[140, 141] So if the wire is divided into elements $\mathrm{d}x$, $\mathrm{d}y$, $\mathrm{d}z$, and each element is considered to be a dipole; the field on the reference sphere centered about the middle of the wire can be written:

$$\mathbf{E}(\theta,\phi) \sim \frac{\mathbf{E}_{dip}^{far}(\theta,\phi)}{f} \sum_{i=1}^{n} \mathrm{e}^{ikr_i} \tag{3.7}$$

Where $\mathbf{E}_{dip}^{far}(\theta,\phi)/f$ is the electric field amplitude from the radiation pattern of a single

dipole and r_i is the distance from each volume element to the surface of the reference sphere. If we consider the case of an infinitely thin wire of length L, oriented along the y-axis, we can write $r_i = f - \frac{\mathbf{k}}{k_0}.\mathbf{y}_i(y)$ where $\mathbf{y}_i(y)$ is the distance along the wire for a length element i. Equation 3.7 can then be written:

$$\begin{aligned}\mathbf{E}(\theta,\phi) &\sim \mathbf{E}^{far}_{dip}(\theta,\phi)\frac{e^{ik_0 f}}{f}\int_{-L/2}^{L/2} \mathrm{e}^{ik_y y}\,\mathrm{d}y \\ &= \mathbf{E}^{far}_{dip}(\theta,\phi)\,.\,\mathrm{sinc}(k_y L/2)\end{aligned} \tag{3.8}$$

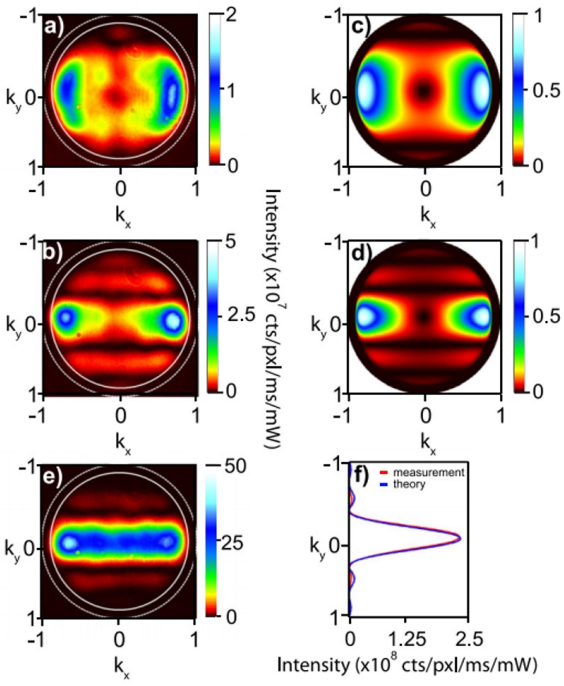

Figure 3.5: From Serisic et al.[137]: (a) Fourier space image of light scattered away from the substrate by a 1μm long, 50 nm wide and 30 nm thick Au nanowire excited by p-polarized incident light. (b) Fourier space image of a 2μm NW excited by p-polarized incident light. (c, d) are calculated radiation patterns of 2μm and 1μm NW's respectively. (e) Fourier space image of a 2μm NW excited by s-polarized incident light. (f) An average cross-cut of (e) along k_y (red curve) agrees well with the calculated sinc^2 behavior (blue line)

So the measured intensity of the NW scattering in the far field is equal to that of a dipole, w.r.t. its polarisation relative to the wire axis multiplied by a sinc^2 function. This has been demonstrated experimentally by Sersic et al, showing good agreement with the model (Fig. 3.5) but only for short NW's and in this case the wires were excited evanescently using TIR from the substrate side, so only light scattered *away* from the substrate was detected. The light scattered into the substrate by a NW was investigated for the first time simultaneously by the Author[142] (see section 6.2) and Demichel et al[139] who probed scattering from light and dark modes for different length NW's by shaping the excitation beam.

This behaviour has the potential to be used in conjunction with the thin-film interference described in the previous section. Combining interference effects due to the

phase difference in the far-field from different elements of a NW, with the interference produced by a thin film structure would result in an excellent level of control over the directional scattering of light by plasmonic nanostructures and is investigated further in section 6.2.

3.3 Hybrid modes and particles at dielectric interfaces

The modes excited in spherical nanoparticles all arise as a consequence of the natural harmonics of the particle geometry. The mode resonances can be tuned by altering the particle size and surrounding environment. Metal nano*shells* have long been another particle geometry that has attracted significant interest since the ratio of the inner and outer radii provide a new parameter for mode tuning. Prodan et al[143] modelled the complex geometry of the nanoshells as a superposition of a metal sphere and a cavity in an infinite metal volume, as shown in Fig. 3.6.

In the shell geometry, the modes produced are therefore superpositions of those of the cavity and the sphere, and there are charges on the inner and outer surfaces of the metal coupled across the metal shell. These can take either the symmetrical 'bonding' form, where inner and outer charges move together, or an asymmetrical 'antibonding' mode when they are π out of phase, and there is a significant energy difference between the two.

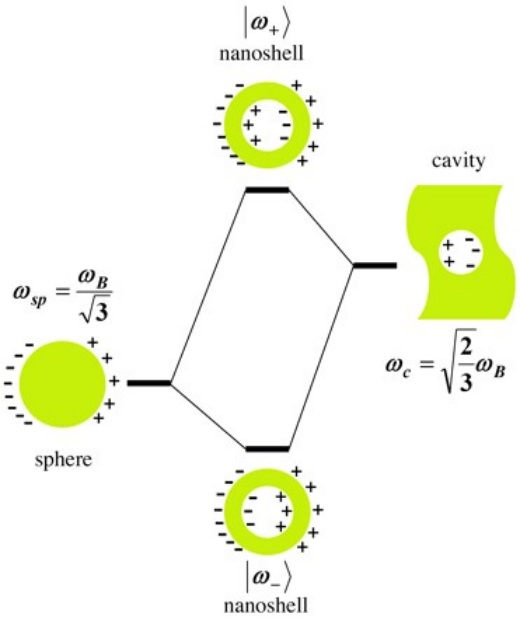

Figure 3.6: Reproduced from Prodan et al:[143] An energy-level diagram describing the plasmon hybridization in metal nanoshells resulting from the interaction between the sphere and cavity plasmons. The two nanoshell plasmons are an antisymmetrically coupled (antibonding) $\omega+$ plasmon mode and a symmetrically coupled (bonding) $\omega-$ plasmon mode.

In this case the spherical symmetry of the particle is maintained, the modes still form an orthogonal basis set and there is

no interaction between mode orders of different angular momentum l, so dipolar oscillations will only hybridise with dipoles, quadrupoles with quadrupoles etc.

The situation becomes significantly more interesting when a particle is positioned near to an interface. In this instance the charge separation in the NP induces an *image* charge in the substrate, which acts to screen the original charge separation in the particle, leading to a reduction in the restoring force and a redshift of the peaks. The image dipole in the substrate has a polarisation:[17]

$$\mathbf{p}_{im} = -\mathbf{p}_{dip}\frac{\epsilon_{subs} - 1}{\epsilon_{subs} + 1} \tag{3.9}$$

And the screening electric field produced can be found to be reduce with the cube of the distance from the centre of the nearest charge separation (not necessarily the centre of the mode) to the substrate.

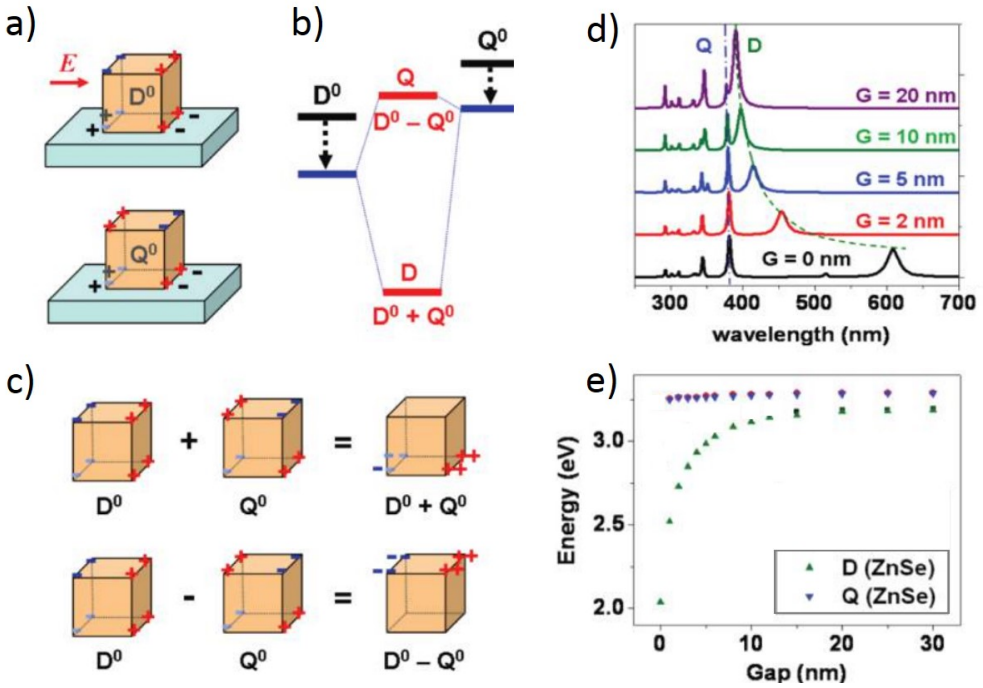

Figure 3.7: Adapted from Zhang et al.[114] (a) Schematic illustrating the substrate-mediated $\mathbf{D}^0$ and $\mathbf{Q}^0$ interaction. (b) Energy diagram showing the substrate effect: pure dielectric screening effect (dashed black) which causes red shifts of both modes and the substrate-mediated interaction (thin blue line) resulting in hybridized bonding $\mathbf{D}$ and antibonding $\mathbf{Q}$ modes. (c) Schematic charge distributions of fully hybridized modes $\mathbf{D} = \mathbf{D}^0 + \mathbf{Q}^0$ and $\mathbf{Q} = \mathbf{D}^0$ - $\mathbf{Q}^0$ (d) Modelled extinction spectra of an individual Ag nanocube (36 nm) on a ZnSe substrate (RI $\sim$ 2.6) for different cube-substrate separations, (G). (e) Energy of the dipolar ($\mathbf{D}$) and quadrupolar ($\mathbf{Q}$) modes as a function of G.

The excitation of an image charge in the substrate also results in the creation of different multipolar charges in the co-ordinate system of the particle. For modes with the same azimuthal symmetry, m (i.e. modes that have been polarised along the same axis), the same image charge will appear in the film, which mediates interactions between these modes that would otherwise be forbidden, leading to hybridisation.[144] In a cube, for normally incident light polarised parallel to the upper face, the quadrupole and dipole modes have the same symmetry on the bottom face of the cube, as shown in Fig. 3.7(a), and so will induce the same image charge in the substrate. Due to its separation from the substrate, the charge distribution on the upper face will have but a negligible effect on the image charges except for in very small cubes (< 10 nm).[114] Thus in the presence of a substrate, both modes have an equivalent multipolar symmetry about the lower edge, which removes the orthogonality of the basis set and mediates an interaction between modes, producing bonding and antibonding modes within the cube focused about the substrate and upper face respectively, as shown in Fig. 3.7(b) & (c).

The excitation of these modes has been described analytically[144] and observed in simulations and experiments.[145] This interaction is especially significant for flatter particles, due to their increased proximity to the substrate and the excitation of new modes has been observed to be significantly more pronounced here than for rounder spheres and nanoshells.[113, 146, 147] Many investigations have focused on nanocubes as a highly symmetric system readily fabricable via wet synthesis.[148]

Due to the differing proximities of the hybrid modes to the substrate, the charge screening will affect them differently and the bonding mode on the lower face will experience a much greater reduction in its net polarisation and so will redshift strongly. Figure 3.7(d) & (e) shows the formation of hybrid modes as a silver cube approaches a high index substrate, and the subsequent redshifting of the lower face mode (D) whilst the upper mode (Q) is hardly affected. For some separations, the spectral and physical overlap of modes produces a Fano resonance (as described in section 2.4) with a very narrow line width which has been suggested for use in sensing applications.[114]

The mode hybridisation model provides a good understanding of the excited modes in

particles near a substrate, but whilst there is continued interest in the mode behaviours of flat particles above dielectrics, there has been little work examining their directional scattering behaviour. (Chen et al investigated back scatter from Au nanorods at an interface with several metals and dielectrics,[149] but not the more structured emission into the substrate.) The models discussed here, along with an understanding of the mechanisms driving the directional emission of dipoles in thin film structures from section 3.1 and the effect of Fano resonances in section 2.4 will be utilised in chapter 6 to produce a holistic description of the way different particle geometries scatter light in thin-film structures with a view to using this information to improve light trapping designs, as well as exploring their use as novel sensors and optical antennas.

3.4 Nanoscale patch antennas

The greatest electric field enhancements due to LSP's generally occur in nanostructures with sharp corners or with a nanometer scale gap between elements.[29, 150, 151], Since many applications for surface plasmons such as increased fluorescence, Raman scattering and sensing depend on this field enhancement, it is highly desirable to fabricate structures with the greatest possible increase in electric field. Very sharp particles are difficult to fabricate, and can be highly polarization sensitive.[13, 152] Nanoparticle dimers are also extremely difficult to produce, as they require either highly precise top-down, lithographic or FIB-milling methods or rely on random aggregations from wet synthesis, with extremely low yields.[150] In the previous section, the coupling of a particle to its own image when placed above a substrate was discussed. When the substrate is a noble metal this forms a system with very similar plasmonic properties to a dimer, but with the advantage that it can be fabricated using planar deposition techniques, which are well developed, and previous studies have demonstrated monolayer control over the spacing between the film and the NP.[83, 153, 154]

Studies investigating spherical NP's above a metal surface have found that a sub-angstrom sensitivity to spacer thickness can be observed in the spectral scattering for extremely thin ($\sim 1nm$) spacer layers.[153, 154] This sensitivity quickly diminishes

for thicker films however, which limits the choice of spacer material and deposition technique. The excited modes are extremely sensitive to polarisation and incident angle and require TM polarized light at an oblique angle to be strongly excited.[154, 155] The properties of flat particles above a metal substrate are of considerable interest as they form a cavity mode between the particle and the metal substrate. The cavity resonances have a completely different structure to those of the film coupled sphere, with a higher sensitivity to gap thickness across a much wider range, whilst remaining highly stable across a broad range of incident angles.[82, 83, 156, 157] This allows for a much broader choice of material for the gap and also broadens the range of experimental geometries that can be used to excite these modes.

This geometry bears many similarities to that of a patch antenna: a system well-known in microwave technology. These consist of a patch, usually rectangular, of highly conducting metal fed by a transmission line and sitting a height h above a metal ground plate, separated by a dielectric spacer with a dielectric coefficient ϵ_d as shown in Fig. 3.8. The simplicity, low profile and ease of fabrication of these devices has made them very widespread, especially in the mobile phone industry.

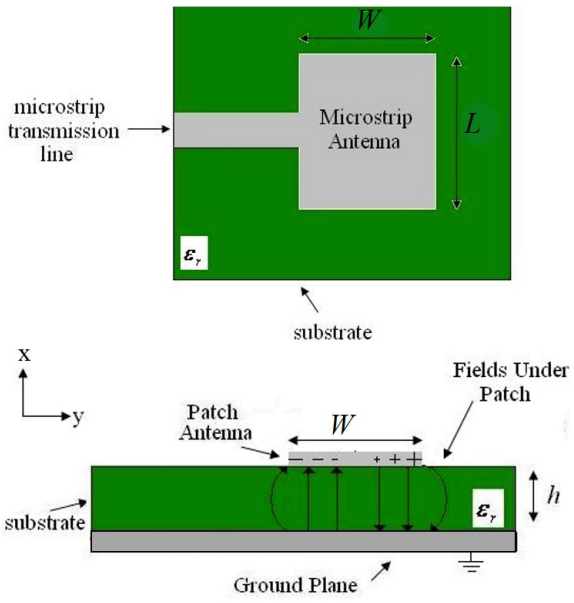

Figure 3.8: Adapted from Ref. [158] - Geometry of a conventional Microstrip (Patch) Antenna as shown from above and from the side with charge polarisation and E-fields shown underneath.

The antenna is excited with an alternating current via the transmission line and the signal is reflected at the end, setting up a standing wave in the patch. For the fundamental mode, this produces a positive and negative potential at either end which is mirrored in the ground plane. Typically the separation of patch and plane is considered to be of negligible importance as long as h is significantly smaller than the resonant wavelength, but larger than $\sim 0.05\lambda_{res}$.[158] The transverse width of the patch PRP to the transmission line controls the input impedance for feeding the antenna and can affect the bandwidth of operation. The resonance wavelengths of the system are chiefly determined by length of the side parallel to the transmission line, W of the patch and can be written approximately:

$$\lambda_{res} = 2m\sqrt{\epsilon_d}W \tag{3.10}$$

Where m is the mode order. The radiation of the antenna is due to the fringing fields, which, near the surface of the patch have E-field components along the y-axis in the positive direction at both ends, as can be seen in Fig. 3.8, which add up in phase and couple to the far-field with a k-vector primarily perpendicular to the antenna.

This description of the patch antenna is applicable to any wavelength as long as the patch and the ground plate behave as good conductors. For a normally incident wave, polarised across the width of a square patch, if the metal at both sides is considered a perfect electrical conductor and the edges perfect magnetic conductors, beneath the patch the electric field can be seen to only have a component along the normal, and so can be said to be transverse magnetic, equivalent to a TM^x_{010} mode. Considering the fundamental mode where there is a dipolar charge separation in the patch, mirrored in the metal film, the electric and magnetic fields can be expressed:

$$\begin{aligned} E_x(x,y,z) &= E_0 \cos\left(\frac{\pi y}{W}\right) \\ H_z(x,y,z) &= H_0 \sin\left(\frac{\pi y}{W}\right) \end{aligned} \tag{3.11}$$

This neglects the effects of fringing fields for now, although they can be brought in later if desired. The modes are shown in Fig. 3.9(a).

This mode structure is independent of h due to the assumption that there is no loss in the metals, leading to the mode being uniform in the x direction. This is questionable for metals at optical wavelengths, as there are numerous channels of absorption as discussed in the last chapter; silver and gold could be considered as lossy dielectrics in the visible regime, especially at the blue end of the spectrum as shown in Fig. 2.1. However, as shown by their plasmonic properties these metals still support strong surface currents over the relevant length scales and thus can still be considered optical patch antennas[82], but the boundary conditions and therefore eqn. 3.11 must be adjusted to account for the field penetration into the metal.[159] This is achieved through dividing the mode into propagating elements in the gap and evanescently decaying elements in the metal. Assuming both metals are infinite for now, we can assume the magnetic field solutions:

$$\mathbf{H} = \begin{cases} \hat{z}H_z^I e^{\kappa x} e^{-jk_y y} & x < -h/2 \\ \hat{z}H_z^{II} \cos(k_x x)\, e^{-jk_y y} & -h/2 < x < h/2 \\ \hat{z}H_z^{III} e^{-\kappa x} e^{-jk_y y} & h/2 < x \end{cases} \tag{3.12}$$

Where H_z is the amplitude of the field in each metal or in the gap, $k_x = \sqrt{k_y^2 - k_0^2}$ and $\kappa = \sqrt{k_y^2 - \epsilon_m'(\omega) k_0^2}$. ϵ_m is the dielectric coefficient of the metal. The gap is considered to be free space with $\epsilon_d = 1$ in this instance. The electric fields can be found using:

$$\nabla \times \mathbf{H} = j\omega\epsilon_m(\omega)\mathbf{E} \tag{3.13}$$

Which produces modes which are still equivalent to the TM_{010}^x modes from the patch antenna, but with an x dependence which more closely fits observations from simulations shown in Fig. 3.9(b).

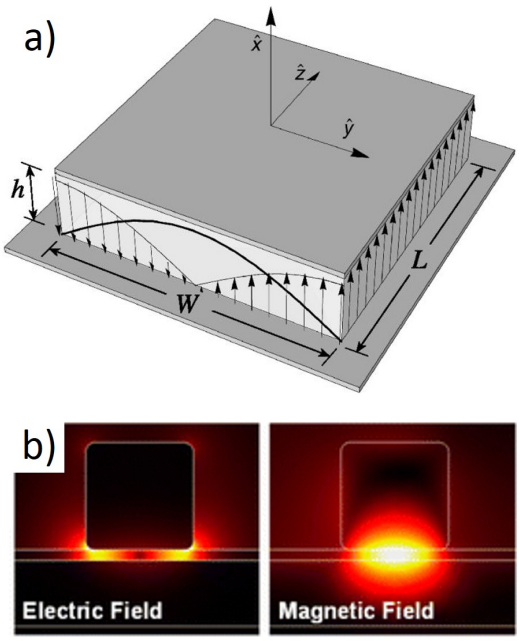

Figure 3.9: (a) Adapted from Ciraci et al.[159] - Diagram of a conventional patch antenna showing the coordinate system. The arrows indicate the strength and direction of the electric field and the thick, solid line indicates the magnitude of the magnetic field of the TM^{x}_{010} resonant mode. (b) Adapted from Lassiter et al.[83] - The simulated electric (left) and the magnetic (right) fields for the fundamental resonance of 81 nm Ag NC's above a Ag sheet with a 8 nm air spacer.

Through equating the tangential electric and magnetic fields at the metal boundary, it is possible to determine a dispersion relation for the mode:

$$k_x \tanh\left(\frac{k_x h}{2}\right) + \frac{\kappa}{\epsilon'_m(\omega)} = 0 \tag{3.14}$$

From which the propagation constant for the mode k_y can be obtained, and with it n_{eff}, the effective index of the mode, since $n_{eff} = k_y/k_0$. Due to the large electric field enhancements produced by the coupling between the patch and the metal film leading to a strongly increased density of states in the gap, n_{eff} can be significantly larger than the index of the spacer material for small h. For thin films where $h <\sim 30nm$ the approximation $\tanh(x) \sim x$ produces less than a 1 % variation and so an expression for k_y can be easily found:[160]

$$k_y \approx k_0\sqrt{\epsilon_d + 0.5(k_{ng}/k_0)^2 + \sqrt{(k_{ng}/k_0)^2\left[\epsilon_d - \epsilon_m + 0.25(k_{ng}/k_0)^2\right]}} \tag{3.15}$$

with:

$$k_{ng} = -\frac{2\epsilon_d}{t\epsilon_m} \tag{3.16}$$

The results from equation 3.15 are shown in Fig. 3.10. It can be observed that the effective index of the mode has a strong reciprocal dependence on h, which is to be expected for an evanescent process such as plasmonic coupling. It is also clear that for very thin films the resonance of the mode is highly sensitive to the spacer thickness. This was demonstrated experimentally by Lassiter et al, where alternating polyelectrolyte layers were deposited on to the Ag film via layer-by-layer deposition, allowing for sub-nm control over the spacer thickness, varying the resonance wavelength across a range of $\sim$ 200 nm.[83] A similar result was obtained in this investigation via the spin-coating of Nafion and is discussed in Chapter 7.

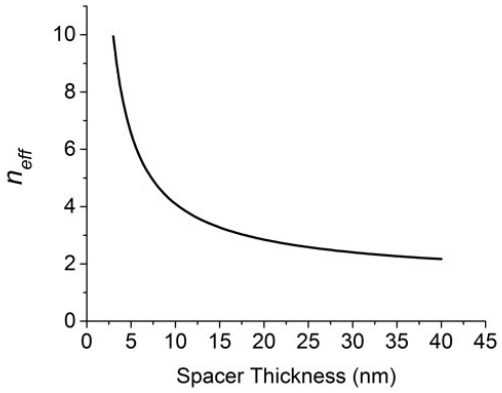

Figure 3.10: Plot of simulated effective index from solution of equation 3.15 for a 75 nm Ag cube separated from an Ag sheet by a Nafion spacer (RI = 1.35) with an illumination wavelength of 600 nm.

There are a couple of further points that are worth mentioning for completeness: The effects of the fringing fields have not been taken into account. In reality there is a significant component of the electric field that extends outside of the gap, as can be seen in 3.9(b), and so for a more accurate result a correction must be made for the *effective* width of the patch, so the resonance becomes:

$$\lambda_{res} = 2n_{eff}W_{eff} = 2n_{eff}(W + 2\Delta) \tag{3.17}$$

The sharpness of the corners is also important, as shown in section 7.5; this could be roughly accounted for using the current method with the correction factor in equation 3.17, although the value of Δ would have to be determined empirically. A more complete analysis of the NC system was conducted by Bowen et al,[161] who produced an eigenmode description of the NC system, which accounts for the effect of corners and fully describes the geometries of bright and dark plasmon modes. However, as the intention here is to provide insight into the formation and behaviour of the antenna modes in order to understand the experimental results in chapter 7, the model described is sufficient.

So far the patch has been considered as a generic flat sided particle of infinite height, and the cubic geometry of NP's in this investigation has not been accounted for. The last section showed how the modes of a NC hybridise near a substrate and the mode arising from the dipole becomes strongly concentrated about the substrate face, and interacts only very weakly with the upper surface and so will not be very sensitive to particle height. This has been investigated by Henson et al,[162] and the height of the particle has been found to have a significant effect on the modes excited in flat NP's above a substrate, but this is only pronounced for thin particles - when the height is close to the particle width the effect is seen to diminish, justifying the use of this model as an intuitive description of the fundamental mechanisms at play.

Another feature of this system that has not been discussed in detail here is the strong electric field enhancement produced by the gap modes within and around the spacer. This has been used to produce a metamaterial with a tightly controlled reflectance spectra,[82] enhance the fluorescence of dye molecules within the gap by over four orders of magnitude[85] and to produce spontaneous emission rate enhancements exceeding a factor of 1000 for these dyes.[84]

The strong dependence of the effective index, and hence the resonance wavelength on spacer layer thickness (as shown in Fig. 3.10) illustrates the potential of this system as a sensing element. Choosing a spacer material that expanded or contracted in response to some outside stimulus, an observation of the shift in the peak scattering wavelength

would provide a means to detect the environmental change. This idea is explored in chapter 7 where the NC patch antenna setup is utilised to create a novel gas sensing element.

3.5 Conclusions

This chapter has presented the theoretical background for the various stages of this investigation in order to provide sufficient grounding to understand the work that follows.

A model describing how the interference of light from a dipolar emitter in a thin film structure affects its farfield angular scattering pattern was presented. Previous work using this system as a dielectric antenna to increase light collection from single emitters was discussed and the idea of using this behaviour to optimise plasmonic light trapping suggested. This understanding of thin film interference will be brought together with the Mie model in the last chapter and used in chapter 5 to help build a holistic description of the effect a thin film structure has on the plasmonic behaviour of metal nanoparticles.

The modelling of plasmonic particles using the discreet dipole approximation was utilised to describe the modes and scattering properties of a noble metal nanowire. The phase mismatch between emitters at separate locations along the wire was shown to lead to interference which drastically altered the far-field angular scattering pattern and the combination of this effect with thin-film interference was suggested to produce highly directional scatterers, which is investigated in section 6.

The interaction of modes in an NP with its image in a substrate was found to lead to mode hybridisation, especially in flatter particles, producing new mode geometries and resonances. The case of a Ag NC separated from a silver sheet by a thin spacer was found to strongly resemble the behaviour of a patch antenna, and modelling the system as such whilst accounting for the finite absorption in the metal allows for the modelling of the fundamental mode, its effective index and thus the relationship between resonance

and spacer thickness. The utilisation of this relation to produce a novel sensor is reported in chapter 7.

The next chapter discusses the experimental techniques utilised in this investigation, before moving on to the experimental findings in chapter 5.

Chapter 4

Materials and Methodology

The purpose of this chapter is to detail the materials, methods and apparatus used in this investigation to provide the reader with sufficient information to recreate the results herein. The chapter begins with a discussion of the basics of FDTD modelling, and the simulation structures used to collect data. Secondly the materials used for every practical experiment in the investigation will be outlined, along with sample preparation techniques. Lastly the optical microscopes designed and utilised for this investigation, along with some key optimisation procedures will be described.

4.1 Finite-difference time-domain modelling

Finite-difference time-domain modelling is the principal method used to simulate the interactions of silver nanoparticles with thin-films in this investigation. The basic function of an FDTD operation is to simulate the propagation of an electromagnetic field through a defined region. It is a grid-based differential numerical modelling method, (hence 'finite difference') which operates in the time domain, allowing measurements from many different frequencies simultaneously without requiring an unreasonable amount of processing power. The Lumerical finite-difference time-domain software package[163] was used to perform FDTD calculations throughout this investigation.

4.1.1 FDTD background

An FDTD program works by solving Maxwell's curl equations (equation 2.1(b) & (d), also known as Ampére and Faraday's Laws) for an EM wave progressing through time and space. In a cartesian system, these expressions form a set of six scalar partial differential equations, which can be approximated as a set of *finite difference* equations as shown in equation 4.1.

$$\frac{\partial \mathbf{A}}{\partial x} \Rightarrow \frac{\mathbf{A}(x + \Delta x) - \mathbf{A}(x)}{\Delta x} \tag{4.1}$$

Where $\mathbf{A}$ represents an arbitrary vector along the x-axis. Taking differentials for each geometric axis into account, this approximation produces a 3D mesh over the volume considered, with the volume of each mesh cell determined by the step size Δx chosen in each dimension. Structures are defined by choosing the refractive index within each mesh element, and so the simulation will only describe structures with a resolution set by the chosen mesh size.

Each of these volumes is referred to as a 'Yee Cell', after one of the founders of the modern FDTD method.[164] In a Yee cell, the cartesian components of the electric and magnetic fields are calculated at different points within the cell, the electric E-fields along the vertices and the magnetic field strength, H-fields at the centre of the faces. This orientation allows for the solution of the finite-difference equations in a leapfrog manner, the electric components for each Yee cell are solved at one instance in time, then half a time step, $(\Delta t/2)$ later the H-field, and so on. This works as the H-field at a step in time can be approximated to depend only on its previous value and the curl of the E-field, and vice

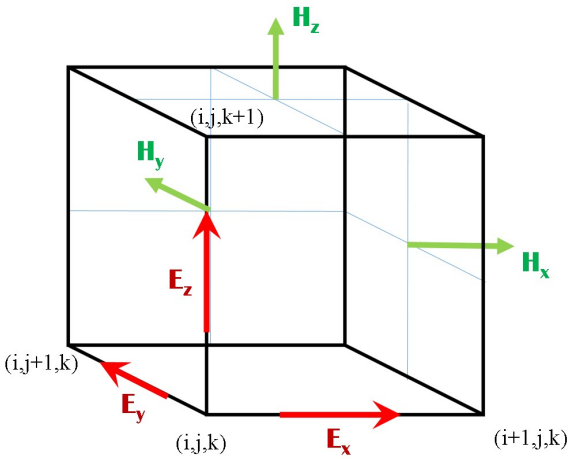

Figure 4.1: Diagram of a Yee Cell, the basic unit of a Finite-Difference mesh.

versa, as long as the steps in time and space are sufficiently small. This is an elegant solution as it removes the need for solving multi-dimensional simultaneous equations at each interval, which is what is required if one attempts to solve for electric and magnetic components simultaneously, and so dramatically reduces the processing time required.

Time-stepping algorithms are known to be prone to producing unphysical results if certain stability criterion are not met, often leading to exponential increases in the field values.[165] One of the most significant of these is the Courant-Friedrichs-Levy stability criterion,[166] (Eq. 4.2), which states that the field cannot travel more than the distance equivalent to the size of one mesh cell in a time step Δt. This is because the FDTD method can only propagate the wave from one cell to its nearest neighbors in each step, and so if an overly long time step is chosen which equates to a field passing through multiple cells, this will lead to instabilities, as described in several FDTD textbooks.[165, 167] Therefore the time step limit is defined by the smallest mesh size and the maximum speed of light in the simulation region, c_{max}, which is dictated by the refractive indices chosen.

$$\Delta t \leq \left(c_{max} \sqrt{\frac{1}{\Delta x^2} + \frac{1}{\Delta y^2} + \frac{1}{\Delta z^2}} \right)^{-1} \tag{4.2}$$

Cells must also be considerably smaller than the wavelength, $\sim \lambda/20$ is generally considered a maximum size, meaning that timescales must be of the order of a few femtoseconds.

Simulations are set to run until a stable condition has been reached, which generally means the EM wave has left the simulation region or been absorbed in the structures within. Once all data is collected in the time domain, a Fourier transform is required to obtain the results as a function of frequency. It is therefore doubly important that the simulation reaches a stable end state as small discrepancies in the time domain can produce significant deviations from an accurate physical representation of the system as a function of frequency.

4.1.2 Simulation geometry

To ensure stability of the simulation a good choice of simulation size is required along with appropriate boundary conditions at the simulation edge. The two most common general boundary types are a periodic boundary, which allows for the calculation of periodic arrays using only a single unit by copying the EM fields that occur at one side of the simulation and injecting them at the other side. Perfectly matched layer (PML) boundaries are multi-layer edges/surfaces (depending on the number of dimensions) impedance matched to the defined simulation, allowing them to absorb radiation with minimal reflection. An ideal PML will have zero reflection, but in practice there is always a small discrepancy due to the finite discretization of the PML equations. To minimise instabilities from these reflections it is important to structure the simulation so that stray reflections are not a significant source of error; generally very small simulation regions containing strongly scattering particles can lead to unphysical results.

A general overview of the simulation geometries used throughout the investigation will now be presented. Certain structural adaptions specific to individual setups will be outlined in more detail in the experimental chapters, but as most simulations follow a theme, the broad structure can be discussed here.

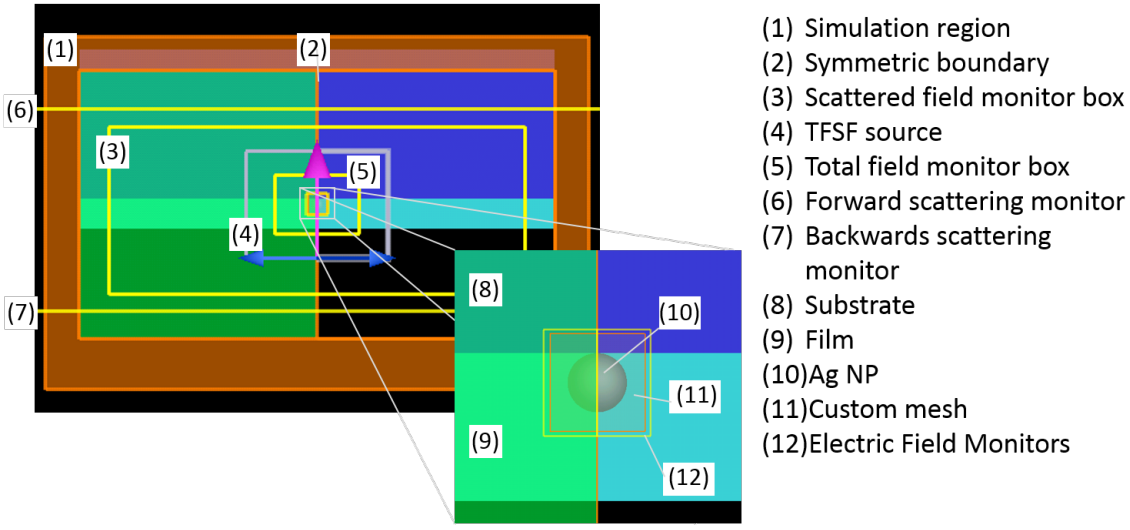

Figure 4.2: The general FDTD simulation setup on Lumerical

The cross section of a typical setup is shown in Fig. 4.2, a plane wave approaches a flat substrate coated in a thin film containing a nanoparticle with its centre at the

origin. The boundaries are all PML but with symmetry conditions which reduce the simulation time. In general simulations are conducted in three dimensions, but there are some situations (especially in chapter 7) where a 2D geometry will produce the same results, which drastically reduces the processing time. The simulation region is 8x8 μm across and 2μm in the direction of incident radiation. These dimensions were chosen to efficiently collect large-angle scattering from the particles and not lead to instabilities at the PML boundary as discussed earlier, whilst conserving on processing time.

A total-field scattered-field, (TFSF) source is used, which separates the scattered field from the incident radiation. The source region ((4) in Fig. 4.2) is defined as a box, with a plane wave incident from one face. The field inside the source box is the sum of the incident and scattered fields. At the boundary the incident field is subtracted so only the field scattered from the structures is present outside the source region. The scattered power then is taken from the transmission through each panel of the scattered field monitor box, ((3) in Fig. 4.2) which is placed outside the source region. Inside the TFSF region, the total field monitor box ((5) in Fig. 4.2) is used to determine the absorption from the balance of power flowing through each monitor.[168]

Cross sections (σ) are defined as the ratio of the power scattered by the particle, $\mathbf{P}_{scat}$ to the incident intensity from the source, I (units W/m^2) at a given wavelength:

$$\sigma(\lambda) = \frac{\mathbf{P}_{scat}(\lambda)}{I(\lambda)} \tag{4.3}$$

These values are determined from the simulations by measuring the net transmission of energy (defined as net power passing through a monitor face, as a fraction of the source power) across each face of a monitor box, from which the total scattered power, and hence the scattering cross section can be found:

$$\sigma(\lambda) = \frac{T(\lambda)\ \mathbf{P}_{source}(\lambda)}{I(\lambda)} \tag{4.4}$$

Where $\mathbf{P}_{source}$ is the source power, and T(f) is the total transmission function through all of the monitors that make up the monitor box. With an identical treatment available for absorption.

It can be seen that the cross section is in units of m^2, and therefore only gives information about the scattering efficiency of the particle, not the actual power scattered. It is conventional to normalise this value to the geometrical cross section, and cross sections are therefore generally given as a unitless parameter (written here as Q_{scat} and Q_{abs}), which indicates the strength of absorption/scattering from a given particle as a function of wavelength.

The fraction of light scattered forward or backwards can be calculated via the power transmission through a pair of monitors at either end of the simulation space. The fraction scattered forwards, into the substrate F_{subs} can be calculated by simply dividing the power transmitted through the forward transmission monitor ((6) in Fig. 4.2) by the total scattered power.

By examining the field components at the surface of each face of the monitor box and then summing the results, Lumerical is able to exactly determine the angular fields in the far-field using the surface equivalence theorem.[169] The far field projection propagates the scattered radiation to a hemisphere at a distance of 1 m from the origin, and therefore describes the scattered power as a function of angle (θ, ϕ), as shown in Fig 4.3.

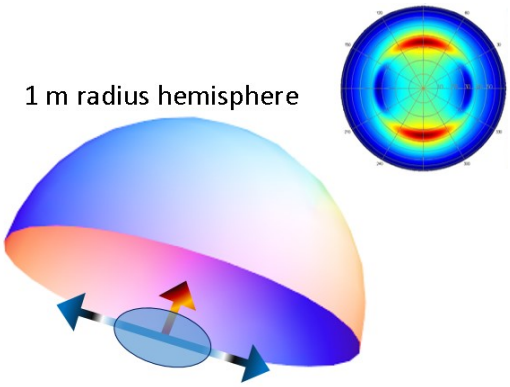

Figure 4.3: Showing the projection of the field components to the far field on the surface of a 1m hemisphere. Inset: an example of such a far field projection for a dipolar scatterer at a planar air-glass interface.

Planar field profile monitors bisect the particles, allowing the determination of the electric near field simply by analysis of the field intensity at each mesh cell on the plane of the monitor, as in Fig. 4.2. To conserve simulation time, a broader mesh is used in the general simulation area and a smaller (1 nm) custom mesh put into place around

the NP, where the detail is required.

4.1.3 Other numerical simulations

Other numerical modelling techniques have been used in the course of this investigation (the matrix transfer method in section 5.3.3 for example) although these are generally used only once and so will be discussed as they appear in the main body.

4.2 Nanoparticle preparation and characterisation

4.2.1 Spheres

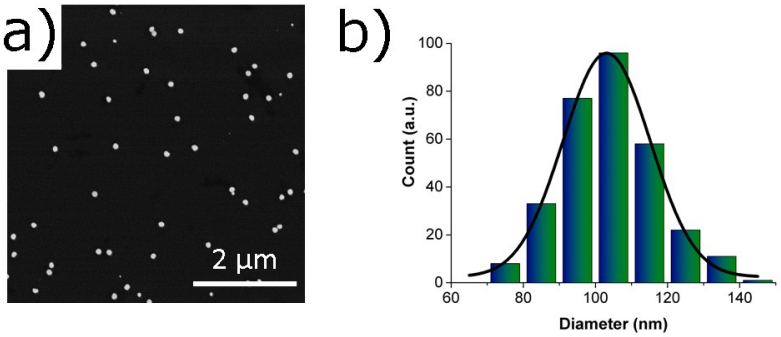

Figure 4.4: (a) SEM image of the nanospheres used in experiments in this investigation. (b) Histogram with fitted normal curve showing size distributions for a sample of 300 particles.

Samples were prepared using spherical silver nanoparticles, procured from Sigma Aldrich in an aqueous solution with poly(vinyl pyrrolidone) (PVP) as a dispersant[170] and diluted with deionised water. These were dispersed onto Si wafers as described in section 4.4, and imaged by the author in a JEOL 840F scanning electron microscope (SEM). Figure 4.4(a) shows an SEM image of the nanospheres used. The diameter of the nanoparticles was measured from SEM images using the ImageJ software.[171] The results from 300 particles is shown as a histogram with a fitted normal curve in Fig. 4.4(b). The NP's were found to have an average diameter of 110 ± 10 nm where the uncertainty represents the standard deviation, as will be the case with all uncertainties for the particle size measurements that follow.

4.2.2 Wires

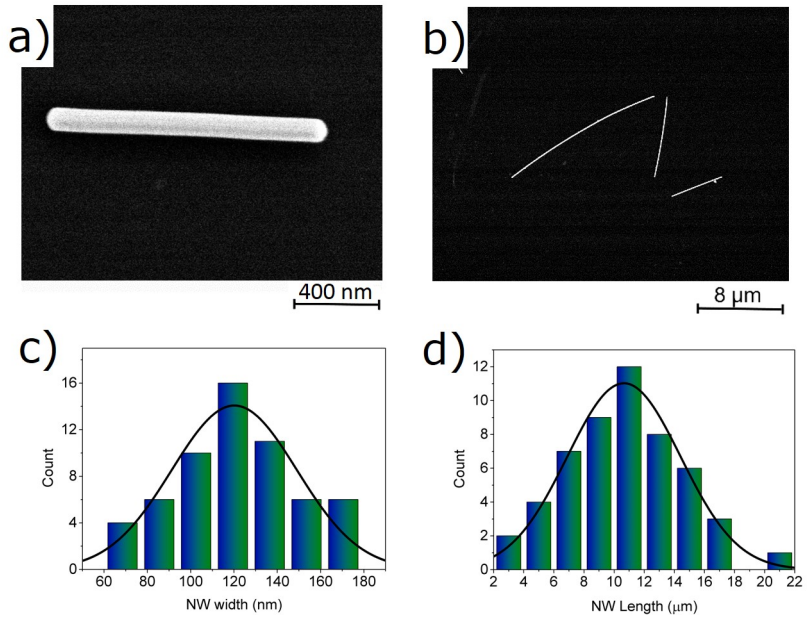

Figure 4.5: (a),(b) Close-up and wide view of some NW's used in this investigation taken with the SEM. (b),(c) Histograms with fitted normal curves showing width and length distributions for a sample of 50 wires.

Ag nanowires were produced in house by Natasha Hjerrild using a polyol reduction procedure[172] and were then centrifuged and dispersed in a methanol solution to minimise corrosion. SEM images of some typical NW's are shown in Fig 4.5(a)&(b), and a sample of 50 NW's showed an average diameter of 120 ± 20 nm. The wires have an average length of 11 ± 4 μm, and the large standard deviation of this sample is a reflection of the difficulty of producing monodisperse samples in-house.

4.2.3 Cubes

Silver Nanocubes were purchased from Nanocomposix[148] and characterised using a Jeol 3000F TEM as shown in Fig 4.6. A sample of 70 NC's were found to have an average width of 76 ± 5 nm, with a corner radius of curvature (RoC) of 10 ± 3 nm, and a PVP buffer layer thickness of ∼3 nm. These were diluted in deionized water at a ratio of 1:50 and sonicated before use.

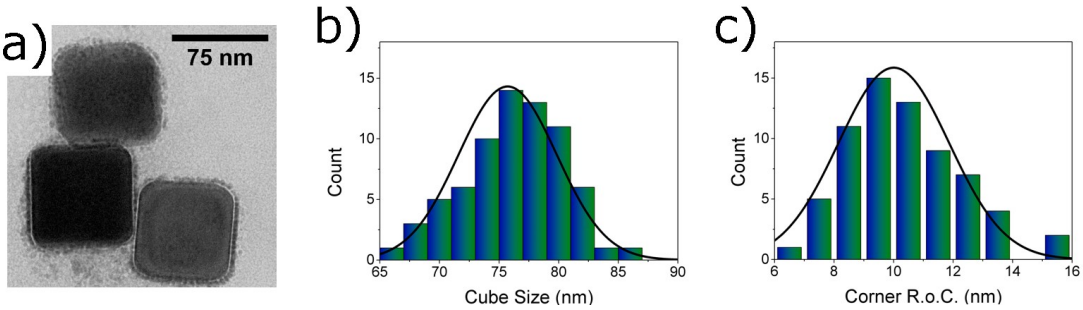

Figure 4.6: (a) TEM image of the cubes used in this investigation. (b),(c) Histograms with fitted normal curves showing size and corner RoC distributions for a sample of 50 cubes.

4.3 Polymers and solvents

4.3.1 PTFE AF

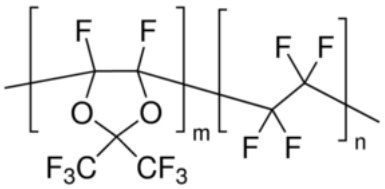

Figure 4.7: The chemical formula for PTFE AF.

Thin films were produced using the low index polymer Poly[4,5-difluoro-2, 2-bis(trifluoromethyl)-1, 3-dioxole-co-tetrafluoroethylene] (PTFE AF 1600) , bought as a powder from Dupont.[173] PTFE AF was chosen because of its exceptionally low refractive index (the lowest of any commercially available polymer at ∼1.31) which arises due to the large free volume in the matrix when spin-coated,[174] due to the formation of nanovoids of diameter < 0.5 nm. Simulations conducted using voids of this size in a higher index matrix have shown that this does not affect the scattering behaviour of ∼100 nm NP's and it is valid to consider the polymer a uniform matrix.[175] PTFE AF is extremely stable and insoluble in most standard solvents and so was dissolved in the Fluorinert^{TM} liquid FC-40 from 3M.[176]

4.3.2 PVA

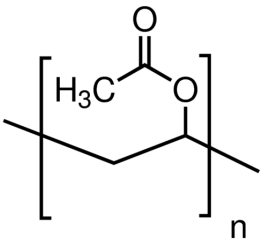

Figure 4.8: The chemical formula for PVA.

Polyvinyl acetate (PVA) was purchased as a powder from Sigma Aldrich[177] and was mixed with deionised water to form solutions for spin-coating. It was selected for its transparency and its refractive index of 1.465. Its chemical formula is shown in Fig. 4.8.

4.3.3 Nafion

For humidity sensing in chapter 7, the Nafion^{TM} fluoropolymer from Dupont was used to alter the plasmonic modes and/or scattering patterns of metal nanoparticles. Nafion is a Poly(perfluorosulfonic acid)-based ion-conducting membrane with a hydrophobic fluorocarbon polymer backbone and hydrophilic sulfonic acid side chains. These two principal components are highlighted in Fig. 4.9.

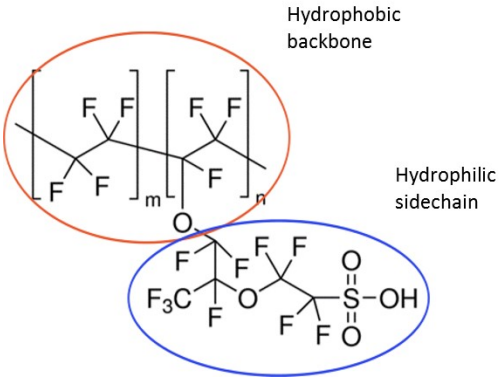

Figure 4.9: The chemical formula for Nafion

The backbone and sidechains phase-segregate in a planar film, forming hydrophilic domains which take in moisture from the surroundings and expand significantly in the presence of water either in solution or as a vapour and more rigid backbones that align parallel to the substrate, providing a rigid structure which limits the expansion.[178–180] Nafion membranes have been found to expand around 15-20% for a humidity shift of 0-100%, although this does depend somewhat on the processing of the film.[181, 182] The behaviour of very thin (< 50 nm) Nafion films is

somewhat more involved and will be discussed in more detail in section 7.2. The Nafion used in this investigation was purchased as a resin from Sigma Aldrich[183] and was mixed with laboratory grade ethanol to form solutions for spin-coating.

4.4 Sample Preparation and calibration

Substrates used were either 1 mm thick monocrystalline silicon wafers or glass, 16 mm, No. 1 coverslips measured to have a thickness of 0.14 +/- 0.02 mm and an RI of 1.526. Silicon substrates were cut using a diamond scribe into 15 x 15 mm squares. Samples were then sonicated in deionised (DI) water, acetone then isopropanol for 10 minutes each, and dried in a vacuum oven at 60 C for one hour.

As this investigation is mostly concerned only with individual nanoparticles, samples were required where particles were sufficiently well dispersed that they could be selected individually by an aperture, but dense enough that they could be located on a sample without undue difficulty. Contrary to expectations, achieving this proved to be a non-trivial exercise, and so for the benefit of those following this work, the methods attempted will be briefly described.

The nanoparticle solutions were diluted in DI water, sonicated to remove aggregations and then deposited through an 0.4 μm Polyvinyl Difluoride (PVDF) filter. Initially solutions were simply drop-cast onto substrates, but it was found that even with low concentrations, particles tended to aggregate around the edge of the drying droplet due to the water surface tension forming a 'coffee stain' pattern as shown in Fig. 4.10(a). Repeating this procedure in an environment of evaporated ethanol reduced this by relieving the surface tension of the water but still produced clumped nanoparticles even after sonication for $>$ 30 mins. Spin coating the samples removed the coffee stain effect, but still left aggregations of 3-5 particles (Fig. 4.10(b)).

A third approach was first used by Moreau et *al.*[82] A glass slide is cleaned and a 30 μL drop of NP solution deposited upon this. Then the substrate is gently placed above the droplet, which will compress and expand to cover the entire surface. In this

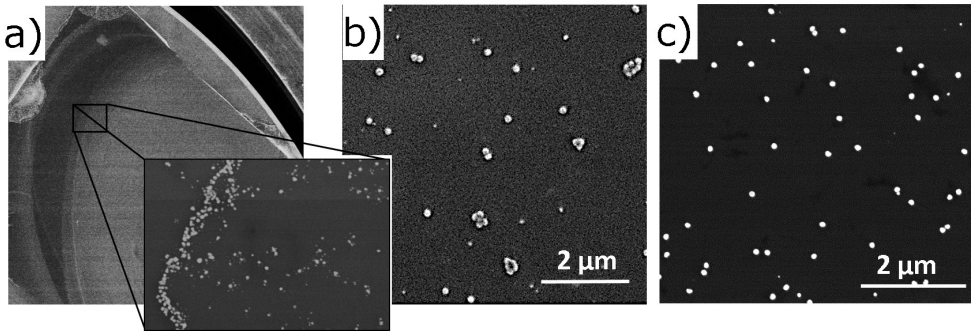

Figure 4.10: (a) Drop cast NP's, highlighting the coffee-stain effect. (b) NP's spin-cast from solution. (c) NP's deposited using Moreau's method.

setup, individual particles adsorb onto the substrate, but aggregates and other large particles stay lower in the solution and so do not, producing the well dispersed particles seen in Fig. 4.10(c). Some control over the surface density can be achieved by varying the solution concentration and the time exposed to solution, although this was not investigated here. The chosen conditions for NP's from Sigma Aldrich was a dilution of 1:100 by volume, and a solution exposure time of 4 minutes. For the nanocubes from Nanocomposix, a dilution of 1:200 by volume and an exposure time of 2 minutes was chosen. Once finished the samples are rinsed in DI water to remove residual solution which could evaporate to form clumps.

Nanowires are much heavier than cubes or spheres and so this method was found to be unsuitable for their use. Filtration is also not possible due to their size. The difficulties are reduced with wires however as they are much brighter scatterers than NP's and most impurities in the samples, and very easy to find under a microscope. As NW's have a much stronger tendency than smaller NP's to settle at the bottom of a container, they require an ultrasound sonication time of 20 minutes before use. Spin coating a 1:20 dilution of the NW solution at 3000 rpm for 90 s provided a good dispersion.

After applying the particles to a substrate, there is still often a coating of PVP around them, which can be quite thick (Fig. 4.11(a)) and have a significant effect on results (see Fig. 4.19). The samples were therefore etched in an Oxygen plasma after deposition to remove the PVP and other organic residue. This was achieved by exposing samples to a plasma for 30 s in a SPI Plasma Prep III Plasma Etcher. Ag nanowires oxidise incredibly quickly under an oxygen plasma, rendering them unusable (Fig. 4.11(c)),

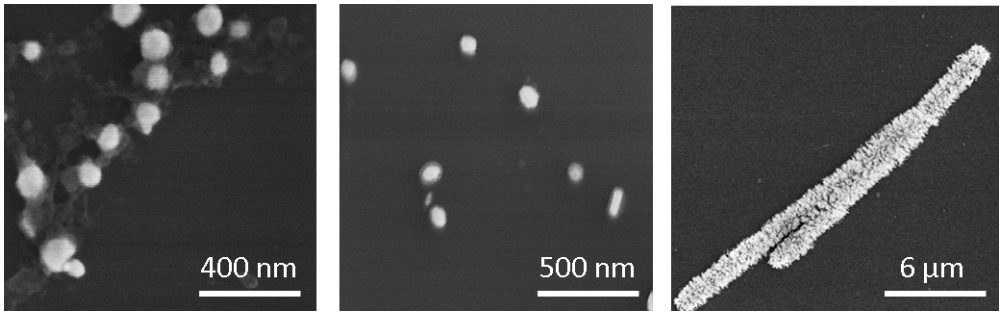

Figure 4.11: 100 nm Ag NP's (a) unetched, showing a particularly bad region of PVP coating and (b) etched in oxygen plasma, displaying no organic residue. The effects of etching in oxygen plasma on (originally) 115 nm diameter Ag nanowires is shown in (c).

but were not observed to have a significant PVP coating as shown in Fig. 4.5 and so further treatment was not required. The nanowires were observed to oxidise with time however, and regular inspection was required to ensure that oxide layers and nodules which formed at grain boundaries[184] were not compromising the sample.

4.4.1 Thin film deposition

All polymer films were deposited using spin-coating. Substrates were spun at varying spin speeds for 90 seconds and 50 μL of polymer solution was dropped while spinning through a 0.4 μm pore PVDF filter, with the exception of PTFE AF, which required a PTFE filter of equivalent pore-size.

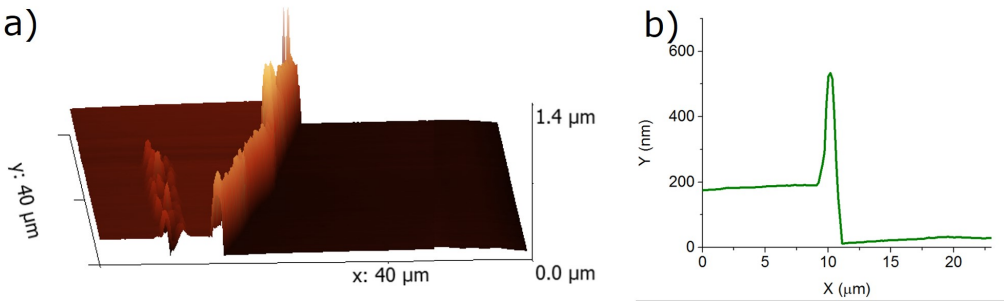

Figure 4.12: AFM image (a) and trace (b) of the edge of a PTFE AF layer as used to measure thickness.

Film thicknesses were measured using a Veeco DekTak 6M profilometer. At least 25 readings taken across 3 samples were used to obtain each datapoint. First, a scalpel was used to scrape away some of the film and then the step crated used to measure the thickness. This technique was found to efficiently remove all of the film from the

substrate without damaging the glass or silicon beneath as confirmed using a Pacific Nanotechnology Nano-R atomic force microscope (AFM) in tapping mode. As the AFM images in figure 4.12 show, the scraping process can create a distinct 'pile-up' of polymer at the edge of the step, but on either side the material is flat and reliable measurements can be taken. Surface features and roughness were also investigated using the AFM.

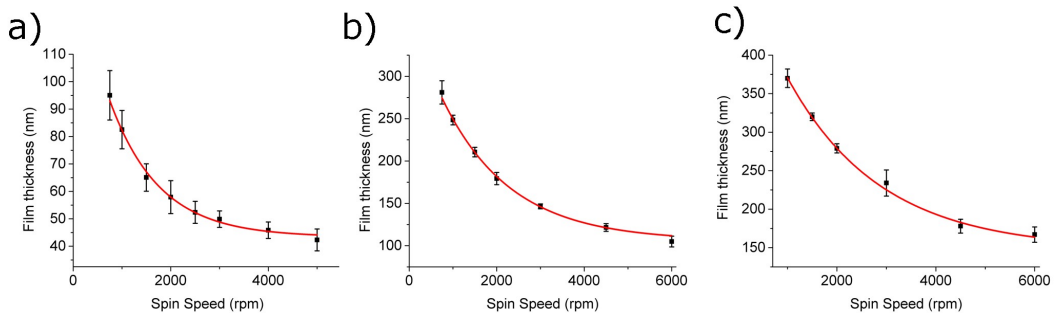

Figure 4.13: Spin coating calibration curves for (a) 1 %wt., (b) 2 % wt. & (c) 3 %wt. PTFE AF in FC40 solution. A fit line has been added to each curve for clarity.

Figure 4.13 shows the spin coating calibration curves for PTFE AF on a glass coverslip for 1,2 & 3 % solutions of PTFE AF in FC40 solution, all data points represent 60 DekTak readings across three samples and the error bars show the standard deviation. Using these three dilutions it was possible to produce films with any thickness between 50 and 350 nm. The root mean squared (rms) surface roughness of the films was found to be 2.2 ± 0.4 nm, which did not change within error for all thicknesses investigated.

As NP's are being coated with films with thicknesses of the same order of magnitude as their diameter, some conformation of the thinner films to the particle shape is to be expected, i.e. the film will not just lie flat above the particle but will follow its shape to some extent. Films of 54, 114, 203 & 307 nm were coated over NP's and examined in the AFM as shown in figure 4.14. A degree of particle conformation was observed, with the rise in the film surface created by the particle diminishing as film thickness increases. For a 114 nm film the bulge in the film is observed to be 20 ± 4 nm which reduces to 9 ± 2 nm for a 203 nm film and is mostly negligible for a 307 nm thick film. The thinnest films used in the following chapters were 89 nm thick, and so there can

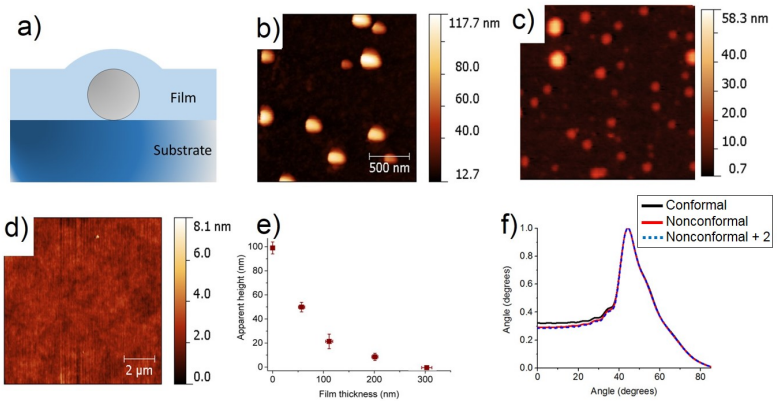

Figure 4.14: (a) Showing film conformation above an NP. AFM images of (b) bare NP's & NP's coated in (c) 114 nm and (d) 307 nm PTFE AF respectively. (e) Apparent particle height as a function of film thickness, showing the deformity of the film around the particle. (f) Simulations for a 114 nm film showing the negligible effect of film conformation on the scattering pattern.

be a significant deviation from the case of a flat film neatly covering the NP.

To investigate the effect of this, scattering at 532 nm from a 107 nm Ag NP beneath a 114 nm film with a spherical deformation which increased the height of the film by 20 nm and has a FWHM above the film of 140 nm (matching experimental observations) was simulated using Lumerical. The results are shown in Fig. 4.14(f). The effect on the scattering patterns is surprisingly small, and only observable at low angles. The change in the scattering pattern from a flat to a conformal film agrees within 2 % with that of a flat film of 116 nm, a thickness increase of only 2 nm. As this is below the thickness uncertainty of the films, and the deformation is reduced for thicker films, the effects of film conformation on scattering pattern are considered negligible in this investigation.

PVA was only used briefly to alter the refractive index surrounding a particle, as shown in Fig. 5.5, and no data was taken which depended strongly on film thickness. A 3 % wt. solution was spun at 3000 rpm giving a thickness of 284 ± 9 nm as measured by DekTak.

The Nafion films used for relative humidity experiments were produced to investigate two different length scales, the thicker films needed to coat NW's and alter their scattering patterns in section 6.4 need to be of the order of ∼100 nm, whereas the films to

act as a spacer for NC's in chapter 7 are required to be as thin as possible. Calibration curves for these films are shown in Fig. 4.15. Surface roughness under ambient conditions was found using an AFM to be 1.7 ± 0.5 nm and was not found to change within the bounds of error for differing film thicknesses.

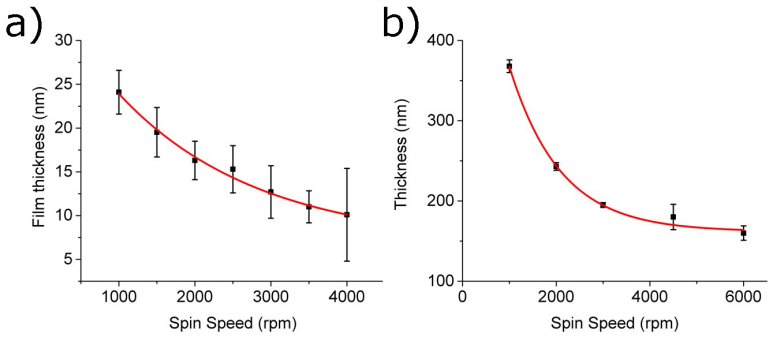

Figure 4.15: Spin coating calibration curves for (a) 0.25 %wt. & (b) 3 % wt. Nafion in ethanol. A fit line has been added to each curve for clarity.

Thicker films were spun onto glass using 3 % wt. nafion in ethanol. Thin films used a solution of 0.25 % wt. Nafion, and were spun onto either bare or Ag coated Si wafers, where a 100 nm layer of silver was coated onto the silicon in a home-built evaporation chamber. Samples were heated to 70 degrees under vacuum for 2 hours to promote adhesion of the Nafion to the substrate. Very thin films spun at or above 4000 rpm did not generally achieve complete surface coverage and there was a very high fail rate for these samples. Therefore the fastest spin speed used was 3500 rpm, which gave a film thickness of 10.9 ± 1.6 nm. The properties of these films are discussed in section 7.2.

4.5 Optical microscopes

This investigation focusses on the scattering from individual nanoparticles in various thin-film environments, and is concerned with acquiring information about the spectral and angular scattering behaviour of these particles. There have been two designs of microscope used to take data; the first is a dark-field microscope which allows the observation of light scattered by particles in the image and the Fourier planes simultaneously, enabling the selection of individual nanoparticles. This will be referred to as the 'Fourier scope' and is shown in Fig. 4.17. The second dark field microscope (Fig. 4.20) investigates the spectral scattering of particles and allows for environmental control around the samples, and well be referred to as the 'spectral microscope'.

4.5.1 Fourier-space measurement

The principles behind measuring the angular scattering pattern of a particle are illustrated in Fig. 4.16.

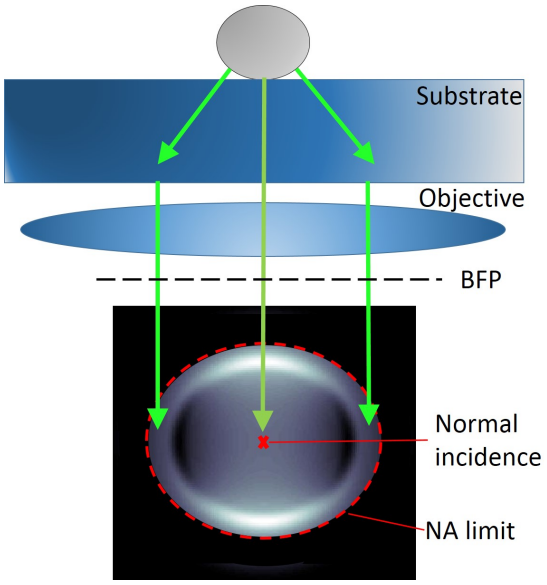

Figure 4.16: Illustrating the Fourier space imaging of scattering from a spherical NP above a dielectric substrate.

Light scattered or emitted from a particle (in this case above a substrate) towards an objective lens is collected up to an angle defined by its numerical aperture (NA), where $NA = n\sin(\theta_{max})$. At the back focal plane (BFP) of the objective, the angle of scattered light arriving at the lens is translated into a spatial location (also shown in Fig. 4.17(b)). Light scattered along the optical axis (normal to the substrate if all is aligned correctly) is at the centre of the plane, and light scattered at large angles is further towards the edge following the relation $r \sim sin(\theta)$ where r is the distance from the centre of the BFP and θ is the angle from the optical

axis. The entire image will appear as a circle, with the edge of the circle defined by the NA of the objective. This can be imaged on a CCD at any Fourier plane of the system and the intensity at any given point is directly proportional to the scattering intensity at the corresponding angle.

4.5.2 A darkfield, Fourier-space microscope

Most conventional darkfield setups involve light approaching the sample at large angles and being collected close to the normal, or utilise total internal reflection to excite samples evanescently.[137] One of the major applications for plasmonic scattering in multilayered structures is light trapping in thin-film solar cells, via path length enhancement due to wide-angle scattering as discussed at the beginning of chapter 5. Solar cells are usually designed to face the source of illumination directly, and hence this microscope was designed and built by the author to investigate the wide-angle scattering of particles from light at a normal incidence to the substrates.

Figure 4.17 shows the setup: A 532 nm Shanghai Dream SDL-532-030F frequency doubled, diode pumped solid state laser was used to illuminate the sample. A wavelength of 532 nm was chosen to best coincide with the dipolar scattering peak from 107 nm Ag NP's (see Fig. 5.5). The beam leaving the laser was extremely messy and contained large intensity shifts across its width and leading to increased noise in the readings. To counter this, light from the laser was focused into a 50 μm pinhole aperture and the recollimated using an identical lens. A variable aperture was used to apodize the resultant beam, which produced a much improved profile. The light was then focussed on to the back focal plane of a Nikon 100x 1.4 NA objective lens using a 1 mm diameter, 45 degree rod mirror (RM) from Edmund Optics,[185] ensuring that it arrived at the sample as a collimated beam travelling perpendicular to the sample plane as shown in the inset of Fig. 4.17(a), illuminating a broad area of approximately 2 mm. Most light passes directly through the transparent samples, and specular reflection from the planar interfaces is blocked by the rod mirror, which also serves as a patch stop. Using the RM as the patch stop also removes the need for an additional Fourier plane and

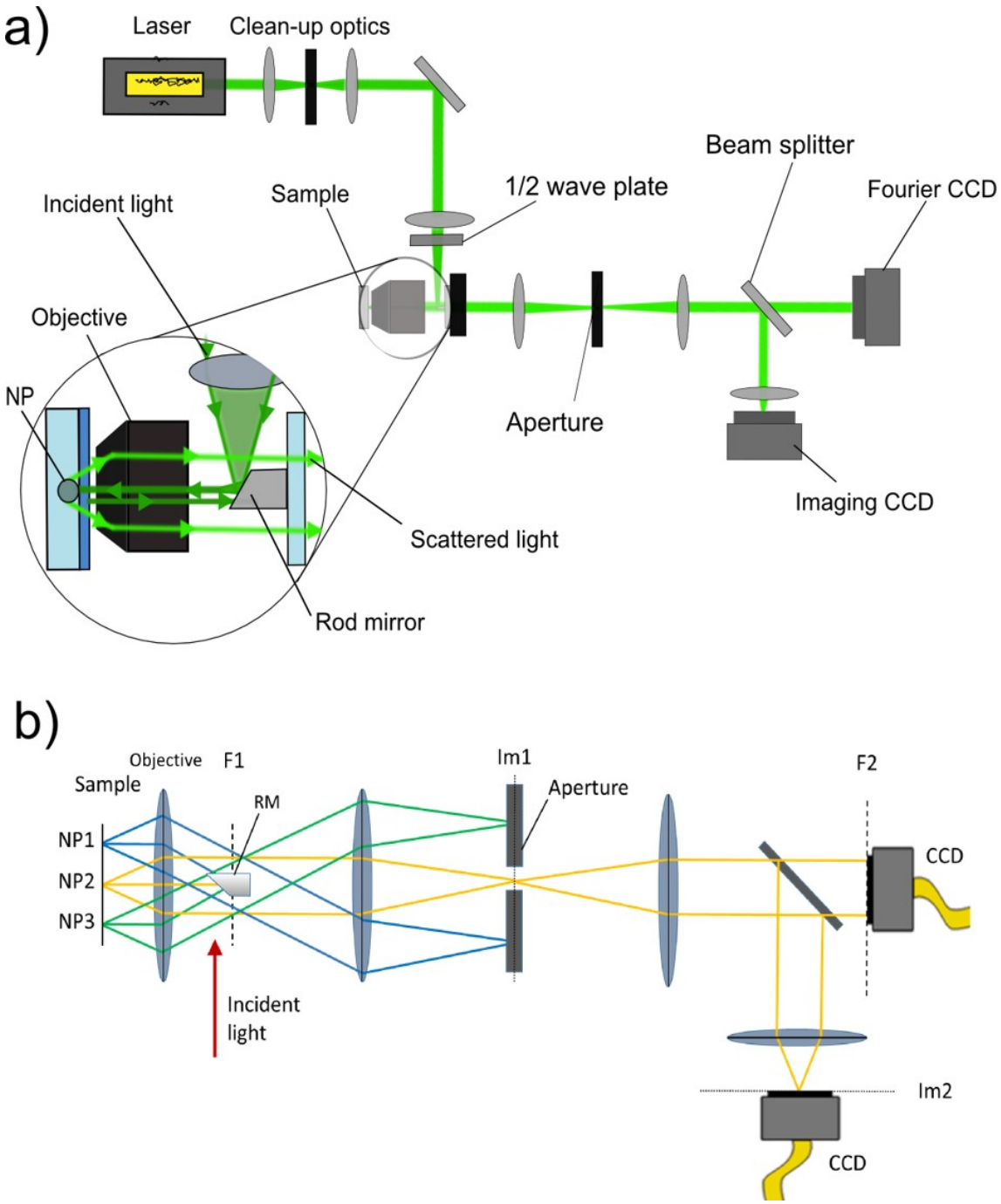

Figure 4.17: (a) Diagram of the home-built, darkfield, Fourier-space microscope used to measure the directional scattering of NP's in thin films for the first time. The utilisation of the rod mirror to illuminate the sample and block specular reflection is highlighted. (b) Ray tracing diagram of the key elements of the microscope, highlighting the exclusion of small angle light by the rod mirror in the BFP (F1) and the spatial selection of individual NP's in the image plane (Im1).

this arrangement results in a significantly smaller fraction of k-space being blocked off than designs in other recent investigations.[139, 186, 187] Scattering from defects in the film, the interfaces and the lenses prevented the use of a smaller patch stop.

Through measuring the extent of the Fourier space that can be observed with this setup, on the CCD, then calculating the size at the back focal plane of the objective from the size of the CCD pixels and the magnification of the lenses, it was determined that the objective actually has a working NA of 1.23 ± 0.01 and the patch stop an NA of 0.15 ± 0.02 where the uncertainty is the standard deviation from repeat readings. Figure 4.17(b) is a ray-tracing diagram of the scattered light which displays how the Fourier scope makes use of both the image and Fourier planes to block specular reflection at F1, select individual particles at Im2, and then image the scattering as a particle image and as a function of angle at Im2 and F2, using two point grey chameleon monochrome CCD's.

The only slight drawback to this setup is that light is incident from the substrate side rather than the front. The reasoning behind this was to minimise noise from background scattering, which was found to be substantial for front illumination and required the use of larger patch stops. Simulations show that scattering from dipolar modes is equivalent for front and rear illumination however, and so the use of this setup in Fourier space is justified.

The fact that this setup can measure scattering without needing to use any kind of fluorescence makes accurate detection of particles and visualisation of scattering patterns a far more convenient process than systems relying on the secondary excitation of some fluorescent dye, which would be the only other option to excite the sample with normal illumination. This has been achieved without use of Total Internal Reflection measurements also, which means that the angular range is only limited by the NA of the objective and the rod mirror diameter, not the critical angle for the substrate. The trade-off is that a portion of the image is blocked by the RM and so low-angle scattering cannot be imaged. Experimental results in the following chapters show that this setup is extremely well suited to measuring the scattering patterns of nanoparticles and the loss of low angle scattering does not reduce the utility of data taken from this microscope.

There are two further points which are worth noting here: Firstly, since the particles

are scattering coherent laser light, there was a significant problem with speckle in the images, as shown in Fig. 4.18(a). The classic solution to this problem is to spin a disk of ground glass or other diffuse material in front of the beam to reduce the coherence of the incident light and thus reduce the speckle in the scattered pattern.[188] Disks of several materials including a plastic slide and ground glass diffusers (220 and 600 grit) from Thorlabs were attached to a small motor and spun at varying speeds in the beam path. Whilst this removed the speckle, it also depolarised the light, fundamentally altering the observed pattern.

The second method that was attempted was to use a small motor strapped to the sample cageplates to vibrate the sample, which is a technique used to reduce speckle in optical fiber outputs[189] and produced similar results, but without altering the polarisation. Care had to be taken with this arrangement as the vibrations could be powerful enough to defocus the setup slightly after each measurement. The difference between the results in Fig. 4.18 is striking and it is clear that to obtain results sufficient to accurately compare with theory some form of decoherence must be utilised, for which the vibrational method has proven sufficient.

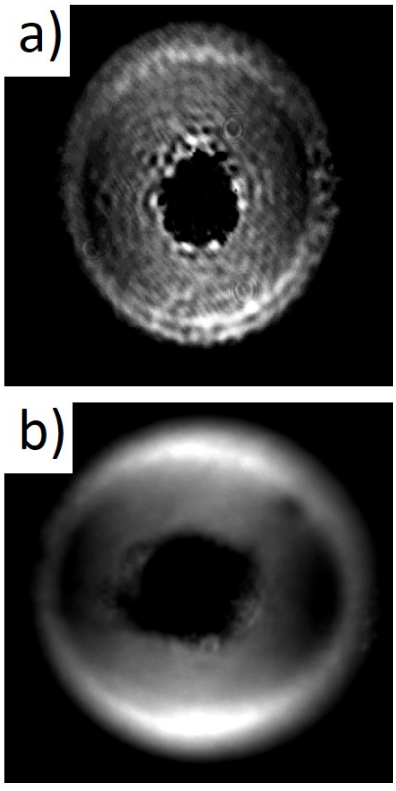

Figure 4.18: Average measured Fourier space scattering images for 50, 100 nm Ag NP on a bare glass substrate with (a) no speckle correction and (b) using the vibrational decoherence method.

Secondly it is worthwhile at this point to highlight the importance of the plasma etch described in section 4.4. In figure 4.11 SEM images showed that there was generally a PVP residue on the NP's which the oxygen plasmon etched removed. This residue was found to have a significant effect on the scattering pattern of particles as measured in Fourier space, as shown in Fig. 4.19.

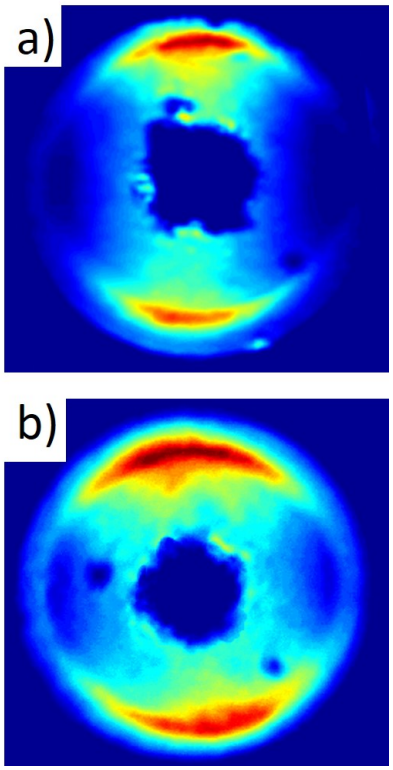

Figure 4.19: Average measured Fourier space scattering images for 50, 100 nm Ag NP's on a bare glass substrate (a) without etching and (b) after a plasma etch.

It can be seen that the observed patterns are quite different, with the scattering pattern for the unetched particles in 4.19(a) resembling that of NP's under a thin film as shown in Fig. 5.11. This reinforces the evidence from SEM that etching is a key experimental step to obtain accurate scattering data for small particles. NW's tended to be much cleaner than NP's and as the data obtained from them agreed well with simulations, the fact that they oxidised horribly under a plasma etch was not a problem.

The angular scattering into the substrate from single plasmonic particles at an interface has not been well studied experimentally, and the scattering patterns of NP's in films not at all, and this setup is a good experimental tool to observe scattering into a substrate across a wide angular range with minimal angular losses.

4.5.3 Dark-field scattering with environmental control

The home-built darkfield microscope created to take spectral scattering data from the nanocube patch antennas in chapter 7 is illustrated in Fig. 4.20. Light from either a white light source or a Toptica Photonics DL100 grating stabilised 632 nm diode laser (chosen to be close to the peak wavelength of the film coupled NC's as shown in Fig, 7.6) is focused onto a sample from an angle of 60 degrees to the normal, to ensure that no specular reflection is collected by a 20 mm working-distance 50x 0.55 NA Nikon objective lens. A beam splitter directs some light to a Thorlabs 120A2/M avalanche photodiode (APD) to check the stability of the laser, the variation of which was found to

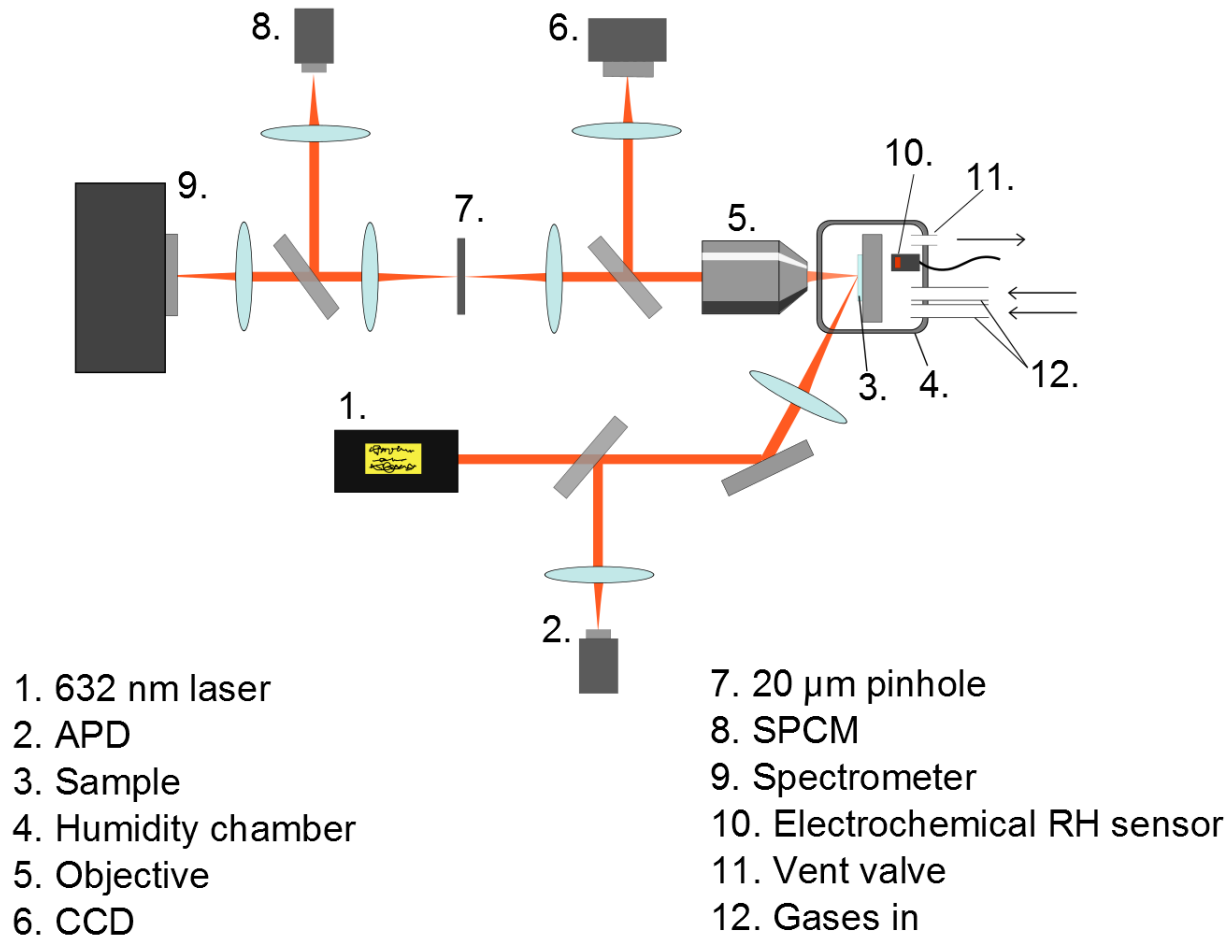

Figure 4.20: (a) Diagram showing the home-built darkfield microscope created to take spectral scattering data from the nanocube patch antennas in chapter 7.

be negligible compared to noise due to vibrations, dust and small atmospheric changes as observed in Fig. 7.12 and so normalisation to the laser intensity was not required. A second beam splitter directs light to a CCD to image the samples. Two telecentric lenses then focus light through a 50 μm pinhole aperture to allow for the selection of individual particles where required. A final beam splitter then splits light between an Excelitas SPCM-AQRH single photon counting module (SPCM) and an Andor SR-500i spectrograph to analyse the scattering from the NC's.

For many experiments, the samples were enclosed in a custom-built environmental control chamber. This consisted of an air-tight casing with NBK7 optical windows for incident and scattered radiation. Two gas inlets allowed for moist and dry air to be injected into the chamber and a small outlet valve maintained a constant pressure. A

TSP01 humidity and temperature sensor from Thorlabs[190] was used to monitor the conditions in the chamber as the gases were added.

4.6 Conclusions

This chapter has described the simulations and experimental methods utilised throughout this investigation along with an account of the major difficulties encountered and their solutions. The principles of Finite-Difference Time-Domain modelling were introduced, and the simulation geometry used in this study outlined. The nanoparticles, polymers and solvents used were reported and their procurement, depositon and characterisation detailed. Two custom designs of optical microscopes created to examine spatial and spectral scattering of light from nanoparticles were described in detail, and compared with other designs in the literature.

Following this chapter, the results of simulations and experiments investigating the effects of a thin-film environment on the scattering behaviour of individual silver nanoparticles are presented. The next chapter examines the simplest case of a spherical particle in a dielectric film, chapter 6 explores the effect of particle shape and chapter 7 presents a novel gas sensor design based on a nanocube separated from a silver sheet by a thin film.

Chapter 5

Plasmonic properties of Silver nanospheres in dielectric thin films

This chapter is based around the papers 'Controlling the optical scattering of plasmonic nanoparticles using a thin dielectric layer',[191] and 'Directional plasmonic scattering from metal nanoparticles in thin-film environments',[142] by Powell et al., but also contains additional material.

For a metal particle placed in a thin dielectric film, the interplay between the localised plasmons and the interference properties of the structure affords a rich parameter space for study. A slight alteration to one of the many variables of this system can lead to a significant change in the near and far field behaviour of the plasmon modes. Previous chapters have discussed the formation of plasmon modes in spherical particles, their response to a high-index substrate and the effect of thin film interference on dipolar emitters. In this chapter these ideas are combined and expanded upon to conduct a detailed investigation of the behaviour of spherical Ag NP's in dielectric thin films.

This is the first time an analysis of plasmon scattering in thin films has been carried out: previous work has mostly focused on particles at the interface of a substrate with free space, which will rarely be the case in completed devices. Even if the NPs are placed at the front of a device (e.g. a solar cell or LED), before the active region and any other conducting layers, thin-film electronics are typically coated in a sub-100 nm protective oxide,[192] which will then alter the optical properties. The effect of a multi-layered structure is often neglected, with previous works at best simply attributing enhancements to "scattering"[193] and at worst assuming identical behaviour to a dipole at a simple interface,[58–60] so an investigation into plasmon scatterers in a thin film structure makes a timely contribution to the literature.

There has also been much interest in plasmonic NP's as nanoantennae for quantum dot[61] and dipolar emitters.[194] Whilst various NP geometries have been tested, so far only structures formed on a bare surface have been considered and the ability of a thin-film environment to alter the behaviour of plasmon modes in metal nanoparticles has not been investigated. Studies into fluorescent dyes in thin films (as discussed in section 3.1) showed that the film structure was of significant importance for altering the emission patterns, and so a significant effect with plasmonic particles can also be expected.

The results that follow demonstrate that a careful tuning of the parameter space can enhance forward scattering and reduce Fano losses, which is important for light trapping and antireflection applications. The structure also enables some tuning of the scattering directionality and power, which is of interest for nanoantennas and single emitter detection. FDTD simulations and experimental techniques are used to explore the behaviour of a metal particle in a thin dielectric layer between two semi-infinite half spaces, where generally, $n_{air} < n_{film} < n_{subs}$, as shown in Fig. 5.1. This chapter focusses on the properties of spherical nanoparticles as the simplest and most readily fabricable system, before moving on to discuss other shapes in chapter 6.

To begin the chapter, the simulation space is described. Secondly, the general effect of overcoating a nanoparticle resting on a high index substrate with a low index film on

the excited modes and the strength and directivity of scattering is discussed. Following this, the parameter space of this system is explored: the refractive index of each layer is varied in turn as is the thickness of the film above and beneath the particle. The impact of these parameters on the absorption and spatial and spectral scattering are analysed in detail both at a fundamental level and with a view to how they might impact potential applications.

5.1 The simulation space

The structure used throughout the simulations is displayed in Fig. 5.1. A spherical silver nanoparticle (NP) was placed within a thin dielectric film in between two dielectric half-spaces, here labelled as 'air' and 'substrate', or 'subs'. For most simulations the RI of layers was set initially as n_{air}=1, n_{film}=1.5, n_{subs}=1.8, corresponding to air, Polyvinyl acetate (PVA), and sapphire layers. These values were chosen as a readily fabricable system which provides a large RI contrast in order to better highlight the properties of the system. Due to the difficulty in index matching for sapphire however, glass substrates were later used for the experimental Fourier-space measurements, and matching simulations have been produced for comparison where relevant.

Another reason for the interest in these layers is that they also bear much similarity to a P3HT:PCBM, PEDOT: PSS structure, (poly-3-hexyl thiophene : phenyl-C61-butyric acid methyl ester, poly(3,4-ethylenedioxythiophene): polystyrene sulfonate) seen in many organic photovoltaic (OPV) cells.[54, 118, 195–197] There are some significant differences however, most notably the lack of a electrical contacts. These would need to be considered to determine the full impact of the described behaviour on the cell performance, and are neglected here to

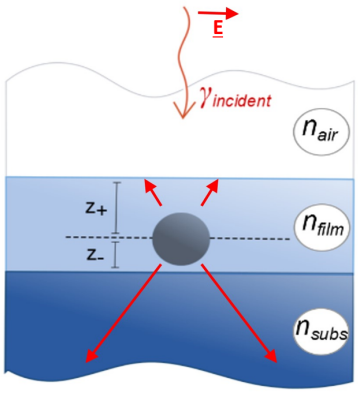

Figure 5.1: The general sample geometry used in simulations and experiments in this chapter.

concentrate on the fundamental properties of the particle-film interaction without being limited to the context of a single device design. Interestingly there is also an increasing interest in 2D materials such as graphene for electrical contacts, which could lead to cell structures which are much closer to the one shown in Fig. 5.1,[198, 199] although would still require individual analysis.

This report focusses on the behaviours of single nanoparticles in order to better distinguish individual mechanisms to inform and improve device design. Studies involving single nanoparticles have been shown to be a good approximation for the behaviour of random particle arrays, where NPs are spaced far enough to be non-interacting,[37] but ensemble effects such as grating interference from ordered arrays are outside the scope of this investigation. Only Silver nanoparticles are used, as Ag has been shown to be the material with the strongest plasmon resonance and the lowest interband losses.[95]

To investigate the effect of the thin-film structure on the LSP behaviour in spherical NP's this chapter will focus on three main behaviours: The first is the plasmon modes that are excited in the particle and how these are affected by the presence of the film. Secondly the strength of the interaction of the LSP modes in the particle with incoming light is measured in terms of the scattering and absorption cross sections, Q_{scat} and Q_{abs} respectively. The absorption cross section of a NP can be considered the area that a perfect absorber would occupy to absorb the same amount of light, and the scattering corss section can be treated in a similar way. These values are often normalised to the actual geometric cross section of the particle, and are therefore written as a unitless parameter that describes the absorption and scattering efficiency of a particle (see section 4.1.2). This is of interest as these values can be used to determine the surface coverage required for a random array to interact fully with incoming light, which is important for applications such as selective reflectors, antireflection coatings and solar cells.

The final property to investigate is the directional scattering of light. This will be discussed in terms of the angular scattering pattern from the particles and the fraction of

light that is scattered into the high index substrate, which is of interest for photovoltaics and single-photon collection. We use the factor F_{subs} to describe this, which is defined as F_{subs}=power scattered into substrate/total scattered power, as measured by a pair of transmission monitors in the simulation ((6) & (7) in Fig. 4.2) as discussed in section 4.1.2.

5.2 The effect of a thin film above a high index substrate

Perhaps the most immediately apparent effect of overcoating a particle on a substrate with a transparent film is that the dielectric conditions around the particle are altered. As discussed in section 2.3.1, this will have a significant effect on the modes and resonances excited. Figure 5.2 shows the optical scattering, Q_{scat} and absorption, Q_{abs} cross sections for 150 nm diameter spheres at a substrate-air interface with and without a 200 nm thick overcoating film ($z_+ = 200nm$) with n_{film}=1.5. The dipole (i), quadrupole (ii), and hexapole (iii) peaks are labelled. In Fig. 5.2(a), the addition of the film redshifts and broadens the scattering peaks for all excited modes - this occurs due to the RI increase in the environment of the NP, which causes a reduction in the charge separation within the particle: the restoring force, so the resonances occur at longer wavelengths.

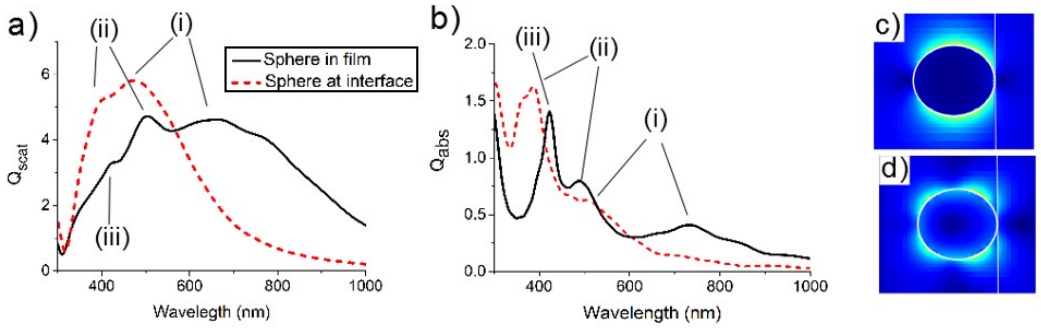

Figure 5.2: FDTD simulations of the scattering (a) and absorption (b) cross-sections for 150 nm Ag spheres at a bare interface (dashed lines) and with an overcoated film (solid lines) with particles resting on the substrate and the film height above the particle centre (z_+) at 200 nm. In these simulations, n_{subs}=1.8, n_{film}=1.5, & n_{air}=1. The dipole (i), quadrupole (ii), and octupole (iii) peaks are labelled. c) & d) show the electric field intensities of the dipole and quadrupole mode respectively.

The dipolar peak is shifted by 200 nm from 480 to 680 nm, whilst the quadrupole undergoes a smaller shift of 105 nm from 390 to 495 nm. For NP's at an interface, the dipolar mode at 480 nm is the dominant feature and scattering is weak at long wavelengths. With the addition of the film, spheres exhibit a much more broadband response, covering almost the entire spectrum. This is due to both the broadening of the dipolar peak through radiation damping and dynamic depolarization[96] and the higher RI of the film shortening the wavelength of light in the film, giving the particle a larger effective size and leading to the excitation of higher order modes - the quadrupole (ii) at 495 nm and hexapole (iii) at 420 nm. The presence of this additional layer therefore opens up a new mechanism alongside particle geometry to tune the resonance peaks to the desired range of the solar spectrum.

Figure 5.2(b) shows the absorption cross sections (Q_{abs}) of the particles. Each excited mode manifests itself as an absorption peak, with the highest-order mode for each particle having the largest peak value and the dipolar peak the lowest. This fits with the models described in section 2.2 where it was demonstrated that lower mode orders have greater radiative efficiencies for a given particle size. The addition of the film red-shifts all resonances whilst broadening the peak and reducing the maximum value from around 1.6-1.4. The greater spread of the absorption spectrum across the visible range could have negative consequences for some applications, especially for photovoltaics and care must be taken to minimise these losses when designing structures for practical applications.

In Fig. 5.3 the effect of the film on the directional scattering is displayed. Figure 5.3(a) compares F_{subs} for spheres both within the film and at a bare interface, showing that the addition of the film dramatically increases the fraction of forward scattered light across the visible spectrum. Here, much of the backscatter from spheres at large angles is caught by the film via total internal reflection (TIR) and reflected forward into the substrate, in an analogous way to a satellite dish coupling to an antenna for radio waves, significantly increasing the forward coupled fraction by an average factor of 1.41 overall and a factor of 1.23 in the dipolar region.

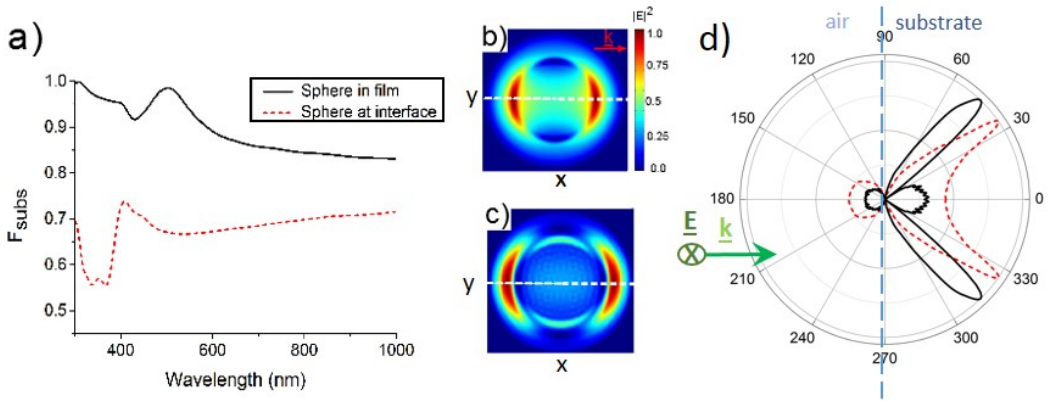

Figure 5.3: (a) Fraction of radiation scattered forward into the substrate for 150 nm Ag spheres at a bare interface (dashed line) and with an overcoated film (solid line) with particles resting on the substrate and the film height above the particle centre (z_+) at 200 nm. (b),(c) Fourier space scattering plots of light scattered into the substrate calculated in the far field for particles at a bare interface and in a film respectively. (d) Angular scattering distribution for both cases measured along the x-axis, perpendicular to the polarization; showing forward and backwards scattering. In these simulations, n_{subs}=1.8, n_{film}=1.5, & n_{air}=1. Scattering patterns are measured at 700 nm.

The interference between directly scattered radiation and radiation reflected from the film-air interface (as discussed in section 3.1) has a significant effect on the far-field scattering pattern of the particle, as shown in Fig. 5.3(b)-(d). With the addition of the film, the angular scattering is dramatically altered with significantly more light scattered to higher angles and a much greater concentration in the high-angle lobes. This is behaviour is extremely useful for increasing the directionality of light for antennae, and for coupling light into the waveguide modes of a substrate and shall be considered further in section 6.3. The directional profile of the backscattered light does not change significantly for normally incident radiation, and the change in the intensity of backscatter is covered in the F_{subs} parameter and so from this point on only angular scattering into the substrate will be discussed.

The light scattered from higher-order modes must also be considered. For particles at an interface, a dramatic drop in forward scattering for shorter wavelengths occurs around the quadrupole resonance. In Figure 5.4(a) this can be seen to be due to an increase in forward scattering just above and reverse scattering below the quadrupole resonance at 395 nm. Figure 5.4(b) demonstrates a significant amount of backscatter just below the quadrupole resonance at 375 nm for a particle at an interface. Such sudden switches in directionality have been predicted for particles in free space and

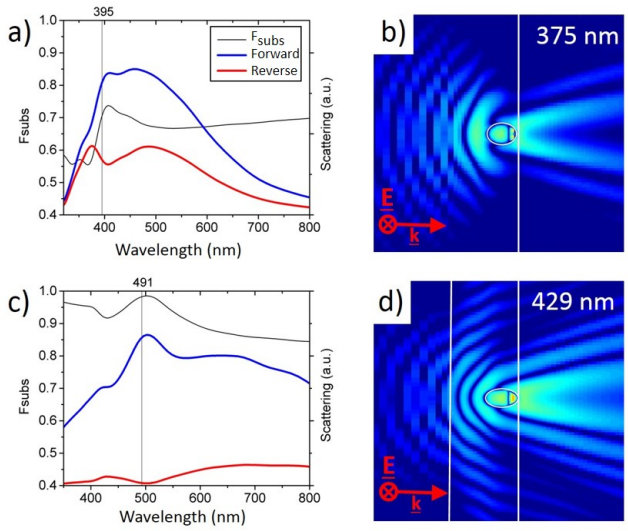

Figure 5.4: (a) Showing the forward (blue) and backward (red) scattering along with the fraction scattered forward into the substrate (F_{subs}, black) for a 150 nm Ag NP at a bare interface. (b) Normalised electric field intensity plots of a cross section of the particle at the peak backscatter wavelength of 375 nm. (c) Spectral scattering and (d) electric field intensity plots at 429 nm for an identical NP with an overcoating film where $z_+ = 200$ nm. In these simulations, n_{subs}=1.8, n_{film}=1.5, & n_{air}=1.

are attributed to a Fano interference between the broad dipole and narrow quadrupole modes,[110, 111] as discussed in section 2.4.

The addition of the film has a drastic effect on this short-wavelength drop in F_{subs} and leads to an extremely high forward coupling where there was previously a loss, as can be seen in Fig. 5.4(b). This reduction of the observed Fano effect is partially due to the broadening of the quadrupole mode in the film due to the increased RI, which reduces the intensity of the Fano interference. The main factor however is the coupling of light to the quasi-waveguide modes of the film, which then leak into the substrate, as shown in Fig. 5.4(d). Therefore by overcoating a metal particle on a high-index substrate with a low-index film, it is possible to not only reduce dipolar backscattering, but also to suppress short-wavelength losses from Fano interference due to higher order modes.[200] For applications seeking to use the Fano behaviour for sensing[109, 110, 201] this would be detrimental, but to construct a short-wavelength anti-reflection coating,[202, 203] or to couple to an optical waveguide of solar cell this removes a significant loss mechanism that has not been addressed previously.

5.3 Exploring the parameter space

It has been shown that by placing a NP in a thin-film structure, the scattering and absorption resonance peaks can be manipulated and the directional scattering behaviour altered significantly, leading to a more finely structured emission pattern, a notable reduction in backscatter and the suppression of Fano losses. To utilise this structure for any given application, the effect of every variable on the strength and resonance wavelength of the plasmon modes excited in the particles and the interference of scattered light must be well understood. To that aim, the following section presents a parameter space investigation of the particle-in-film system.

5.3.1 Index of the film

The effect of the refractive index of the film on the scattering and absorption cross-sections of a NP is displayed in Fig. 5.5 where the RI of the layer containing a 100 nm Ag sphere is varied between $n_{film} = 1$, the case of a particle at a bare interface, and $n_{film} = 2.2$, a value greater than that of the substrate.

In Fig. 5(a), it is clear that raising n_{film} redshifts and broadens all of the particle resonances; the dipole peak shifts over 400 nm over the range considered and broadens its FWHM from 101 to 301 nm, compared to a 215 nm shift for the quadrupole mode, and a FWHM shift from 22 to 127 nm as determined from lorentzian curve fitting. This behaviour has been observed previously and is very similar to that discussed in section 2.3.1, for the case of a sphere in a uniform dielectric. As can be seen in Fig. 5.2(c)&(d), there is minimal coupling of the modes of the spheres to the substrate and for a film that coats the particle beyond the near field range (about 20 nm), the comparison with spheres in a uniform dielectric is a good one. This is not the case for all particle geometries however, in the next chapter the substrate and film will be shown to have a dramatic effect on the modes in flatter and longer particles.

The redshifting of the dipolar peak was measured experimentally using the optical setup in section 4.5.2 connected to a spectrometer. The scattering of white light from 107 nm

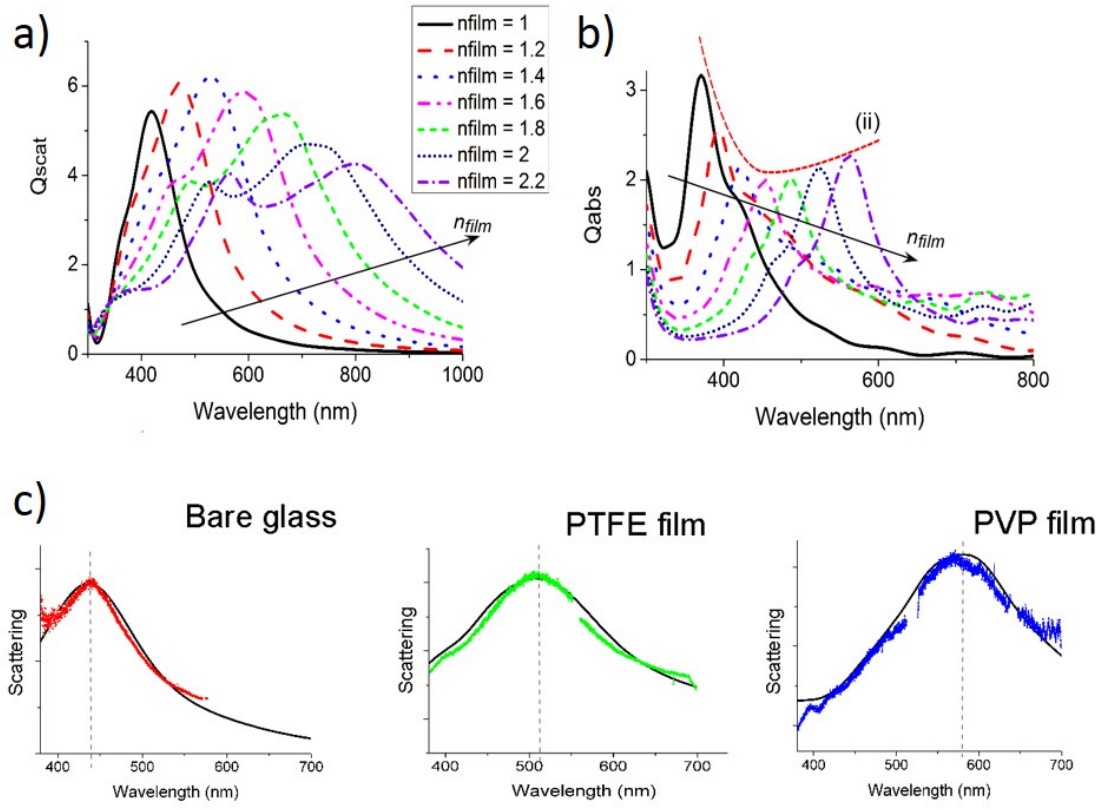

Figure 5.5: The scattering, (a) and absorption (b) cross sections of 107 nm Ag spheres in the structure defined in Fig. 5.1. The spheres were placed upon the substrate with $z_+ = 200$ nm, $n_{subs} = 1.8$ and n_{film} varied between 1.0 and 2.2. (c) Experimental (coloured lines) and simulated (black lines) forward scattering for 100 nm Ag NP's on a glass substrate, and with the particles overcoated with 200 nm of PTFE AF and PVP.

NP's is measured for particles on a bare glass substrate, and particles overcoated with a PTFE AF or PVP film, with refractive indices at 600 nm of 1.31 and 1.465 respectively. The breaks in the measured spectra are discontinuities due to the spectrometer changing gratings and the deviations below 400 nm and around 700 nm are probably due to the spectrometer not producing a flat response at these limits. Aside from this a good agreement between theory and experiment can be observed, which supports the use of FDTD methods to investigate this structure.

The directional scattering behaviour is also affected by film index. The fraction of photons scattered into the substrate for various values of film index, n_{film} is shown in Fig. 5.6(a): increasing n_{film} up to that of the substrate, n_{subs} leads to an increase in the fraction scattered forward across the spectrum up to a factor of 1.3 compared to a particle at a bare interface when $n_{film} = n_{subs} = 1.8$. This can be attributed

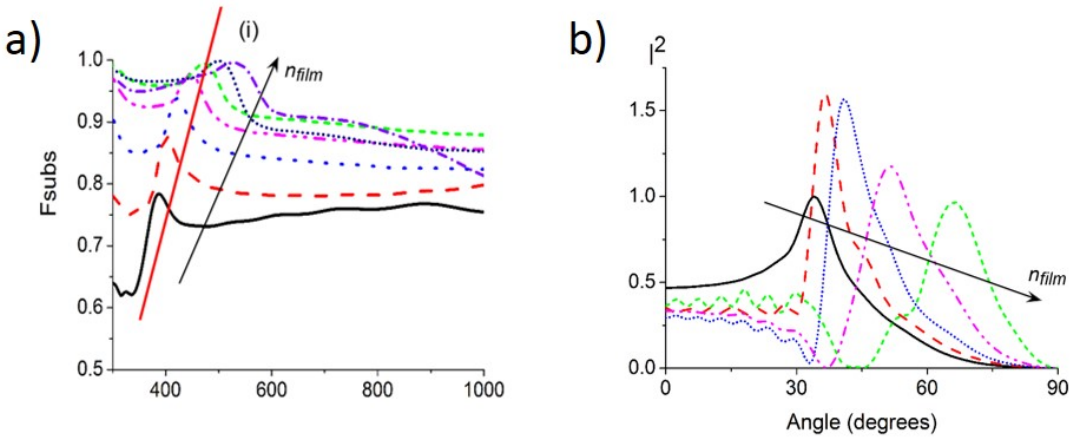

Figure 5.6: (a) The forward scattering fraction & (b) angular scattering distribution measured across the x-axis of a Fourier space plot, for 100 nm Ag spheres placed upon the substrate with $z_+ = 200$ nm, $n_{subs} = 1.8$ and n_{film} varied between 1.0 and 2.2.

to the increased contrast between the index of the film and the upper half space, leading to stronger reflection from the upper interface and TIR across a wider range of angles, producing greater re-scattering in the forward direction. For 150 nm spheres, a maximum enhancement factor of 1.45 was found, the greater value largely due to the increased influence of higher order resonances. The Fano peak (i) at around 400-600 nm, which was observed earlier in Fig. 5.4, can be seen to redshift in step with the quadrupole peak and the drop in forward scattering for shorter wavelengths reduces as the RI is raised. When $n_{film} > n_{subs}$, the situation changes somewhat and in the dipolar zone a marked decrease in F_{subs} can be observed. This is due to the fact that some large-angle emission from the dipolar region will now be trapped within the layer via total internal reflection and so will no longer contribute to forward scattering.

Figure 5.6(b) shows the far-field scattering pattern along the x-axis at the dipolar peak. As n_{film} is raised, the reflection conditions at the interfaces are altered and the optical path length within the film increases. The peaks also broaden as the large-angle evanescent contribution gains significance with the reduction of the RI gradient.

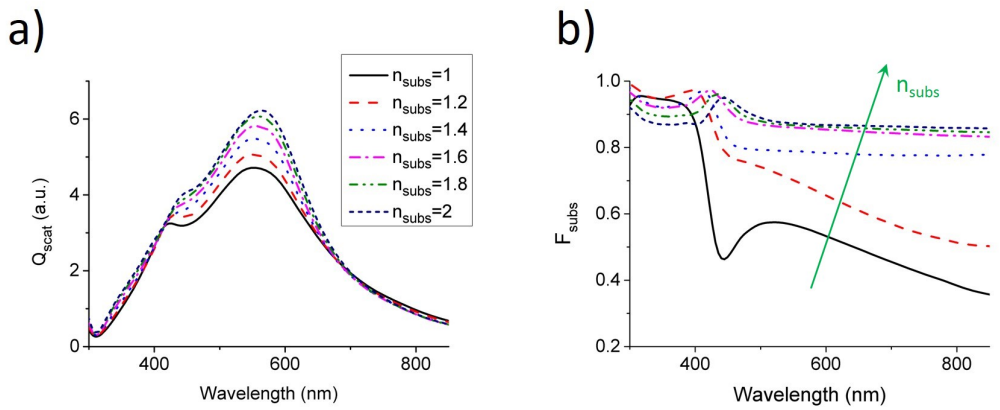

Figure 5.7: (a) Q_{scat} and (b) F_{subs}, for 100 nm Ag spheres in the thin film structure with $z_+ = 200$ nm, $n_{film} = 1.5$ and n_{subs} varied between 1.0 and 2.0.

5.3.2 Index of the other layers

As a spherical particle has very little contact with the layers either side of the film, one would not expect altering their refractive index to have much of an impact on the resonances. In Fig. 5.7(a) it can be seen that this is generally the case: the dipole peak shifts a total of 12 nm when n_{subs} is changed from 1 to 2.2, which is negligible compared to the 180 nm shift with an equivalent variation of n_{film}. However, the scattering efficiency is seen to shift significantly due to the changing reflection conditions at the film-substrate interface, which leads to a different driving field (the sum of the incident and reflected fields) at the particle center. The scattering efficiency is proportional to the driving field intensity[38] and so whilst the substrate can be chosen at will with a negligible effect on the resonance position, care must be taken ensure the driving field at the particle centre is at a maximum, which can also be achieved by changing the film thickness as discussed in the next section.

Figure 5.7(b) shows that as long as $n_{subs} > n_{film}$, the fraction of light scattered forward into the substrate is relatively unaffected by n_{subs}. For $n_{subs} < n_{film}$ TIR at the film-substrate interface becomes a significant problem, with a fraction of scattered radiation becoming trapped in the film and leading to a reduction of F_{subs}. This fits with the model described in section 3.1 and implies that the enhanced forward scattering due to the presence of the film is primarily due to wide-angle reflection at the film-air interface.

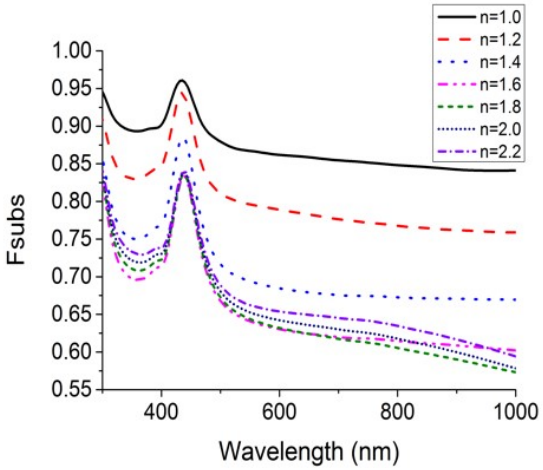

Figure 5.8: F_{subs} values for 100 nm Ag spheres in a thin film structure with $z_+ = 200$ nm, $n_{film} = 1.5$, $n_{subs} = 1.8$ and n_{air} varied between 1.0 and 2.2.

The importance of reflections from the film-air interface is reinforced by examining the effect of altering the index of the top layer, as in Fig. 5.8. As n_{air} is increased, there is an extremely rapid reduction in the forward coupling; a minimum is reached when $n_{air} = n_{film}$ and beyond this a slight increase due to weak reflection from the RI mismatch. This behaviour could be extremely problematic for using these particles in thin-film cells, as the active layers typically lie beneath a transparent conducting oxide, which typically have an RI significantly greater than P3HT:PCBM, which would dramatically reduce forward coupling and the light collected by the cell. This could be counteracted using a 2D material such as graphene as the front contact. For high-index inorganic cells such as silicon and gallium-arsenide with indices of 3.94 and 3.92 respectively (at 600 nm), this effect is less of an issue as their very high RI makes index matching less of a problem.

5.3.3 Particle position in the film

Electric field strength

Whilst careful selection of the refractive indices provides a great deal of tunability, the dimensions of the film and the position of the particle within are also key to optimising the power and directionality of the scattering. The most important mechanism here is

interference in the film, but near-field coupling to the substrate is also a factor. The electric field strength at any given point in the film depends exclusively on the film thickness and refractive index of the layers, therefore care needs to be taken to ensure that the particle position and properties are balanced to ensure the greatest driving field and hence scattering power at the particle center. In this section all RI values are taken as previously with: $n_{air} = 1, n_{film} = 1.5, n_{subs} = 1.8$.

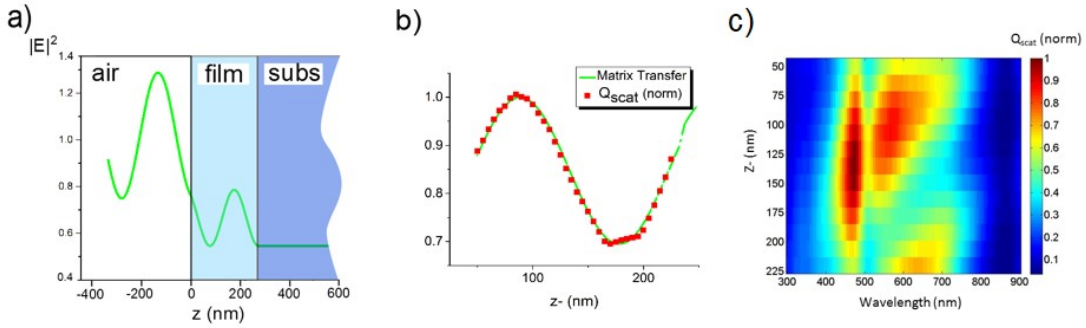

Figure 5.9: (a) Plot showing the magnitude of the electric field intensity (normalised to incident field) in the structure in the absence of a nanoparticle with $z_+ = 200$ nm and $z_- = 50$ nm under normal 560 nm illumination. (b) Normalised scattering cross section at the dipolar peak (560 nm) for a 100 nm Ag sphere with a variable distance between the particle centre and the substrate, z_- matched with transfer matrix simulations for the driving field at the particle center. (c) Q_{scat} values across the solar spectrum with changing z_-. In these simulations, n_{subs}=1.8, n_{film}=1.5, & n_{air}=1.

The total electric field at the centre of a 100 nm particle resting on the substrate with $z_+ = 200$ nm whilst the thickness of the film below it is varied was calculated using the transfer matrix method. For light incident from the air side, the interference from incident and reflected components leads to a standing wave formation within the film and in the air above, whilst only transmitted radiation exists in the substrate, as shown in Fig. 5.9(a). Comparing the results with the scattering cross section of a 100 nm NP at the dipole resonance at 560 nm, (Fig. 5.9(b)) an excellent agreement between simulation and theory is observed, confirming that the scattering power is entirely dependent on the interference conditions within the film. For Fig. 5.9(c), the scattering cross section across the spectrum was simulated and it can be observed that the quadrupole mode also exhibits a similar dependence.

Interference conditions for scattered light

Once excited, the coupled surface charge oscillation constituting an LSP will eventually decay, mostly through re-emission (scattering) for a ∼100 nm particle. Most scattered light is emitted directly into the film (some is coupled into the substrate through the near field) and the interference between incident radiation, scattered light and light reflected from the interfaces produces well defined angular emission patterns which can be observed in the far field. These emission patterns are entirely defined by the interference conditions and are thus very sensitive to the optical path lengths within the film. To investigate this dependence, the thickness of the film above (z_+) and beneath (z_-) the particle are investigated separately in order to isolate their individual effects.

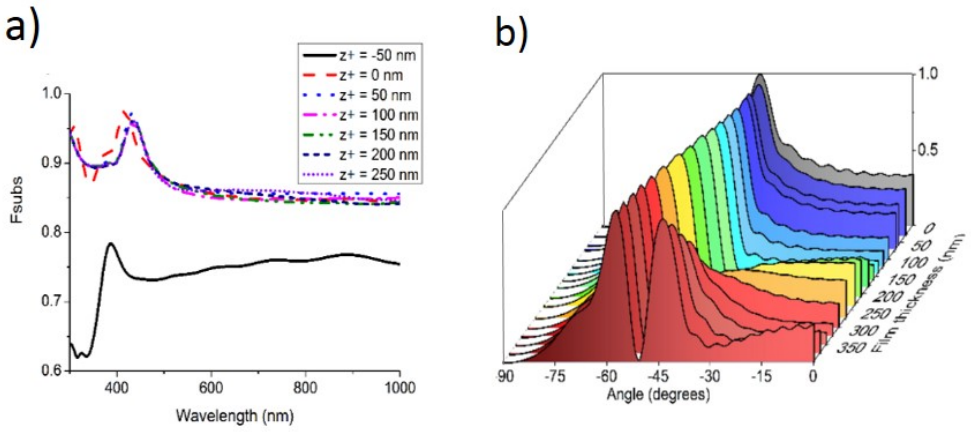

Figure 5.10: (a) F_{subs} for different film heights, z_+ above a 100 nm Ag NP resting on the substrate. (b) Far-field scattering pattern traces measured perpendicular to the incident polarization for varying z_+. In these simulations, n_{subs}=1.8, n_{film}=1.5, & n_{air}=1 and the incident radiation has a wavelength of 532 nm.

In the presence of an overlaying film, since $n_{air} < n_{film}$, total internal reflection at the film-air interface is a significant factor and much initially backscattered light is caught and reflected forward, as described in equation 3.5, producing a very high F_{subs} value across the optical spectrum. Figure 5.10(a) shows the effect of altering z_+ on F_{subs} values, demonstrates that as soon as the centre of the particle is covered by the film, strong forward coupling is achieved, and further thickness increases have a minimal impact. It is worth noting however that this value is normalised to the total scattered

power, and so does not take into account variations due to the changing driving field discussed earlier which would be observed in practice.

Whilst the fraction of light scattered forwards remains mostly unchanged with varying z_+, the directional emission of the dipolar mode is modified significantly, as shown in Fig. 5.10(b). The maximum of the scattering lobe is seen to shift to larger angles and further lobes are excited as film thickness is increased. This behaviour is in agreement with the theory of dipolar emitters in multi-layered structures as defined by Lukosz [128] and is due to the interference between directly scattered light and light then reflected from the various interfaces. As the film height above the particle, z_+ increases, the interference maxima shift to larger angles and new maxima begin to form close to the center, until z_+ becomes large compared with the wavelength and we arrive at the case of a simple interface between the substrate and a half-space with the RI of the film. Thus the majority of the light will be scattered into one or more pairs of well-defined lobes, and the concentration of light within a given angular spread will be dependent on z_+. The confinement of light within the lobes along with the fraction scattered beyond the critical angles of the structure is discussed further in section 6.3.

To verify these simulations, the impact of the film thickness on the directional scattering of individual Ag NP's in a thin-film structure was investigated experimentally for the first time using the custom-designed microscope described in section 4.5.2. Figure 5.11 shows the simulated (a)-(d) and measured (e)-(h) Fourier space scattering patterns of bare NP's above a glass coverslip and those overcoated with 89 ± 7, 185 ± 5, and 247 ± 4 nm PTFE AF films. Simulations were conducted using the average measured film thicknesses and particle sizes. The normalised line traces across the vertical axes of experimental and simulated plots are also shown in (i)-(l). The scattering pattern is shown to be defined by the thickness of the film containing the particle. As the thickness increases from (a)-(d), the lobe peak moves outwards from 41^o to 54^o from the optical axis and the emission at low angles reduces from 50% of the peak value in Fig. 2(i) to 17% in Fig. 2(k), before increasing again and beginning to form a secondary pair of lobes, which have just started to emerge in Fig. 2(l). The experimental results show strong agreement with simulations, once the effect of the mirror patchstop at the centre

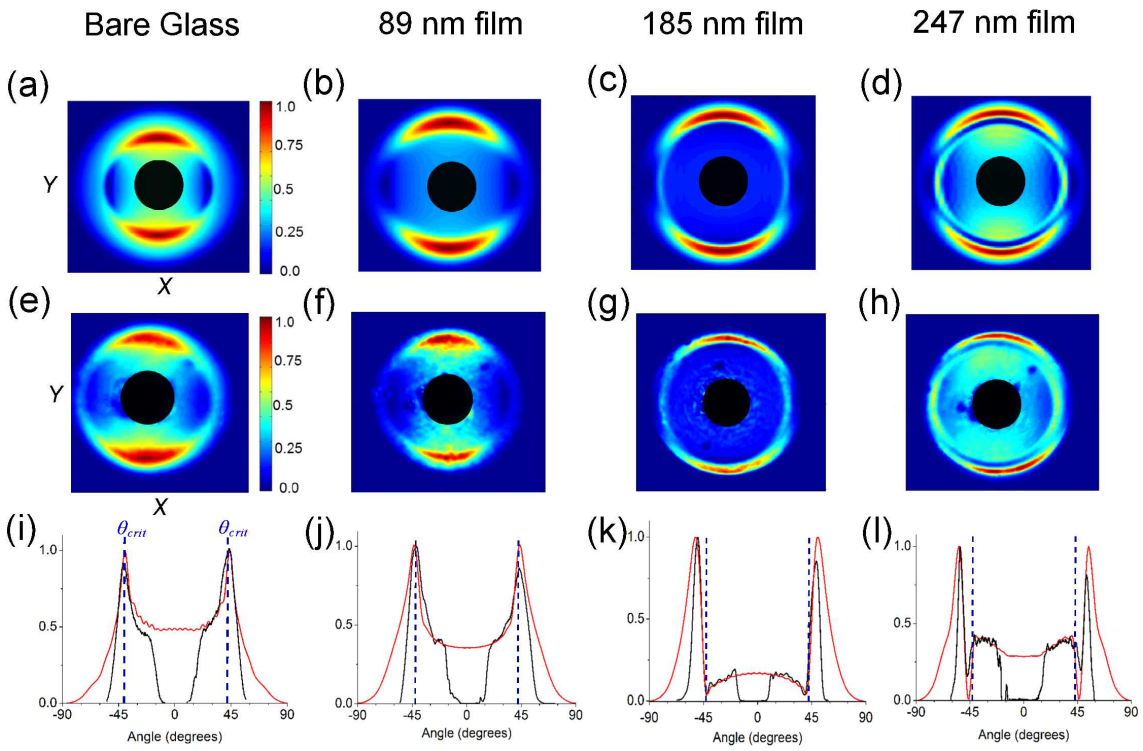

Figure 5.11: FDTD simulated (a)-(d) and experimental (e)-(h) Fourier space images of scattering patterns from 107 nm Ag nanospheres at an air-glass interface ((a), (e), and (i)) and overcoated with 89 nm ((b), (f), and (j)), 185 nm ((c), (g), and (k)) and 247 nm ((d), (h), and (l)) of PTFE AF. Plots (i)-(j) show line traces across the vertical axis of all plots to better compare theory (red lines) and experiment (black lines). The air-glass critical angle θ_{crit} is displayed as a dashed blue line. Here, n_{subs}=1.52, n_{film}=1.31, & n_{air}=1 and illumination is provided by a green laser at 532 nm.

and the NA of the objective lens are taken into account, highlighting the impact of the film on directional scattering and experimentally verifying the use of the dipole model for spheres. This is the first experimental observation of the angular scattering patterns of individual metal nanoparticles in thin films and is an important confirmation of the simulations in this chapter.

The interaction of the particle with the substrate-film interface is somewhat different. Whilst the thickness of film above the particle made little difference to the fraction of scattered light coupled into the film, it can be seen in Fig. 5.12 that altering z_-, the distance to the substrate, has a marked effect. As z_- increases, F_{subs} in the dipolar regime drops away, which is due to a reduction in the near-field coupling to the substrate. Particles at a bare interface show a reduction in F_{subs} of 5% across the dipolar regime for the distances considered, compared with 2.5% for MNPs in a film. The smaller reductions of forward scattering in the presence of the film is due to both

the film catching some of the radiation that would generally be back-scattered for an increase of z_- at a bare interface and the reduction in the RI gradient between the layers, meaning that a given increase in distance from the substrate results in a smaller change in the near-field coupling.

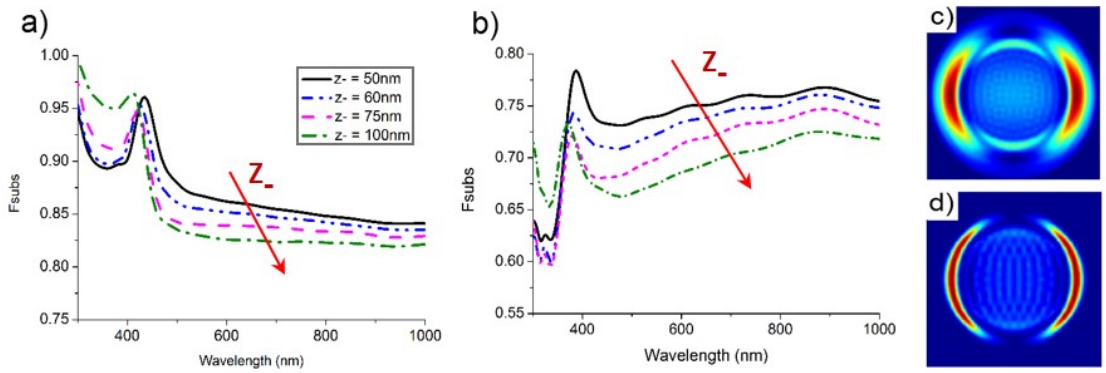

Figure 5.12: FDTD simulations of the fraction of radiation scattered forward by 100 nm spheres for varying distance from the particle centre to the substrate (z_-) for NP's in a thin film (a) and at a bare interface separated from the high-index substrate by a spacer layer with the same index as the film (b). (c) and (d) are Fourier-space plots showing the far-field scattering pattern for the particle at $z_- = 50$ and 125 nm, respectively, under 700 nm illumination. In these simulations, n_{subs}=1.8, n_{film}=1.5, & n_{air}=1.

The effect of the de-coupling of the near field can also be seen in Fig. 5.12(c)&(d), where z_- is increased from 50 nm, where the particle is resting on the substrate to 125 nm and the reduced presence of the evanescent near field in the substrate leads to a dramatic reduction in light scattered beyond the critical angle at 41^o, and also a reduction in small angle scattering, producing a more well-defined emission pattern, which could be useful for nanoantenna applications.[61, 194]

5.4 Conclusions

The results of this chapter have shown that a silver nanoparticle placed within a thin film structure displays markedly different scattering properties compared with an identical particle at a simple interface. This behaviour can be explained primarily by interference due to reflection at the interfaces, affecting both the driving field exciting the particle modes and the directional scattering of radiation by the particle. Careful tuning of the film properties and particle position provides a route to improve forward

scattering across the entire optical spectrum and to maximise scattering to larger angles, which will be of significant benefit to light trapping applications. The RI of the film will also affect the resonances of the plasmon modes however, and so it is important to take a holistic approach to determine how the thin film impacts every aspect of the plasmonic scattering.

The addition of a dielectric film above a NP at an interface where $n_{air} < n_{film} < n_{subs}$ was seen to significantly enhance the fraction of light scattered into the substrate through the coupling of scattered light to the quasi-waveguide modes of the layer. These then leak into the substrate whilst the RI gradient prevents leakage at the film-air boundary leading to strongly reduced backscatter. Short wavelength backward scattering due to Fano interference between the dipole and quadrupolar modes was found to be almost entirely suppressed by the film, which could be used to significantly improve broadband light trapping. Careful choice of n_{film} was shown to provide additional tunability of the resonances and increase the optical path length in the substrate. It was found that films with RI values not conforming to $n_{air} < n_{film} < n_{subs}$ could show a reduction in F_{subs} in the dipolar regime, highlighting the importance of placing plasmonic scatterers in a region where these conditions can be fulfilled. The high refractive index of most common TCO's can make this difficult in OPV cells. A degree of control over the emission pattern has been achieved through adjusting the properties of the film, allowing for scattering to a more tightly confined angular range, which could be of interest for nanoantenna research and will be discussed further in the following chapter.

A custom-built dark field Fourier space microscope was utilised to experimentally explore the influence of film thickness above an individual NP on its angular scattering pattern for the first time. The results showed excellent agreement with simulations, and the microscope allows the observation of a greater angular range than other existing dark-field designs. This is utilised further in the next chapter to explore scattering from other NP shapes.

This study is a useful reference for anyone attempting to add plasmonic scatterers

to a planar thin-film structure, but further work would be required to optimise their behaviour in a given device. For example, there are effects that would be present in a PV structure that have not been discussed here, such as interference from adjacent particles, thin substrate layers and reflection from metallic back contacts. To investigate these effects would require the choice of an individual cell structure, as the impact of a NP layer on a ∼100 nm nm thick OPV and a 2 μm a-Si cell would be radically different, and would make a fascinating area for future study.

The next chapter will build upon these results to investigate the effect of a thin-film structure on the behaviours of flat-sided and elongated particles.

Chapter 6

Flatter and longer - other particles in thin films

Sections 6.2 and 6.3 of this chapter are based around the paper 'Directional plasmonic scattering from metal nanoparticles in thin-film environments'[142] by Powell et al., but also contain additional unpublished material.

The results of the previous chapter have given a detailed picture of the effect a thin-film environment has on the behaviour of plasmon modes in individual nanospheres. However, whilst spherical NP's provide a good starting point to explore particle-structure interactions due to their highly symmetric shape, which also makes them comparatively simple to fabricate via wet synthesis,[204] they are not necessarily the ideal shape for use in many applications. Flatter particles, with a greater surface interaction have been shown to produce better forward coupling at a bare interface[5] and are therefore of significant interest for light trapping in photovoltaic cells. Elongated particles have been shown to have more directional scattering[61, 137] and so are more useful for waveguiding or nanoantenna purposes.

In this chapter, nanocubes (NC's) and nanohemispheres (NH's) are chosen as two of the most readily fabricable flat particles to explore the impact of a thin film on differently

shaped NPs. Nanocubes can be wet synthesised[148] and hemispheres can be produced in a straightforward manner by annealing a thin Ag film,[205] where the film re-forms into metal islands to reduce the surface area and maximise the total energy of the system.[9] The impact of an overcoated dielectric film on the excited modes, spectral extinction and spatial scattering is simulated for these particles and compared with the behaviour of spheres. There is some difficulty in comparing differently shaped particles, as if one parameter, e.g. NP volume is chosen to be equal, then others, such as cross section might be different, and so there is some size dependency that needs to be taken into account. In this investigation the width of all particles is set at 100 nm. An effort is made to discuss general trends specific to the particle shapes and it should be remembered that some parameters, such as coupling to the substrate could be fine-tuned by altering the particle size, but this will not be discussed in detail here. For the interest of the reader, there is a brief investigation of the effect of size on substrate coupling and of the height of flat particles in works of Catchpole et al.[5], and Mokkapati et al[206] respectively.

The scattering from extended Ag nanowires (NW's) is also investigated experimentally and demonstrates a ready means to produce a tightly confined scattering pattern. The achievable angular confinement is compared with other methods in the literature. The ability to enhance the angular confinement of light scattered by the particles by tuning the film thickness is discussed and compared to other optical nanoantennas. The final part of this chapter explores the potential application of using NW scattering to create a novel humidity sensing element.

6.1 Flatter - cubes and hemispheres

The principal difference between round and flat sided particles is the strength of their interaction with the substrate. As discussed in section 3.3, when a metal NP supporting a plasmon mode approaches a dielectric, the substrate material polarises to screen the electric field from the charge separation in the particle. The screening field is not uniform across the particle and thus the symmetry is broken, altering the structure of

the modes from the original geometry and removing the orthogonality of the basis set. This can lead to a mixing of the dipole and quadrupole modes especially, producing hybrid modes which can interact strongly with the substrate. This effect is much stronger for flat-sided NP's, as they have significantly greater contact with the substrate than spheres.

One of the most influential papers on plasmonic light trapping for PV in 2008 found that the large surface area of flatter particles also led to better coupling of scattered light into a high-index substrate, reducing back reflection compared with other shapes.[5] Since then, the majority of publications investigating light trapping via large angle scattering from plasmonic particles have studied some manner of flat sided particle.[27, 37–39, 42, 46, 98, 117, 205, 206] A few groups have modelled the silver NP's produced by annealing a ∼10 nm film (Fig. 6.1) as spheres,[46, 126, 203] but most studies agree that these are better thought of as flat sided particles such as hemispheres, as shown in Fig. 6.1(b), although they are generally modelled at bare interfaces despite their placement within thin films.

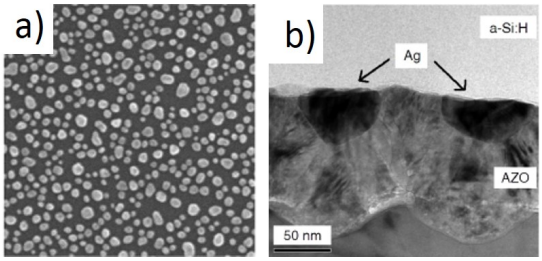

Figure 6.1: From Santbergen et al. [205]: (a) Silver island film on Si mass annealed at 200 C from a 5 nm thick Ag film showing an area of 1x1 μm^2. (b) TEM image of silver nanoparticles embedded in the rear oxide of an amorphous Si solar cell showing the hemispherical nature of the particles.

Enhancement from nanocubes on the surface of a cell has been simulated in a few investigations[51, 207] but the origins of the increased active layer absorption compared with other NP shapes has not been studied in depth, and despite being readily fabricable via wet synthesis the predicted enhancements from nanocubes have not been verified experimentally. Several reports have utilised disk-like particles,[27, 38, 104, 117, 126, 206] which are difficult to produce in a scalable manner. More exotic shapes such as nucleated particles[59] and nanocups,[208] have also been explored. These are both produced by wet synthesis and have the potential for increased tunability of the angular scattering.

6.1.1 Cubes

The mode structure and spectra of flat particles, and especially cubes at an interface have been studied in several reports,[113, 114, 209] but their directional scattering properties, and the impact of a thin-film structure are yet to be examined. Fig 6.2 shows the extinction cross sections of 100 nm Ag nanocubes in free space, on a substrate where n_{subs} =1.8, and on a substrate and overcoated with a film where $z_+ = 200$ nm, $n_{film} =$ 1.5 as in the previous chapter. In the free space case, the dipolar (I) and quadrupolar (II) modes can be seen clearly in the FDTD simulations of the scattering cross sections and the electric near field. When the NC is placed on a dielectric substrate the mode hybridisation first seen by Sherry et al[113] is observed. There is a strong shift of the mode concentrated about the substrate (I), which has been shown to originate from the dipole[114] (see section 3.3) caused by charge screening from the image dipole induced in the high index substrate which reduces the net charge separation of the plasmon and weakens the restoring force. The upper, mode (II), which originates from the quadrupole is far from the substrate and so only weakly affected.

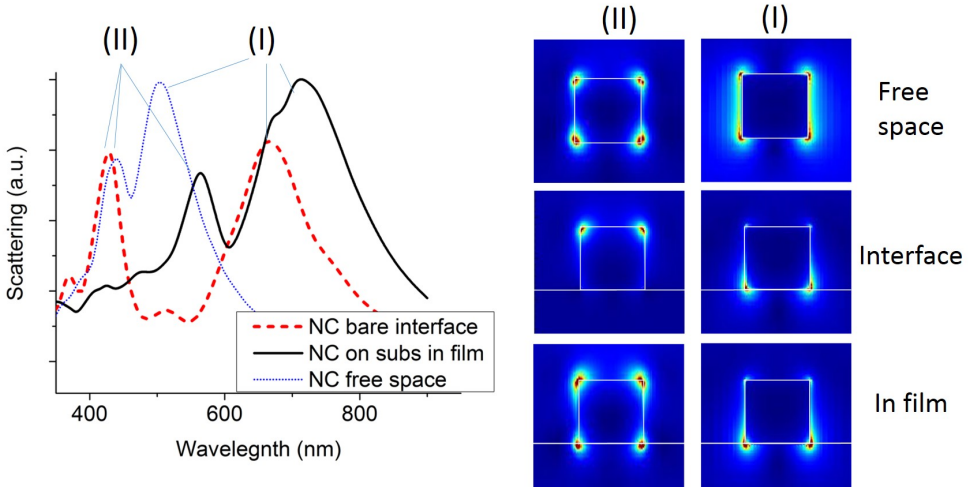

Figure 6.2: FDTD simulations of the spectral scattering (left) and electric field strengths of the excited modes in 100 nm Ag nanocubes in free space, on a substrate where n_{subs} =1.8, and on a substrate and overcoated with a film where $z_+ = 200$ nm, $n_{film} = 1.5$. Electric field plots are taken at the wavelength of the peak resonance of the corresponding mode.

On the addition of the film, there are two notable effects: Firstly the resonance of both modes is seen to redshift, mode II is seen to shift 135 nm and mode I shifts only 47

nm, which is to be expected as mode I on the lower face interacts much more strongly with the substrate than with the surrounding medium and so will be less sensitive to the RI of the film. Thus by altering the substrate and dielectric surroundings it is possible to tune each mode of a nanocube with some degree of independence, allowing the positioning of the strongly scattering mode I about a spectral region of interest whilst reducing the negative effects of the more strongly absorbing mode II in this area.

The second directly observable effect of the film is the reduction of the mode hybridisation. The electric field plots show that mode II appears much more quadrupole-like in the film, leading to a much stronger substrate interaction than in the case of a bare interface. The field of mode I is still quite concentrated in the substrate, although there is an increase in the field along perpendicular vertices and upper face, again demonstrating a reduction in hybridisation.

This behaviour is potentially worrying for light trapping applications, as the reduction in coupling of mode I to the substrate could be expected to reduce F_{subs}. Figure 6.3 plots the forward coupled fraction for a cube at a bare interface, in a film with z_+=200 nm and at an interface where the RI of the upper half-space is equal to that of the film. In this last situation it can be seen that raising the RI about the NC *does* result in a substantial reduction in forward scattering across most of the spectrum due to the weaker coupling to the substrate, although below around 550 nm the reduced hybridisation leads to an enhancement due to *better* coupling from the upper face mode, as shown in Fig. 6.2. However, when this environment is a thin film, the F_{subs} value is raised significantly, demonstrating that the interference effects due to the thin-film geometry produce a stronger forward scattering across the

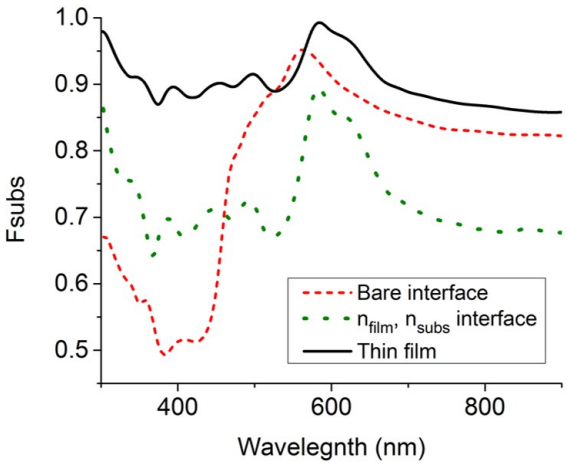

Figure 6.3: Forward coupled fraction, F_{subs} of the a cube at a bare interface, in a film with z_+=200 nm and at an interface where the RI of the upper half-space is equal to that of the film. In these simulations, n_{subs}=1.8, n_{film}=1.5, & n_{air}=1.

optical spectrum, despite the weaker near-field coupling due to the reduced RI gradient, once again demonstrating the effectiveness of the structure as a dielectric antenna for efficient forward coupling.

6.1.2 Hemispheres

Despite the widespread use of hemispherical particles for exploring light trapping in solar cells, there have been very few studies investigating the effects of a substrate, or thin film structure on the plasmon modes and almost no work on their directional scattering behaviour.[5, 210] Whilst a full analytical description of the behaviour of these particles is beyond the scope of this investigation, there are several interesting traits that can be readily observed and investigated using FDTD simulations, which will be discussed below.

An interesting feature of NH's, is that for the size range typically considered there is only one strong mode, and higher order terms are extremely weak, this is due to the lack of symmetry of the particle not allowing for equivalent charge separation at the top and bottom faces required to produce a strong quadrupole. The dipolar mode (I) is concentrated about the corners of the particle and the influence of the substrate is observed to have a very limited impact on the mode structure, although the charge-screening effect again leads to a significant redshift, as shown in Fig. 6.4(a).

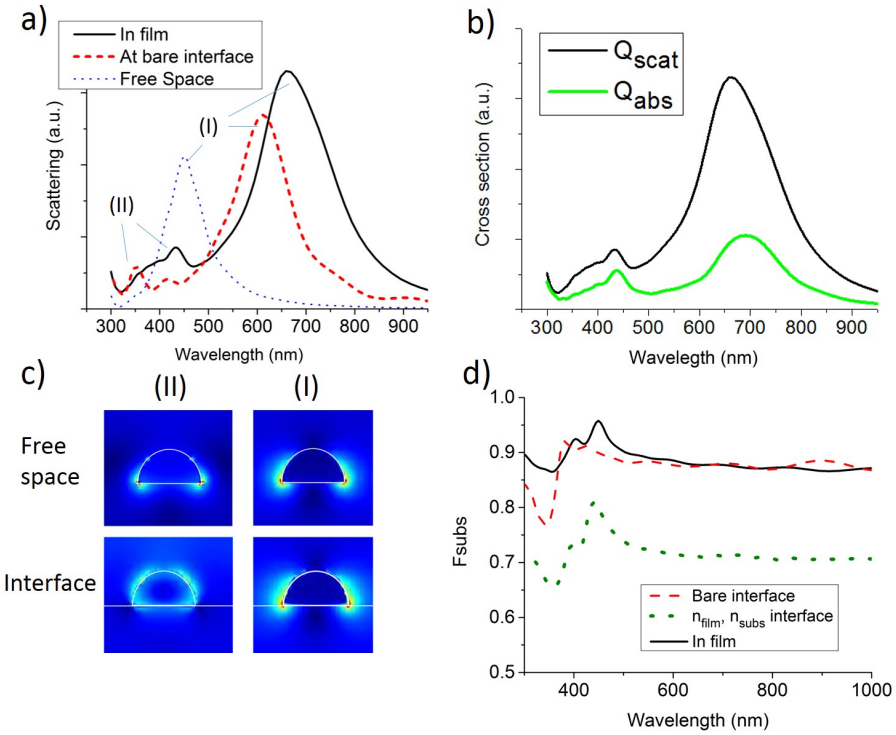

Figure 6.4: (a) Scattering spectra of 100 nm Ag hemispheres in free space, at an interface and overcoated with a thin, 200 nm thick film. (b) Scattering and absorption spectra of a 100 nm Ag hemisphere in a film. (c) Electric field plots for modes I and II of NH's in free space and at an interface, taken at the wavelength of the peak resonance of the corresponding mode (d) Forward scattering fraction for NH's at an interface and in the thin film structure. In these simulations, n_{subs}=1.8, n_{film}=1.5, & n_{air}=1.

As the quadrupole mode is so weak, the absorption is concentrated about the dipole, as highlighted in fig. 6.4(b). This is in direct contrast to the spheres in the last chapter, where it was found that the absorption was strongest about the highest order mode excited, and cubes where absorption is principally concentrated about the upper face mode[113], and could prove problematic for PV enhancement. Due to the lack of differentiation between the case of free space and an interface, and as the differences expressed in the modes in the film are even more subtle, and an E-field intensity plot for this case is not shown. In the film the peaks are redshifted again due to the increase in the RI of the surroundings, and again mode I experiences a smaller relative RI increase around it and so shifts less than mode II, with shifts of 50 nm & 80 nm respectively.

The forward scattering of the NH at first appears mostly insensitive to the addition of the film, as shown in Fig. 6.4(c). The extremely strong forward scattering without

the film is due to the low profile of the particle, which lowers the effective distance of the charge separation to the interface. However, reducing the RI gradient does reduce the coupling significantly as shown in the case where the upper half space is set to $n_{film} = 1.5$, so in fact the seemingly equivalent values for scattering at an interface and within the film structure is actually due to the reduced backscatter due to interference in the film almost exactly cancelling out the reduced near field coupling due to the smaller RI gradient. The 4.5% difference in F_{subs} between the NC and the NH is probably due to the weak residual concentration of light about the upper NC face, which draws a fraction of the mode further away from the film than is possible with a hemisphere. This is supported by the work of Mokkapati et al which found that taller Ag cylinders above an Si substrate achieved significantly less coupling to the substrate as the particle height was increased,[206] although the difference in geometric cross-section could also be a factor here.

Of all three particles, the hemisphere couples light into the substrate the most effectively and has the weakest backscatter due to higher order modes thanks to its geometry only supporting a weak quadrupole. The spectral region covered is not so broad as for the other two particles, but for many antireflection applications this is not necessarily too much of a problem, in fact in some light trapping for PV applications this is a desirable attribute since there is a certain spectral region where absorption enhancement is needed the most, e.g. the weakly absorbing NIR region for silicon,[46] or the red absorption edge of P3HT:PCBM for organic cells.[52] However the location of the absorption peak beneath the primary mode could prove problematic.

6.1.3 Directional scattering for flat-sided particles

The directional scattering into the substrate from spheres, hemispheres and cubes is shown as Fourier space patterns and traces in Fig. 6.5. Simulation and experimental results using the microscope described in section 4.5.2 are compared for cubes and spheres as the two extreme examples. The first thing to note is that there is a marked increase in light scattered beyond θ_{crit} for flat particles, especially for cubes, as well

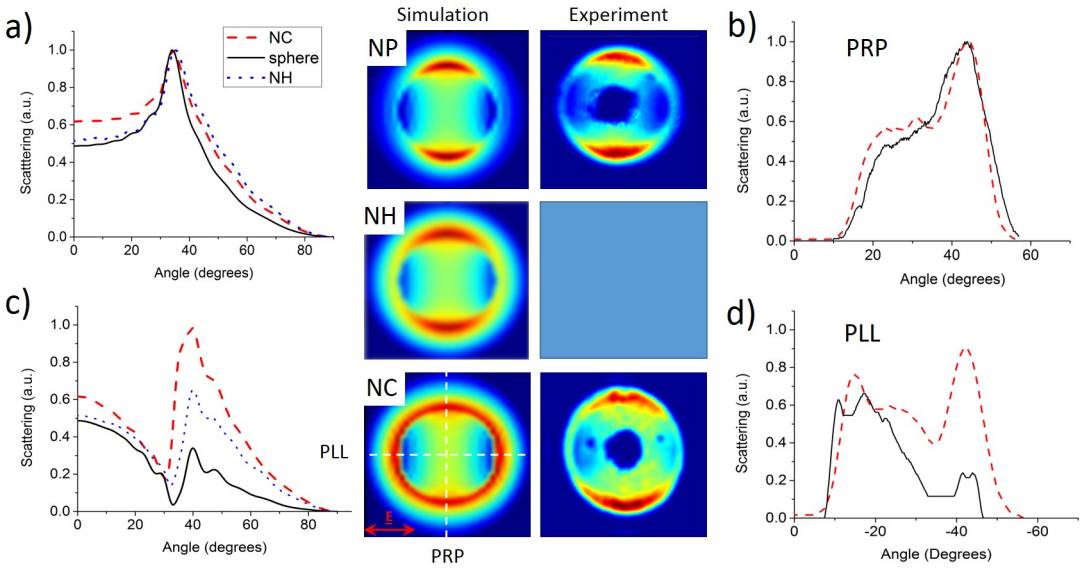

Figure 6.5: Simulated and experimental Fourier space plots of scattering into a glass substrate at 532 nm for 100 nm spheres, hemispheres and cubes, including traces taken PRP (a),(b) and PLL (c),(d) to the incident polarisation. Here, n_{subs}=1.52, n_{film}=1.31, & n_{air}=1.

as some increase in small angle emission. This is to be expected since the modes have been seen to be closer to the substrate which, considering the dipolar model of Neyts[129] discussed in section 3.1 will result in greater near field coupling and evanescent emission into the substrate. It was observed earlier that cubes exhibit slightly weaker forward coupling compared to hemispheres thanks to their greater height producing some electric field enhancement further from the surface, thus the apparent increase in large-angle evanescent coupling is somewhat surprising. However, the long edges and greater cross section of 100 nm cubes compared to 100 nm hemispheres result in a near-field penetration into the substrate across a greater surface area, which could explain the increased evanescent emission, although further research would be needed to confirm this.

The average path length enhancement in the substrate for a single pass compared to normally incident light is 38 %, 36 % and 26 % for hemispheres, cubes and spheres respectively. These values relate to the average percentage increase in distance travelled by light scattered from a particle, compared to the distance travelled by normally incident radiation traversing a substrate of arbitrary thickness, and is a good measure of how much light is scattered to large angles in the substrate. The experimental figures

for the cubes in Fig. 6.5 certainly show some of the traits seen in the simulations, such as increased low-angle scattering and much larger lobes in the PLL trace compared with the spheres, although the large angle emission cannot be measured in this setup due to the NA of the objective. However, this effect does seem somewhat less than the simulations predict: for example the lobes for the PLL trace are predicted to be ~60% stronger than the scattering power along the normal, but experimentally they are measured to be roughly equal (although this is slightly difficult to determine precisely due to the patch stop). This difference is probably due to the rounded corners of the NC's found in section 4.2.3 which are shown in section 7.5.2 to have a significant impact on coupling to substrates.

Examining the scattering patterns into the substrate for spheres and cubes in a film in Fig. 6.6, a similar effect can be seen, with increased scattering at low angles and beyond θ_{crit}, especially for emission PLL to the axis of polarisation. In this instance 44 % of the light scattered into the substrate by the cube and 39 % of that of the sphere is scattered at angles larger than the critcal angle, with total path length enhancements of 51 % and 40 % respectively. The low and high angle scatter from the cube counteract each other to an extent but the NC still performs better than the sphere, again demonstrating the benefit of using flat-sided particles for light trapping.

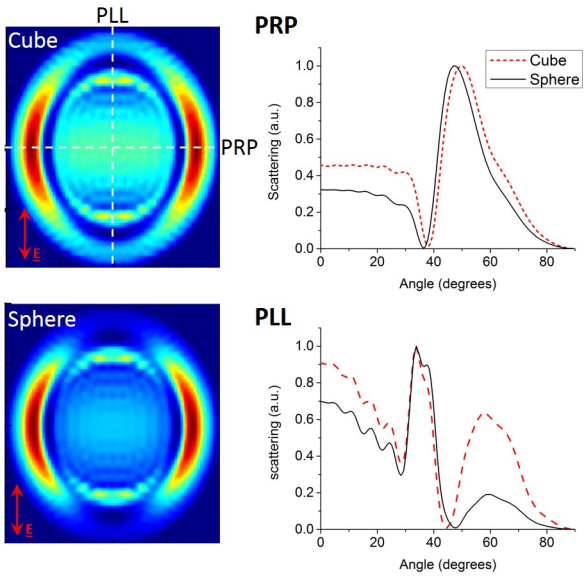

Figure 6.6: Simulated Fourier space plots of scattering into a glass substrate at the peak of mode I for 100 nm spheres and cubes, overcoated with a film with z_+=200 nm, including traces taken PRP and PLL to the incident polarisation. In these simulations, n_{subs}=1.8, n_{film}=1.5, & n_{air}=1.

The advantages of using flat sided particles for light trapping, as opposed to the spheres described in the last chapter are clear: better forward coupling, and increased wide angle scattering due to better evanescent coupling with the substrate. For the case of a bare interface, hemispheres demonstrate much better forward coupling across the

spectrum compared to spheres and cubes, albeit across a more limited spectral range, and only a slightly reduced path length enhancement compared to NC's. However the absorption peak having the same resonance as the maximum scattering could also prove problematic. When a film is added however, forward scattering from NC's is almost equivalent to hemispheres, with a slightly greater path length enhancement and a separation between the absorption and scattering peaks. The potential of cubes for light trapping enhancement seems to have been mostly overlooked in the literature to date, most likely due to the fact that previous studies have not taken thin film effects into account. Their ease of fabrication through wet synthesis and their properties discussed here suggests that NC's could make much more of a contribution to light trapping studies than has so far been the case.

6.2 Longer - Nanowires

For light trapping applications it is often enough to ensure that the most light is scattered to the largest possible angles, and knowledge of how the layer materials and geometries affect this is extremely useful. For antennae however, it is generally highly desirable to be able to emit or receive light in a defined angular range to maximise the signal collection efficiency from an emitter. There has been much interest in optical antennas, which has increased over the last 5 years as fabrication techniques have improved, and the small footprint,[82] strong field enhancement[116] and capacity for directionality[61] make LSP structures a promising option. The utilisation of readily fabricable structures that do not require complex synthesis procedures are of the greatest interest for this investigation, and so the zoo of varied antenna designs will not be discussed in detail save for a few examples. For further reading the review by Novotny & Van Hulst is recommended.[211]

One route to pursue unidirectionality of optical emission is to follow methods that have been shown to be effective for radio and microwave antennas and utilise modern techniques to scale them down. Investigations into nanoscale Yagi Uda antennas produced strong directionality of emission from a quantum dot coupled to the antenna in the

far field.[61–63] A similar arrangement also produced highly directional cathodoluminescence when irradiated with an electron beam.[212] These structures require either e-beam lithography or FIB milling to produce however, and thus present problems for future scalability. The nanocube patch antennas described in section 3.4 are also known to produce unidirectional emission, but over a considerably broader angular range.[84]

A possible solution to this is to use nanowires, which are attractive due to their ease of manufacture. Shegai et al demonstrated that by exciting surface plasmon waves from one end of the NW, highly unidirectional plasmon leakage radiation was produced from the opposite end.[134] The effectiveness of this as an antenna was then demonstrated by coupling emission from rare earth nanocrystals to the NW.[64, 65] An alternate approach was taken by Arnaud[79] and Zraggen,[135] where plasmons in the NW were excited via a photonic waveguide, producing well structured bi-directional emission and hinting at the possibility of integration with photonic circuity.

In this section the scattering of normally incident light from long (> 5 μm) NW's at a bare interface and in a thin film structure is investigated. The directionality of scattering from the NW's and how the film can be used to optimise this is discussed. This is mostly a fundamental work and does not discuss the coupling of NW's to any kind of single emitters, rather focusing on planar illumination, but the results could be utilised to improve the directionality of all the NW studies mentioned above.

It has been demonstrated that a nanowire can be modelled as a set of point dipoles arranged in a line across the length of the wire.[137] Due to the phase difference incurred by radiation from different points in the wire, the dipole radiation pattern is multiplied by a form factor, obtained by integrating over the wire length,[133] as shown in equation 3.8. This results in the predicted scattering pattern being that of a dipole, multiplied by a sinc^2 function perpendicular to the axis of the wire. The intensities along the sinc^2 strip depend on the orientation of the incident radiation with respect to the NW. The larger the wire aspect ratio the tighter the scattered light is confined about the axis perpendicular to the wire.

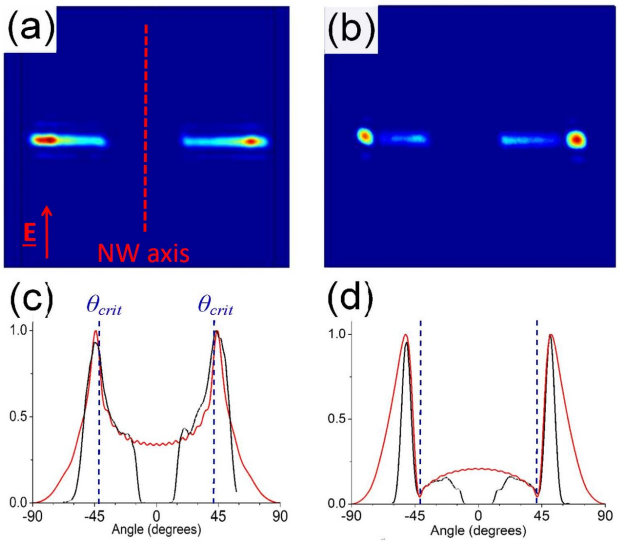

Figure 6.7: Experimental Fourier space images and line traces (black lines) of scattering from a 115nm diameter NW's on the surface of a glass coverslip with incident radiation polarised parallel to the wire axis. **a** and **c** show results for a wire on bare glass, **b** and **d** for a NW coated in 185 ± 5 nm PFTE AF. The line trace plots also show results from FDTD simulations (red lines). Here, n_{subs}=1.52, n_{film}=1.31, n_{air}=1 and incident illumination is at 532 nm.

Figure 6.7 shows the experimentally obtained scattering patterns from an Ag nanowire on a glass substrate, under 532 nm illumination polarised parallel to the wire axis. For NW's on a bare glass substrate the lobe peak is 2.9 times the value at zero degrees with 38% of the light scattered into the substrate being caught within 10 degrees of the lobe peaks, which is a significant increase compared to 3% for a spherical NP at a bare interface.

The ability of a thin film to increase the directionality of the NW scattering is highlighted in Fig. 6.7(b), which shows the Fourier space images of a NW on a glass coverslip overcoated with 185 ± 5 nm of PTFE AF 1600. Again a good agreement with simulations is shown through the line traces and the lobe strength here is 5 times that of the central peak. Thanks to this reduction in low-angle scattering, 43% of the light is scattered within 10 degrees of the lobe maxima - a 15% increase from the uncoated NW.

Figure 6.8 shows the Fourier space scattering patterns for NW's with incident illumination polarised perpendicular to the NW axis. The experimental and simualtion results mostly show good agreement; in Fig. 6.8(c) a slight asymmetry is observable,

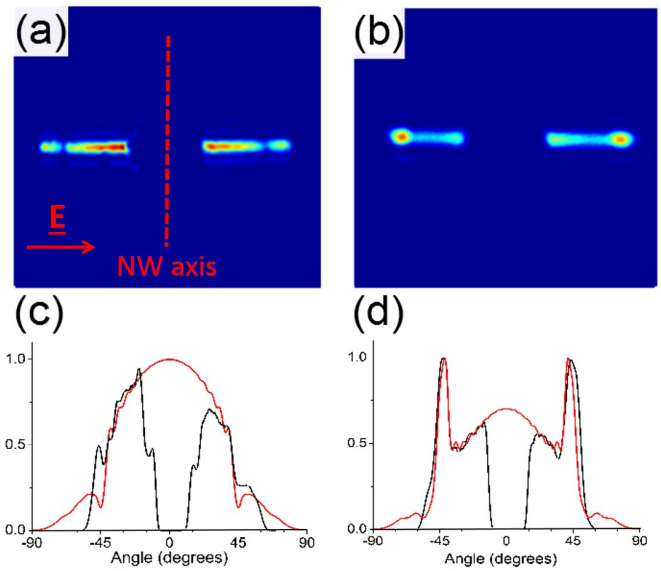

Figure 6.8: Experimental Fourier space images and line traces (black lines) of scattering from 115 nm diameter NW's on the surface of a glass coverslip with incident radiation polarised perpendicular to the wire axis. (a) and (c) show results for a wire on bare glass, (b) and (d) for a NW overcoated in 185 ± 5 nm PFTE AF. The line trace plots also show results from FDTD simulations (red lines). Here, n_{subs}=1.52, n_{film}=1.31, n_{air}=1 and incident illumination is at 532 nm.

as well as some disagreement in the intensity of the side lobes that is most likely due to the area of the glass substrate containing the NW not being exactly square with the objective. The presence of some organic precursor around the NW, might also cause slight discrepancies by altering the dielectric surroundings of the NW, although this was not observed to be an issue in the SEM and care was taken to only select NW's that appeared clean and regular in the image plane CCD. It can be seen that there is a much weaker confinement within the lobes produced than for the PLL polarisation, and that the lobes in the PRP orientation are at smaller angles and have much less efficient evanescent coupling to angles beyond θ_{crit}. For this reason it shall be the PLL polarisation which is focussed upon for the remainder of this chapter.

A trace of the scattering intensity parrallel to the axis of the wire (in the farfield) should produce a sinc^2 pattern, which can be fitted to experimental results to determine the length of the wire. This is shown in Fig. 6.9, where Eq. 3.8 has been fitted to the experimental trace using the Ezyfit toolbox for MatLab[213] and shows good agreement with experiment for a NW of 6.9 μm length.

The inset to Fig. 6.9 shows a webcam image of the NW, which, when magnifications from the microscope components are taken into account gives a wire length of 6.5± 0.4 μm, where the uncertainty is due to the spherical aberrations in the image, which is in agreement with the model. This process was repeated for a variety of other NW's, and in every case a good agreement was found within the bounds of error. The discrete dipole model proposed is therefore seen to be sufficiently accurate for the purposes of this research and is a convenient way to understand the scattering traces seen in figures 6.7 and 6.8.

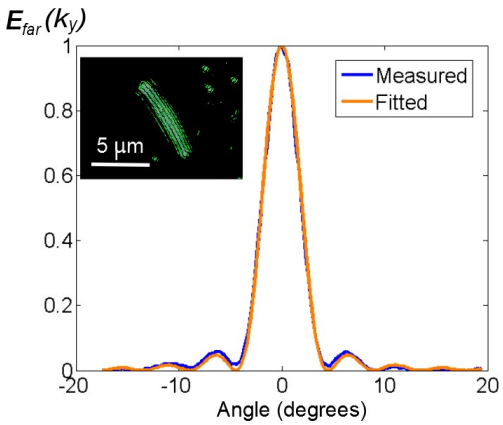

Figure 6.9: Traces taken across the Fourier patterns from NW's shown in Fig. 6.7 parrallel to the axis of the wire (perpendicular to the line in Fourier space). Experimental results (blue) are fitted to a sinc^2 function (orange) to find the length of the wire. This can be compared with values observed on the webcam (inset) to test the theory.

6.3 Tuning the confinement of scattered light

In the previous chapter, changing the film thickness above a particle was shown to directly affect how much light is emitted into a given angular range: the evolution of the scattering patterns of spherical NP's with increasing z_+ is displayed in Figs. 5.11 & 5.10. This is of great potential interest for nanoantennae where the confinement of light in high-angle scattering lobes allows for very directional emission. For light trapping applications, this behaviour affects the path length in the substrate and the amount of light scattered beyond the critical angle, θ_{crit}, both of which can be maximised by careful choice of z_+. These two properties are examined in Fig. 6.10.

6.3.1 Emission to a small angular range

As discussed in the previous section, nanowires are far more effective than any other particle studied at scattering light to a small angular range and as Figs. 6.7 and 6.8

show, this is most effective when incident radiation is polarised PLL to the length of the wire. Thus in Fig. 6.10(a) only values from NW's in PLL configuration are considered.

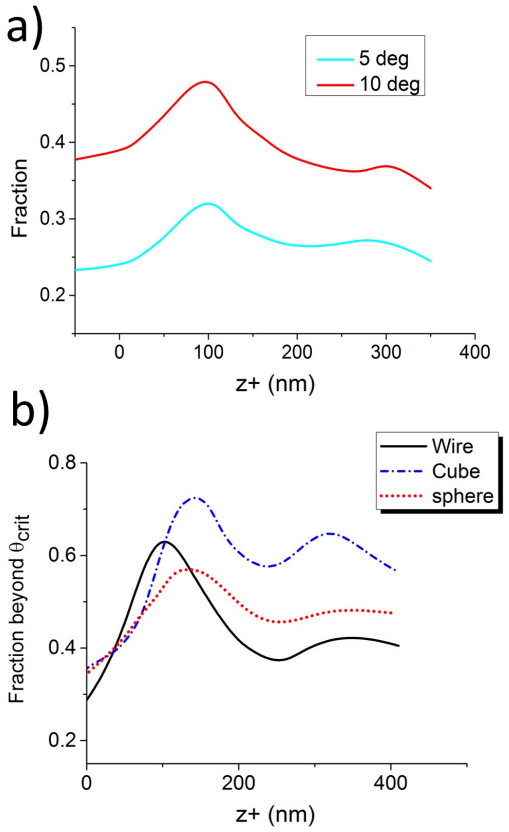

Figure 6.10: (a) Total fraction of light scattered within 5 (cyan) and 10 (red) degrees of the angular lobes for a 100 nm x 10 μm NW in varying thicknesses of film where n_{subs}=1.8, n_{film}=1.5, & n_{air}=1. (b) Fraction of light scattered into the substrate beyond the critical angle by 100 nm spheres, cubes and wires on a substrate for varying z_+ under 532 nm illumination.

It is clear that the confinement can be maximised for a 100 nm thick, 10 μm long NW resting on the substrate at z_+ = 95 nm where an angular range of 5 degrees about the centre of the lobes at 46^o contains 32 % of the scattered light, and an angular range of 10 degrees 48 %. This value is limited by the large evanescent contribution due to the proximity with the substrate which broadens the lobes through increased emission beyond θ_{crit}. By moving the NW away from the substrate, the emission pattern becomes much tighter as demonstrated in Fig. 5.12 and for the same z+ value, with z- = 100 nm, where the near-field is completely decoupled from the substrate, a confinement of 38 % in the 5 degree range and 55% for 10 degrees can be achieved, which is an enhancement of 19 % and 15 % from the case of a NW resting upon the substrate. There is some reduction in F_{subs} here due to reduced near-field coupling, which has been accounted for in these values, but the overall increase in confinement shows that the interference effects from the film-air interface is the dominant factor here. This result must be halved for coupling to any single direction, but even so this compares well to previous results using NW's and other shapes.

The best results for direction emission from particle-based nanoantennas in the liter-

ature is by Shegai et al[134] via excitation of travelling plasmons at one end of a NW producing leakage radiation at the far end, with a coupling to the substrate of 11 dB, corresponding to an F_{subs} of 0.93 and an angular FWHM of the lobes of 4^o by 30^o. Results fabricating Yagi-Uda antennas produced visibly less effective confinement and require a more involved synthesis.[61, 212, 214] The best results from this investigation produce $F_{subs} = 0.86$ at 532 nm, and the FWHM of a single lobe is 4^o by 11^o, so whilst being in no way unidirectional, for an application requiring emission over a very narrow angular cone of a few degrees or so, the scattering from an NW in a thin film illuminated by planar radiation here compares well to the leakage radiation to travelling plasmons in an NW.

These results could also be used to improve the directionality of existing nanoantenna designs: Hartmann et al coupled single emitter crystals to NW's via a near field interaction and found that the far-field emission was a convolution of the dipolar pattern of the nanocrystal emitter and the leakage radiation of the NW,[65] so utilising the thin film to tune the dipolar pattern could enhance the confinement of this system as well. Arnaud et al. excited the plasmon modes of a gold NW laid across a linear waveguide via the photonic modes of the waveguide,[79] in order to connect the guided modes with a far-field propagating signal. Using this research, the radiation pattern produced could be tuned using an overlaying thin film to give a much more directional emission from the waveguide coupled system, although the film materials would have to be chosen carefully to not interfere with the waveguide properties.

6.3.2 Emission beyond the critical angle

One of the most obvious applications for this research is the improvement of light-trapping via plasmonic scattering, both for the enhancement of solar cells and for coupling light into and out of other planar waveguide structures. As it has been shown that particles with different geometries couple differently to the substrate due to their near-field interactions, it makes sense to examine how much light can be scattered beyond the critical angle and trapped within the structure by different NP's. In Fig. 6.10(b)

the fraction of light scattered into the substrate beyond θ_{crit} as a function of the film height above the particle centre is shown for 100 nm cubes, spheres and 10μm long wires resting on the substrate. As this is a fractional value, it is normalised to the driving force. All traces show a strong peak around 100-150 nm which is due to the interference between directly emitted light and that scattered form the interfaces as discussed in section 3.3. As the refractive indices fulfil $n_{air} < n_{film} < n_{subs}$ the interference is determined chiefly by reflection from the film-air interface as described in section 3.1. So as the film height above the particle, z_+ increases, the interference maxima shift to larger angles up to the critical angle for a $n_{subs} - n_{film}$ interface and increasing number of new maxima begin to form closer to the normal. When z_+ becomes comparable to the wavelength, thin-film interference effects become negligible and we return to the pattern of a particle at a bare interface, as illustrated in Fig. 5.10. So the most concentrated angular scattering will be for fairly thin films where only one set of lobes is present, and further maxima will lead to less significant alterations, which is what is observed.

Cubes are shown to have by far the strongest emission fraction beyond θ_{crit} for most thicknesses, peaking at 0.73 for $z_+ = 137$ nm, which is expected as it was demonstrated earlier in Fig. 6.5 that they achieve the best large angle coupling of all the shapes considered due to confinement of the primary mode at the substrate face. Wires show the sharpest initial peak, at 0.63 for $z_+ = 102$ nm, due to the farfield scattering of NW's being a convolution of the dipolar pattern and a sinc^2 function, as discussed in section 3.2. This means the large low angle component emitted by dipoles PLL to their axis which is much less sensitive to z_+ is not present for NW's. After this initial peak however, the formation of multiple lobes with increasing z_+ leads to greater scattering at small angles, especially along the PRP axis of dipolar emission, leading to *reduced* large angle scatter for NW's at larger z_+ values.

This information is useful for tuning the scattering from differently shaped particles to maximise confinement and light trapping. Tuning the particle position and the thickness of the film can strongly effect the fraction emitted close to the angular lobes and the fraction scattered beyond the critical angle. It is worth noting that many of

these effects could also be achieved by altering the refractive index of the film, but as there is generally a limited range of materials that can be utilised in a given application, and so varying the geometry seems like a more useful approach. NW's produce by far the most directional emission due to the interference of scattered light long their length, and cubes scatter the best to large angles. The next section investigates utilising this behaviour to create a novel sensor design.

6.4 A discussion on utilising confinement control to create a humidity sensor.

The previous section has demonstrated that altering the film thickness above a metal nanoparticle or nanowire changes the fraction of light scattered into a given angular range due to changing the interference conditions in the film. This variation in trapped light with film thickness presents an opportunity to produce a novel type of sensor if the film can be made from a material that alters its thickness in response to a change in the surrounding environment. The Nafion polymer from Dupont introduced in section 4.3.3 is a good example of such a polymer as it expands and contracts significantly with the surrounding relative humidity (RH).

As the NW showed the most significant peak in Fig. 6.10, making for the largest variation in light scattered beyond θ_{crit} over the greatest range of thicknesses, this is selected as the particle of choice for these tests. NW's also scatter much more brightly than cubes or spheres and are thus less affected by noise due to background scatter from impurities and inhomogenities in the sample, and so this setup is also advantageous experimentally.

NW's on a glass coverslip were overcoated with a thin Nafion film and placed in an environmental control chamber, illuminated by 532 nm light polarised PLL to the axis of the wire, and their angular scattering observed in k-space using the home-built microscope described in section 4.5.2. Figure 6.11 shows initial results demonstrating how the scattering pattern of the NW's beneath a 192 $\pm$ 5 nm (ambient thickness)

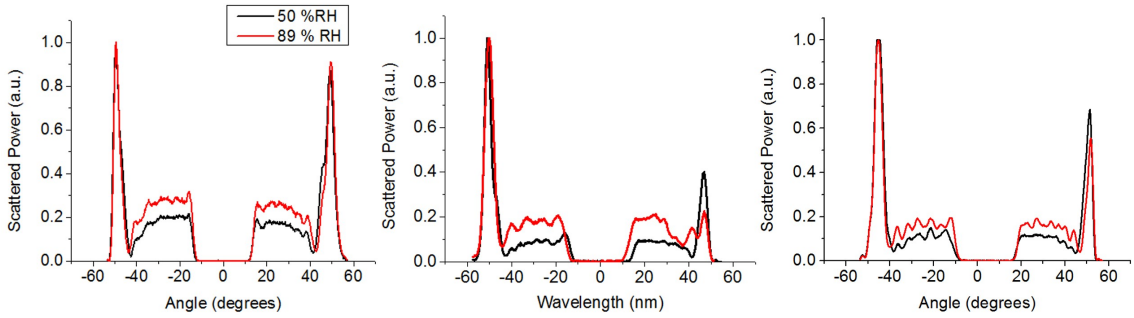

Figure 6.11: Normalised scattering pattern traces of three NW's in a 192 ± 5 nm thick Nafion film under 532 nm radiation polarized PLL to the axis of the wire as the relative humidity is altered.

Nafion film develops as the RH is increased from ambient levels at 50 %RH to 89 %RH - the upper limit of the apparatus. It can be seen that a significant alteration in the scattering pattern is achieved, and averaging over 16 NW's, this was found to match a film expansion from 192 to 220 ± 5 nm as simulated using FDTD. The 15 ± 3% expansion is in agreement with the values for Nafion RH response of equivalent thickness films obtained using ellipsometry which is discussed in section 7.2.

This result demonstrates that changes in humidity can be readily detected by examining changes in the scattering patterns from NW's under a moisture sensitive film. The last section investigated how altering z_+ affected the $fraction$ of the total scattered power in a given angular range as defined by an angle, θ. However, as shown in Fig. 5.9, due to the changes in the driving field, the *total* scattered power will also vary with z_+. To utilise this system as a sensor, it is important to consider how the *total power scattered into a given angular range* might change with RH, as this is the key value for determining the sensitivity of this system.

The actual power scattered within a given angular range, $P(\theta)$ is determined by two factors, as in equation 6.1:

$$P(\theta) \sim |E_d|^2 . I_{scat}(\theta) \tag{6.1}$$

a driving term due to the electric field intensity at the centre of the NW, $|E_d|^2$ as

discussed in section 3.2, and an interference term, $I_{scat}(\theta)$ dictating the fraction of power scattered (independent of source power) into a given angular range, taking into account both interference in the film and from components along the length of the wire. Here the light scattered at an angle *smaller* than the glass-air critical angle θ_{crit} is simulated, as this is the light which would escape a planar glass substrate after scattering by the NW and would be the most straightforward value to measure experimentally with the microscopes used in this investigation.

The relationship between the terms for a changing thickness of film above the wire, z^+ is shown in Fig. 6.12 for $\theta < \theta_{crit}$. Here the normalised electric field intensity is taken from transfer matrix simulations discussed in section 5.3.3, the interference values and the normalised power transmitted to the forward direction determined from FDTD simulations. 532 nm light is normally incident from the glass side, as this better approximates experimental conditions. Whilst the driving field has a sinusoidal dependency on the thickness, the relationship for the interference of scattered light is more complicated, as discussed in the previous section and in section 3.1.1, and so there are z_+ values where the two terms are in phase and where they are not. The most significant thickness range is for low z_+ values where there is only one set of lobes and therefore greater variation in the angular scattering.

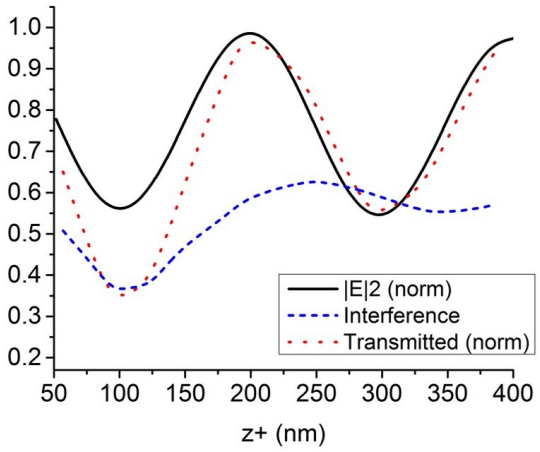

Figure 6.12: Simulated values of the electric field at the NW centre, fractional scattered power and actual (normalised) scattered power for a 100 nm NW in a Nafion film on a glass substrate as the height of the film above the particle centre is altered. In these simulations n_{subs}=1.52, n_{film}=1.35, n_{air}=1 and the incident radiation has a wavelegnth of 532 nm.

In Fig 6.12, the I and E terms are never exactly in phase, but importantly, around the first minimum they are close, and so the final transmitted power through the substrate has a greater variance than that produced by either component individually. For greater thicknesses, there is smaller variation in the interference term due to the formation of secondary lobes and so the transmitted power depends principally upon the driving

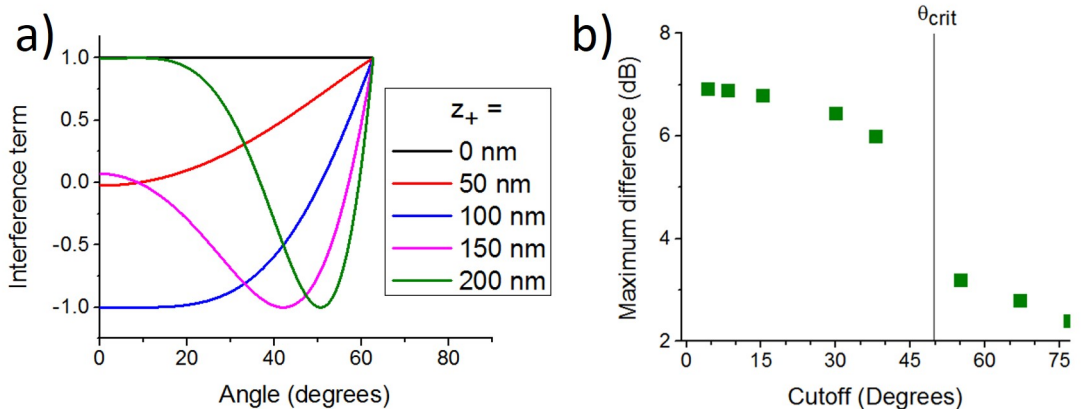

Figure 6.13: (a) Showing the z_+ - dependent part of the interference term for dipolar emitters in thin films from equation 3.5 as a function of emission angle in the substrate. (b) FDTD Simulated values of the maximum peak-to-trough variation (in dB) of total scattered power of a 100 nm x 10 μm NW under changing spacer for a variety of angular ranges defined by the cutoff angle. In these simulations n_{subs}=1.52, n_{film}=1.35, n_{air}=1 and the incident radiation has a wavelegnth of 532 nm.

field.

Reports investigating a Fabry-Perot (FP) sensor, where Nafion is coated onto the end of an optical fiber and the expansion of the film determines the reflection conditions at the fiber end, achieved a peak to trough variation of 7 dB.[215] The NW structure achieves a maximum of 4.6 dB, which is significantly inferior. By moving the NW away from the substrate (increasing z_-), the emission pattern becomes much tighter and depends more heavily on low angle emission as the evanescent component (which is not dependent on z_+) is decoupled. For the same setup, with z- = 100 nm, total peak to trough variance of 6 dB is predicted, which is a significant improvement but still does not match the FP setup.

This difference is due to the interference terms governing the scattering patterns, as discussed in section 3.3. Fig. 6.13(a), shows the the z_+ dependent part of the interference term in equation 3.5, which dictates the far field scattering pattern in the substrate. It is observed that this term is affected much more strongly by z_+ at low angles close to the normal than for large angles. Therefore the effect that z_+ has on the total power scattered, depends strongly on the angular region considered. This is demonstrated further in Fig. 6.13(b), which shows the maximum peak-trough variation in the total power scattered into a given angular range. It can be seen that where the angular cutoff

is high enough to include the lobes, the variation is weak, but for angles slightly below θ_{crit} the lobes are no longer considered and lower angles can be seen to vary much more significantly, approaching the sensitivity of a FP sensor as the cutoff approaches zero.

It should be noted that these values are the maximum power scattered into an angular range compared with the minimum. As can be seen in Fig. 6.12 a variation in thickness from ∼100 nm to ∼200 nm would be required to span this range. As Nafion films around these thicknesses have been observed in Fig. 6.11 and later in section 7.2 to expand by only about ∼15 % of thei original thickness, it is clear that this change in signal will not be achieved using the current setup.

This system therefore has few advantages compared with an FP reflection sensor: even though some particle dimensions are sub-wavelength, the area needed for the reflections to create the interference conditions which produce the angular scattering patterns is certainly not. The reaction time would be expected to be equivalent as in each case it depends upon the expansion of a thin Nafion layer. There may be some applications where scattering *beyond* θ_{crit} is desirable, e.g. planar solar concentrator windows, where the ability to incorporate RH sensitivity might be of some use, but this would also not produce superior sensitivites to an FP sensor and the result could be achieved more effectively by other means.

One application that might hold more interest would be to position a Nafion coated NW above a photonic waveguide, as in the work of Arnaud et al.[79] In this situation the NW modes would be excited by the waveguide, and therefore the ability of the waveguide to couple to the farfield would be dependent on the surrounding humidity. This could have applications for for optical circuity, and might be an interesting path for future study.

6.5 Conclusions

In this chapter the effect of particle shape on the behaviour of metal NP's in a thin-film structure was investigated. Cubes, hemispheres and wires were chosen for their ease of fabrication. The impact of the thin film on mode hybridisation of flat faced particles was found to be significant. For cubes the localisation of hybridised modes on the upper and lower faces was much reduced in a film due to the reduction in the RI gradient at the interface, resulting in weaker coupling to the substrate. However, despite the reduced near field coupling, the interference of scattered light by the film resulted in better forward scattering across the solar spectrum for cubes and prevented significant losses in F_{subs} for hemispheres.

The film also allowed the tuning of modes on the upper and lower faces of NC's with a degree of independence which could be useful in tuning the highly absorbing upper mode away from areas of interest for light trapping etc. This was not possible with NH's, as they do not support a strong upper mode. It was suggested that if thin film effects are taken into account nanocubes could make a much greater contribution to plasmonic light trapping studies than they have to date, and as they can be wet synthesised and easily processed they could prove an attractive alternative to the more ubiquitous hemispheres.

Nanowires were used to scatter light into highly confined lobes due to interference from emission along their length. The confinement of scattered light to within a small angular range about the lobes was tunable through altering the film thickness and if considering an angular cone of a few degrees was shown to produce a comparable level of confinement to leakage radiation from NW SPP's and optical Yagi-Uda antennas, despite not being unidirectional. The effect of the thin film could also be utilised to improve directional emission from the NW SPP antennas discussed in the literature.

The height of the film above spheres, cubes and wires was altered in order to tune the amount of light scattered beyond the critical angle of the structure. It was found again that cubes scattered the best to large angles, but NW's had the strongest variation.

Therefore a novel humidity sensor design was proposed where a NW was overcoated with a Nafion film which expands with RH and alters the fraction of light scattered into a given angular range. Preliminary experiments observing the change in NW scattering in Fourier space confirmed the viability of this approach. It was found that the insensitivity of the scattering at large angles to the height of the film above the particle meant that this design could not beat a Fabry-Perot setup, and could only reach equivalent sensitivities if solely emission very close to the normal is considered. In practice this will not be achieved with Nafion as it does not expand sufficiently to encompass the maximum and minimum interference conditions. There could be some other ways to utilise this approach, such as measuring the coupling of light into the guided modes of the planar structure, or the ability to excite the NW sensor via a photonic waveguide, which would be interesting avenues for future research.

In the next chapter, a different sensing geometry based around nanocubes separated from a silver sheet by a Nafion spacer is investigated and methods to optimise and utilise this sensor discussed.

Chapter 7

Subwavelength sensing elements from film-coupled silver nanocubes

This chapter is based around the paper 'Plasmonic Gas Sensing Using Nanocube Patch Antennas',[216] by Powell et al, but also contains additional material.

The previous chapters have shown that metal nanoparticles in a purely dielectric environment provide a rich parameter space to be explored and exploited. Another system that is attracting a large amount of interest is that of a metal particle separated from a metal sheet by a thin spacer, as shown in Fig. 7.1(a). When the particle is illuminated, the electric field of incident light induces the motion of free charges, which are reflected at the edges of the particle leading to the formation of resonant modes. For a flat particle the charge separation induced by the incident electric field is mirrored in the sheet, producing a coupled plasmon mode with a resonance strongly dependent on the spacer thickness, as discussed in section 3.4.

If a spacer material that expands in response to an external stimulus is chosen, this

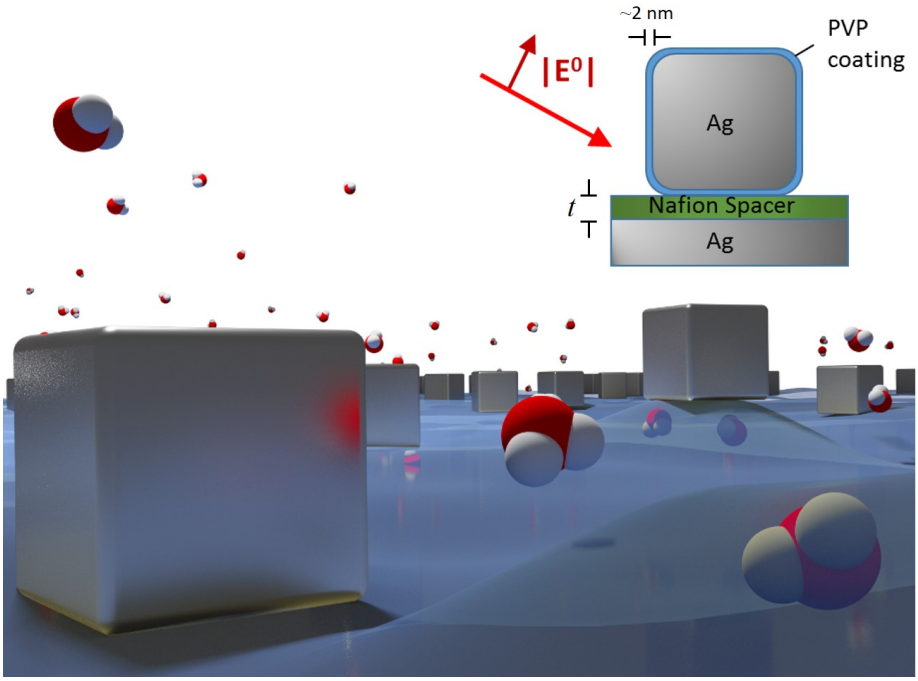

Figure 7.1: Artistic representation of the nanocubes resting on a Nafion film which expands on interaction with water molecules. Inset: The basic setup for simulations and experiments in this chapter: a silver NC with a PVP coating is separated from a silver film by a dielectric spacer layer. It is illuminated and the scattered light is used to characterise the system.

system provides the basis for an optical sensor with a footprint hardly greater than the cross-section of the particle, which can be fabricated using established planar deposition techniques. There is much motivation for utilising plasmonic particles as sensing elements, especially those producible entirely through wet-synthesis techniques, due to their ease of manufacture, efficient operation beneath the diffraction limit, strong electric field enhancements and their capacity to be coupled to photonic circuitry.

In this chapter, the operation of the nanocube patch antenna as a gas sensor is demonstrated. As a proof of concept the Nafion fluoropolymer from Dupont, which expands in response to changing relative humidity (RH) was used as the spacer layer to create a humidity sensor. A brief review of particle-based plasmonic gas sensors and the state of humidity sensing in general is presented to put the work in context. The properties of very thin films of Nafion and their response to changing RH are then discussed. The tunability of the principal waveguide mode through altering spacer thickness is shown and the utility of this system as a humidity sensor, both through wavelength-shifts and through intensity variation of scattering by a red laser is demonstrated. Finally the

road to enhancing the sensitivity is also explored using Finite-difference time-domain (FDTD) simulations and the potential for detection of a slew of other gases, along with integration with plasmonic waveguides is discussed.

7.1 Progress in plasmonic gas sensing

Optical sensors present an attractive alternative to well established electrochemical technologies owing to their fast response times,[81, 217] low susceptibility to external EM radiation, potential for increased sensitivity[77, 77, 218] and plentiful choices for signal retrieval such as intensity, spectrum, phase and polarization.

Due to their ability to confine light to subwavelength volumes, leading to extreme sensitivity to their dielectric surroundings, surface plasmons are an ideal platform for optical sensing and are even beginning to enter the commercial market.[68, 69] The ability of many plasmonic structures to behave as nanoantennas, coupling near field enhancements to well-directed far field emission means that well-designed plasmonic sensors also have potential for integration with on-chip photonic or plasmonic circuitry.[31, 219] Aside from Surface enhanced Raman scattering, these sensing applications are by far the most successful outcome of the plasmonics revolution to date, owing to the fact that the performance of sensors is not significantly damaged by the strong absorption of plasmons in noble metals, which has so far prevented plasmonic circuitry and photovoltaic enhancement from making any commercial impact.[220]

Most plasmon sensing relies on detecting a change in refractive index, and for this reason the majority of sensors are designed to operate in fluidic environments, where there is much more contact with molecules in the surrounding environment and the adsorption of biological molecules, or changes due to chemical reactions of the addition of impurities can be detected relatively quickly and easily. This report focusses on plasmonic gas sensing, but there are several detailed reviews discussing plasmonic sensors in aqueous environments, generally to be utilised in biological or medical applications. The reader is referred to the work of Anker[11] and Chung.[29]

The first plasmonic gas sensors were produced in the early 80's by Nylander and Liedberg who used a prism to excite surface plasmon polaritons on a silver sheet coated with silicone oil[221] (See Fig. 7.2(a)). When placed in a gas chamber and exposed to the anaesthetic gas halothene, the refractive index of the oil was raised, which altered the characteristic angular reflection minimum due to the SPP, which achieved sensitivities of 100's of ppm. This method was then expanded to investigate the adsorption of antibodies in an aqueous environment,[12] and so was the precursor of almost all plasmon sensing techniques.

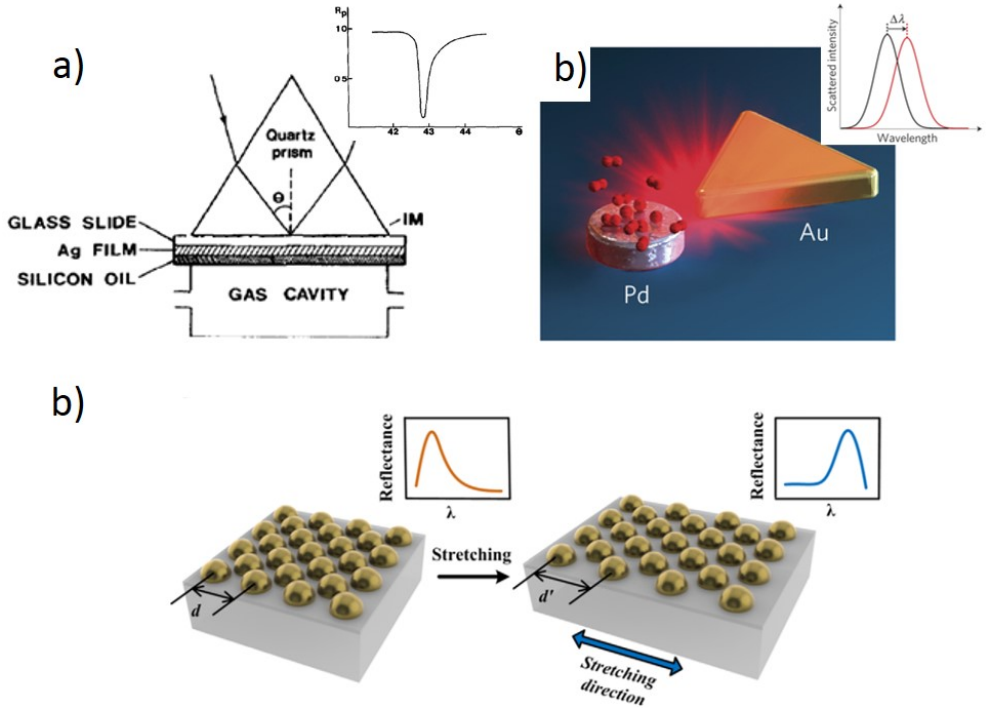

Figure 7.2: (a) Adapted from Liedberg et al:[12] SPP's are excited on a Ag film coated in silicone oil. Gas is absorbed by the oil, changing its RI and altering the angular reflection minimum (inset). (b) Adapted from Liu et al:[77] Hydrogen sensing using a resonant antenna-enhanced scheme. A palladium nanoparticle is placed at the nanofocus of a gold antenna, Hydrogen absorption on the palladium particle changes its dielectric function, which causes a resonance shift of the gold antenna that can be optically detected. (c) Adapted from Zhao et al:[222] Illustrating how stretching a film embedded with NP's shifts the resonance.

Gas sensing not relying on a reactive coating, and therefore only measuring the change in plasmon resonance induced by RI changes in the environment was first achieved by Vukusic and Jory using the polarisation conversion properties of SPP's excited in Silver gratings.[223, 224] However this required large amounts of the solvents measured to induce significant adsorption on the metal and create a dielectric shift, resulting in

severely limited sensitivities. With the improvement of production and analysis techniques required to produce well-characterised samples, interest in sensing using colloidal nanoparticles increased due to their ease of production and compact size, making them much more sensitive to small changes in the local environment than SPP or photonic sensors.[14] Bingham et al fabricated Ag nanoparticle arrays using nanosphere lithography and used a high-resolution spectroscopy technique to measure the plasmon shift of the arrays between Nitrogen, Argon, Helium and wet air environments, caused by RI shifts of the order 10^{-4}, achieving an extremely high spectral resolution.[30] However, it was not possible to distinguish between gases using this technique and the miniscule changes in RI that trace elements of a gas will produce limits practical application.

A significant step forward in plasmonic gas sensing has been is the use of 'active' plasmonic structures where the surface plasmon extends into, or is excited within a gain medium resulting in increased radiating power and vastly narrowed linewidths.[225–227] This effect was demonstrated recently by Ma et al to achieve parts-per-billion sensitivity to nitroaromatic compounds used in explosive devices, using a lasing plasmonic cavity with a CdS slab above an Ag sheet separated by a thin layer of MgF_2. CdS is both the gain and the sensing material. Molecules adsorbing onto the CdS change the surface chemistry and reduce recombination losses at the surface, resulting in measurable laser intensity shifts. However, although this is an impressive result with much potential for future development, the response time to detect the concentrations found in real-world applications was several tens of minutes, which would hinder its utility in the field.

The vast majority of plasmon gas sensors utilise some form of active layer which responds to a specific chemical change in the environment. This does mean that the sensor is limited to an extent by the material properties of the active layer, but it also means that with careful material choices, layers can be selected which only respond to a single reagent. This can take the form of a refractive index change,[77, 81, 228–231] or a structural reorganisation.[70–76] Tokareva et al used poly(2-vinylpyridine) brushes to separate a nanoisland Au film from a layer of spherical Au NP's.[70] The brushes

coiled and uncoiled in response to pH, thus changing the separation of NP layers and altering the resonance. Later, noble metals were mixed in with precursor solutions and NP-embedded films produced which expanded and contracted in response in the presence of an analyte, thus altering the resonance of the film (Fig. 7.2(c)). This technique has been used to detect organic solvents such as chloroform and toluene,[72] pH[74] and relative humidity,[71, 75, 76] which is a good system to test a sensor due to experimental ease and the ready availability of materials which respond to water vapour.

There are some significant benefits to using single-particle systems rather than extended films - such as much greater sensitivity to changes in a tiny mode volume, allowing for the detection of individual processes, which is important for applications such as catalysis.[77] Liu et al used e-beam lithography to create Au triangles near a Palladium nanocrystal, which can absorb hydrogen within its crystal lattice to produce palladium hydride in a reversible manner (Fig. 7.2(b)). This was able to detect hydrogen concentrations well below the dangerous 4 % threshold where explosive combustion is a hazard and provide insight to the catalytic processes in the Palladium.

There has also been some recent interest in systems which can be integrated with waveguide structures, which would enable future implementation. Wang et al embedded gold nanorods within a RH-sensitive Polyacrylamide (PAM) fibre and observed the effect of RH on the RI of the wire and thus the attenuation of light transmitted through the fibre with good results.[81] Gu et al positioned a 192 nm diameter Ag NW above a PAM film and aligned tapered fibre tips to excite and measure SPP's along its length. The transmission was seen to alter significantly with RH.[231]

All of the single NP techniques described so far require strenuous manufacturing techniques which hinders their real world utility. A single particle sensor, which is simple to fabricate and could be integrated into photonic circuitry is still lacking.

7.2 Ellipsometry studies of very thin Nafion films

Nafion is a Poly(perfluorosulfonic acid)-based long-chain polymer with a structure that causes it to take on water from its surroundings and expand significantly under high humidities.[178–180] The structure and general expansive behaviour of Nafion films with increasing moisture content was discussed earlier in section 4.3.3. However, films of less than ∼50nm are a special case, and many studies have shown that the structure and behaviour of such films is highly dependent on their thickness.[178–182, 232] As the gap thickness is the key parameter in this study, the effect this has on the properties of the spacer is of vital importance.

There is something of a discrepancy in the literature regarding the structure of very thin films. Using neutron reflectometry, Dura et al[179] and then others,[178, 232] observed extremely water-rich and poor layered lamellar regions in the first ∼5-7 nm of a Nafion film at a SiO_2 on Si surface, demonstrating a strong phase segregation for ∼100 nm films and extremely thin (< 10 nm) films. There were no lamellae seen on the more hydrophobic Au or Pt substrates, which instead showed just one water rich layer near the substrates. This result indicates that the structure of the Nafion is retained for very thin films but is extremely sensitive to substrate conditions.

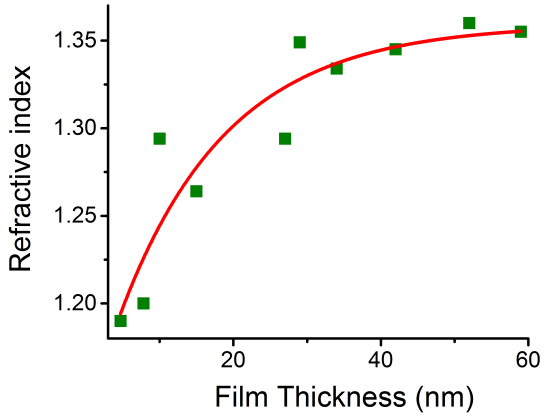

Figure 7.3: The refractive index of thin Nafion films used in this investigation under ambient conditions as measured by ellipsometry.

However Modestino et al.[181] and Petrina[182] used TEM and grazing-incidence small-angle x-ray scattering to find a marked *decrease* in phase-segregation with decreasing film thickness below ∼20 nm, across several different substrates, using both spin-coated and self-assembled films. This somewhat contradicts the findings of Dura et al. and throws the existence of extended structures within very thin Nafion films into question. Most studies observing lamellar structures studied much thicker films, and a direct study of the structure of sub-20 nm

films is still lacking. Ogata et al,[180] observed lamellar structures in ∼50 nm films on SiO_2 and not on Ag, but found the water uptake and expansion properties to be highly similar.

Thus there is something of a disagreement in the literature as to the nature of the film structure for films below ∼20 nm, although all studies seem to agree that the choice of substrate does not strongly affect the expansion behaviour of these films as humidity is varied. The results of this study agree very closely with that of Modestino et al and so the model of the increased expansion due to lack of morphological restrictions for very thin films seems an appropriate picture here and shall be used to interpret the following results.

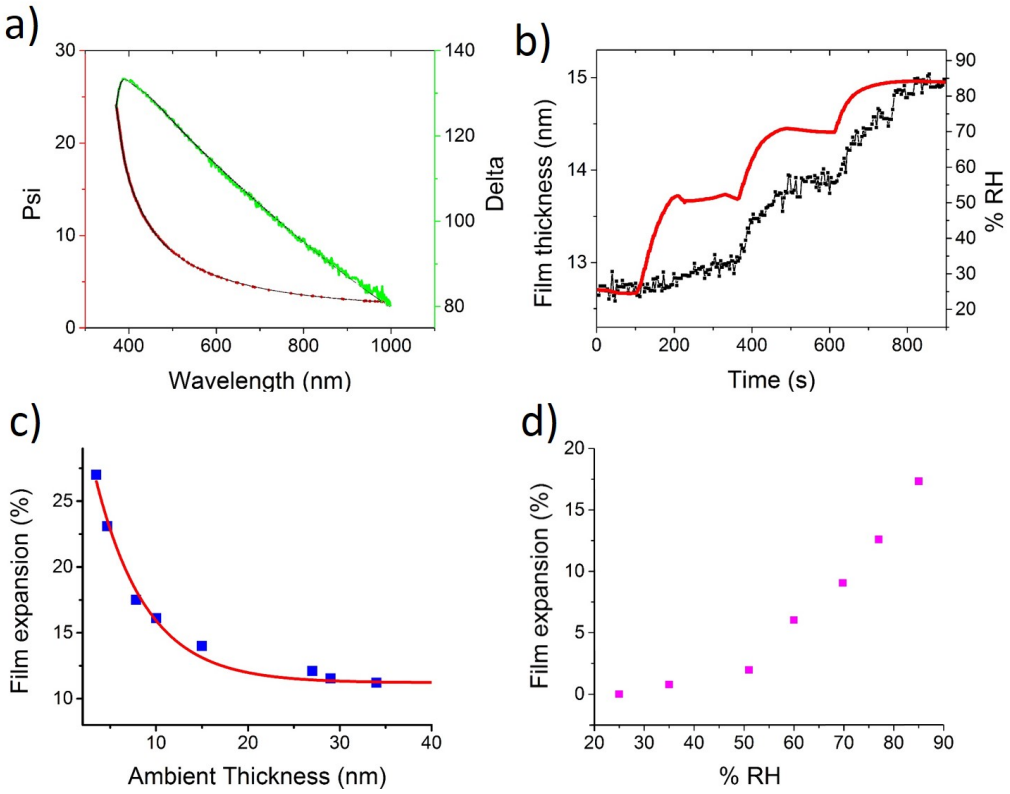

Figure 7.4: (a) Raw ellipsometery data for a 15 nm Nafion film on Si. (b) Ellipsometer reading of film thickness (black) response to relative humidity (red). (c) Measured film expansion for a change of 52-85 %RH as a function of film thickness. (d) Measured expansion of a 13 nm (ambient) film as RH is increased.

Petrina[182] observed a decrease in the refractive index and a significant increase in the expansion capabilities of Nafion with decreasing thickness for films below ∼50 nm. Using ellipsometery to measure the RI of the Nafion films used in this investigation

under ambient conditions (measured as 52 ± 2 nm for all thickness tests), similar results were produced, as shown in Fig. 7.3. Whilst many polymers show an increased ring-stacking for thinner spin-coated films,[233] Nafion is a random copolymer and so the reduction in thickness actually reduces what order it had due to phase segregation, leading to poor chain stacking and increasing the free volume of the films. This results in a lowering of the refractive index, a behaviour which will be key for accurately modelling the resonances of the film-coupled nanocubes throughout this chapter.

The reduction of structure in thinner films means that the matrix formed by the rigid fluorocarbon backbones becomes much weaker and thus thinner films are able to expand more freely. The expansion of films with ambient thicknesses between 5 and 35 nm when the RH changed from 52 - 85 % was examined using ellipsometry as shown in Fig. 7.4. In Fig. 7.4(b) the film can be seen to expand stepwise with the humidity. Figure 7.4(c) demonstrates that for a given RH shift, films thinner than around 30 nm swell an exponentially greater fraction with the reciprocal of their ambient thickness. This was not observed to produce lasting damage or inhibit the repeatability of experiments. For thicker films >100 nm, a further slight increase was seen and films were found to have an expansion of 15-18% for measured thicknesses of up to 366 nm. It is also interesting that the Nafion does not expand in a linear fashion, as shown in Fig. 7.4(d), but instead seems to expand only marginally until about 50 %RH and then much more rapidly. Petrina attributes the small expansions below 50 %RH to individual water-rich domain growths which are very limited by the matrix of hydrophobic backbones. Above 50 %RH these domains coalesce and cooperative effects of ionic groups overcome the mechanical resistance, leading to a reduced elastic modulus and greater expansions.

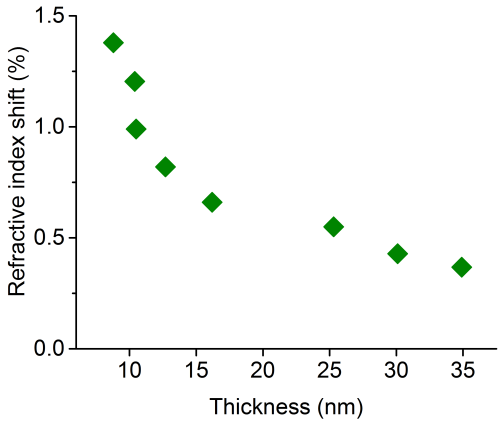

Figure 7.5: The refractive index shift of thin Nafion films as humidity is varied from 52-85% as measured by ellipsometry.

The refractive index decreases with expansion since the RI of water (1.33) is less than that of dry Nafion (1.35), the results in Fig. 7.5 show that the RI shift is greater for thinner films, which Petrina hypothesises is again due to their reduced structure allowing for greater water uptake. Petrina obtained almost identical results using SiO_2 on Si or Au substrates, and using different coating techniques, indicating that the swelling properties are more strongly linked with the morphology of the films than the surface chemistry for sub-50 nm films. Thus the use of ellipsometry data from films on Si substrates seems justified in this case, and using this data to define spacer properties in FDTD simulations produces a good agreement with theory throughout this chapter.

7.3 Tuning the fundamental mode

With a solid understanding of the properties of the spacer layer to hand, the next step is to investigate the tunability of the plasmon modes of the system through altering the spacer thickness. Lassiter et al[83] and Ciraci et al[159] have looked into aspects of this behaviour both experimentally and analytically, but as this investigation approaches the problem with different aims, and uses different materials and fabrication techniques, it is necessary to investigate the dependence on spacer thickness for the samples used before pursuing any sensing applications.

Figure 7.6(a) shows an FDTD simulation of the scattering spectra of a single 75 nm Ag NC with 10 nm RoC corners above an Ag sheet with varying thicknesses of Nafion spacer. The fundamental mode (i) manifests as a peak around 600 nm, which redshifts as the film thickness is decreased, due to an increase in the effective index within the cavity as discussed in section 3.4. There are a variety of other modes (ii),(iii) which can be excited in this system, which appear as shorter wavelengths peaks in the scattering spectra, but as these show a much weaker wavelength dependence on the spacer properties, they are of limited interest for this application. It has also been demonstrated that whilst the intensity of the E-field enhancements are affected, the structure and wavelength of the fundamental mode is insensitive to the angle and

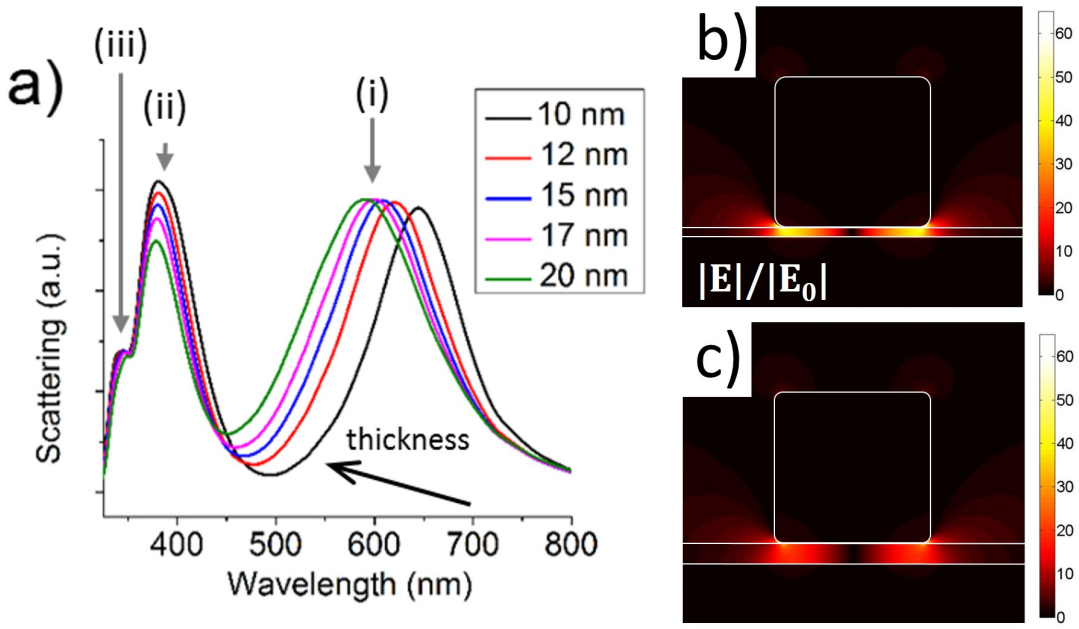

Figure 7.6: (a) FDTD simulation showing the wavelength shift of the principal mode as the thickness of the Nafion spacer is increased. (b),(c) Electric field at the fundamental mode resonance (i) for a 5 nm and a 10 nm spacer layer, highlighting the difference in coupling strength. In these simulations cube width is 75 nm, RoC = 10 nm and the RI of Nafion is taken as 1.35.

polarization of incident light except for very oblique angles.[83] As we are generally concerned with the only the resonance wavelengths here, normally incident radiation has been used to conserve processing time.

In Fig. 7.6(b)&(c) the electric field enhancement compared with the incident field is shown. It can clearly be seen that the electric field is strongly concentrated in the spacer layer, specifically around the corners where the charge separation is most significant. Doubling the film thickness from 5 nm in Fig. 7.6(b) to 10 nm in Fig. 7.6(c) can be seen to drastically reduce the electric field concentration, and hence the optical density of states in the spacer due to the weaker coupling between plasmons in the cube and the silver film.

The peak shifts predicted by FDTD simulations were compared with experimental results from NC's deposited upon silver sheets with six different thicknesses of Nafion beneath them. Figure 7.7(a) shows an image on the spectrograph CCD along with line traces for the three NC's under illumination. Differences in resonance wavelength can be attributed to the varying size and corner sharpness of the NC's and the surface

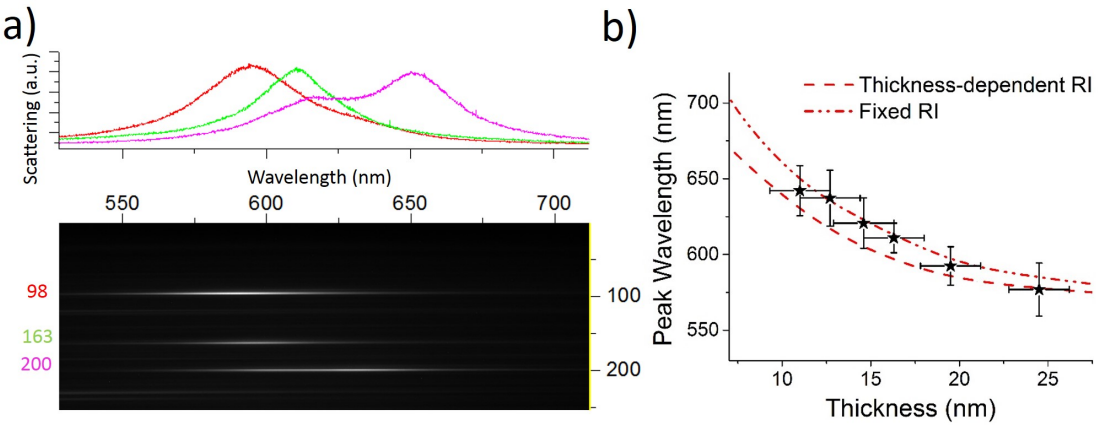

Figure 7.7: (a) Andor spectrograph CCD image and line traces of white light scattering from three NC's above a 16 nm Nafion spacer on Ag. (b) Plot showing simulated peak wavelength for a spacer RI fixed at 1.35 (dash-dot line) and one which varies with thickness (dashed line), compared to experimental dark-field scattering results (black stars) for 75 nm NC's on varying thicknesses of Nafion polymer.

roughness of the film.

Figure 7.3 shows how the actual refractive index of the film outside the cavity reduces with film thickness due to an increase in the void fraction in the Nafion, but this change is small compared to the change in effective index due to the increased density of states in the gap, as determined by the spacer thickness. Calculations using the cavity model described in section 3.4 predict a change from $n_{eff} = 2.6$ for a 25 nm gap to $n_{eff} = 3.9$ for a 11 nm gap, whereas the change in RI due to structural differences in thin Nafion films as measured using an ellipsometer only range from $n = 1.32$ for a 25 nm thick layer to $n = 1.26$ for an 11 nm layer.

This difference can still have an impact however: Fig. 7.7(b) shows simulated values of the resonance peak positions for spacers from 7-22 nm thick both in the case of a fixed spacer RI (at 1.35), and one which varies with thickness. Experimental results taken from dark-field scattering spectra from NC's above Nafion films from 11 - 25 nm, with 50 NC's in each sample are compared with the simulations. A clear reciprocal relationship between thickness and gradient is observed, with a strong redshifting of the peak for thinner films in line with an increasing effective index. A good agreement is seen between the experimental data and both sets of simulations, showing that the effect of changing thickness dominates over the reduced RI of thinner layers.

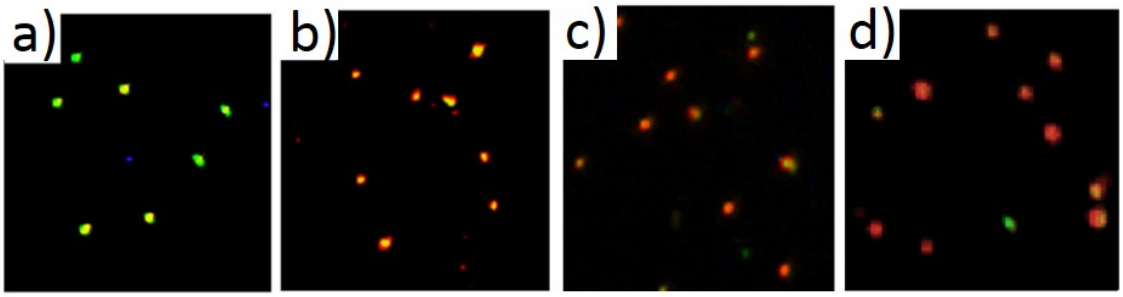

Figure 7.8: Dark-field colour CCD images of NC's above (a) 110, (b) 16, (c) 13 & (d) 11 nm Nafion films.

Uncertainty in the experimental data is due to the varying NC dimensions within the dataset and the surface roughness of the Nafion layer from the spin coating, both of which are extremely difficult to measure on a cube-by-cube basis. However, the average values agree well with the simulations. Techniques such as layer-by-layer or vapour deposition would allow access to thinner films and thus more sensitive devices. The slightly inferior fit of the RI-corrected curve is possibly due to the fact that the films measured in the ellipsometer were not the exact same as were used in the scattering experiments, although there is still good agreement within the bounds of experimental error.

The resonance shift is significant enough that it can be detected visually, as shown by Fig. 7.8(b)-(d), where white-light scattering from 11, 13 and 16 nm samples show a clear shift from a deep red to a yellowy orange as the film thickness increases. Also shown for contrast in Fig. 7.8(a) is a sample with a 110 nm film showing a peak in the green, demonstrating a resonance with barely any coupling between the cube and the metal sheet.

Agreement between simulation and experiment here demonstrates that the peak resonance is tunable through altering the thickness of the spacer layer using basic deposition techniques and that the thinner the spacer the more sensitive it is to thickness changes. As Nafion is known to expand and contract with humidity variations, this provides the basis for a new type of sensor.

7.4 Film-coupled nanocube humidity sensors

7.4.1 Measuring resonance shift

To demonstrate the sensitivity of the plasmon resonance to the surrounding humidity, 11 nm of Nafion was coated on to a silver sheet with NC's deposited above. The sample was placed inside a humidity chamber and the RH of the enclosed environment altered whilst under illumination from a white light source. Scattering from the particles was measured both spectroscopically and in image mode using the optical setup described in section 4.3.3.

Figure 7.9(a) shows marked redshifting of the peaks as the humidity increases and the spacer takes on water and expands. This process was found to be reversible and showed identical results after several repeats. This is in agreement with previous studies of Nafion films, which found them to be highly robust giving nearly identical results after 50 days usage.[215] This shift can be observed visually, and varying the RH from the lower range of our apparatus at 11 % RH, to the upper at 85 % RH, produces a noticeable shift from a deep red to a much brighter orange(Fig. 7.9(b)&(c)).

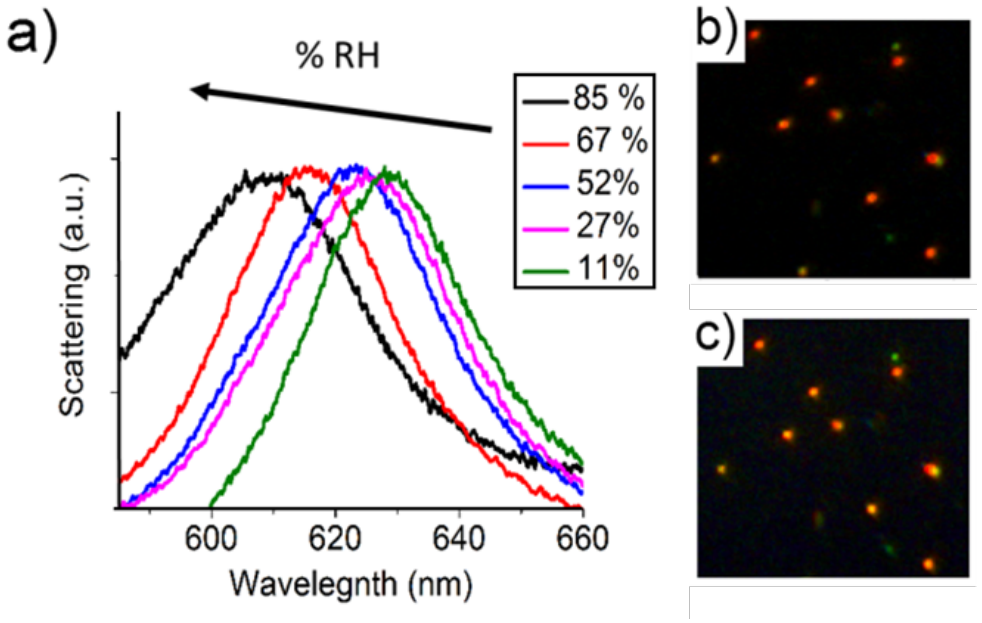

Figure 7.9: (a) Normalised experimental scattering spectra of a 75 nm Ag cube separated by a silver sheet by a 11 nm spacer under conditions varying from 11-85 % RH. (b),(c) Dark-field image of NC scattering under 11 % and 85 % RH respectively.

In Fig. 7.9(a) it can be seen that the peak shifts significantly more at higher humidities. Figure 7.10 shows that the expansion of a bare Nafion film and the shift of the resonance peak with increasing RH are closely related and that there are at least two regions of differing expansive behaviour for the Nafion. RH changes above ∼50% are seen to produce much greater expansions than for lower humidities, as discussed in section 7.2. In the rapid swelling regime above ∼50 %RH, both follow an approximately linear trend as shown by the fit line in Fig. 7.10. An analysis of the relation between RH and resonance wavelength in the region between 52-85 % RH found a linear fit to be a good approximation, with an average R^2 coefficient of determination of 0.98 ± 0.2. This region therefore is chosen to investigate the relationship between film thickness and peak shift and to determine the sensitivities of the system as displayed in Fig. 7.11.

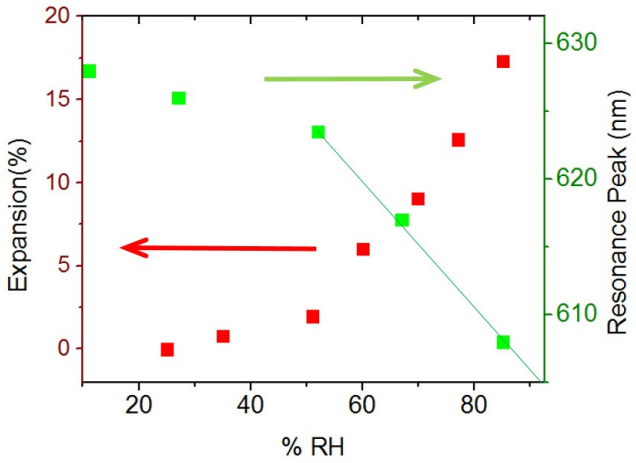

Figure 7.10: Resonance peak position vs RH compared with the % expansion of a bare Nafion film measured on the ellipsometer for a single NC above a 14 nm film. A fit line demonstrating the approximately linear relation between RH and peak position in the rapid swelling regime above ∼50 %RH is also shown.

Due to the reciprocal relationship between the mode effective index and spacer thickness, scattering from NC's above thinner films will show a much greater shift in resonance wavelength than thicker films for a given change in spacer thickness. Studies of the expansion of Nafion films when RH is varied from the ambient level of 52 % up to 85 % using an ellipsometer (Fig. 7.11(a)) show that thinner films also expand a much larger fraction of their initial width, following an approximately exponential relationship for the thicknesses considered. Whilst a quantative model of this relationship is lacking, as discussed in section 7.2 it has been suggested that this behaviour is due to a reduced ability of the Nafion in very thin films to phase segregate and form the rigid backbone structures that generally exist in thicker films and limit the water absorption capacity, leading to runaway expansion in very thin films.

The greater expansion of thinner films, and the increased thickness sensitivity of the

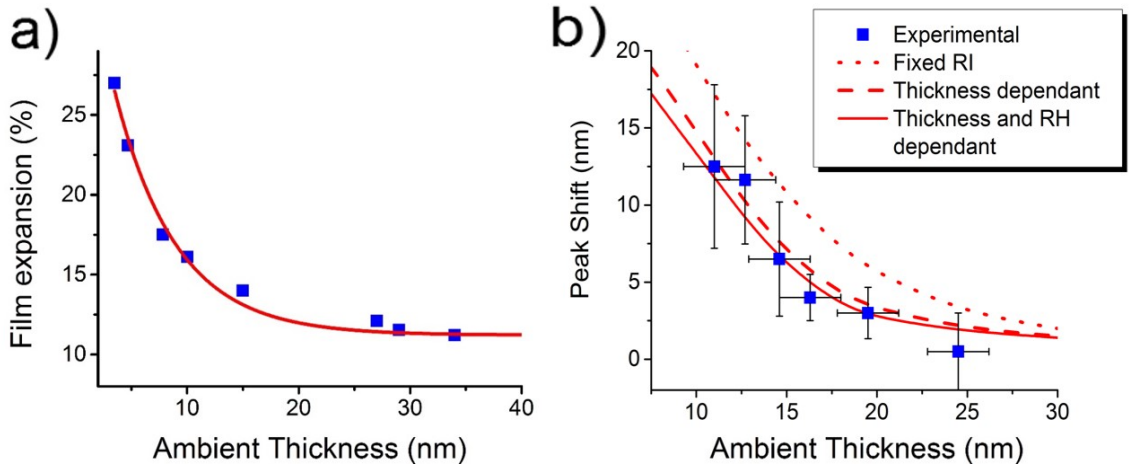

Figure 7.11: (a) Expansion as a percentage of ambient thickness for Nafion films as RH changes from 52-85 % as measured via ellipsometry and fitted to an exponential curve. (b) Experimental (blue squares) resonance shift for 75 nm, 10 nm RoC Ag NC's above a silver film with various spacer thicknesses, with simulated shifts based on the expansions in (a) where the RI of the films is fixed (dotted line), where it varies with thickness only (dashed line) and where it varies with thickness and RH (solid line).

resonance for thin spacers, mean that the much greater peak shifts for thinner films for a fixed change in RH shown in Fig. 7.11(b) are to be expected. Experimental data are plotted here against values from FDTD simulations taking the expansion fraction from an exponential fit to the ellipsometer data. When the RI dependence on film thickness is also taken into account, (from Fig. 7.3), the data and simulations demonstrate good agreement. When the small RI shift of the expanding Nafion shown in Fig. 7.5 is also included, the fit is slightly improved, although both cases agree well within error, once again showing that shifts in the RI of Nafion due to structural changes are less significant compared with the dependence of n_{eff} on spacer thickness, but must be taken into account to obtain a good fit. The good match between theory and experiment also indicates that the presence of the NC's above the film does not significantly affect water uptake.

There are significant sources of uncertainty, especially for thinner layers, again due to imperfect monodispersity in the cubes, surface roughness and the fact that any inhomogeneities in the ambient film will be accentuated through uneven expansion,[182] leading to larger error bars for thinner films. However, the trend is very much in line with the predictions of the leaky cavity model and our knowledge of Nafion expansion. Therefore the best sensors must use the thinnest producible films where the expansion

properties can be maintained.

The best average humidity sensitivity of this system is found to be 0.37 nm/% RH for NC's above a 11 nm film, with an average FWHM of 47 nm. Certain NC's show much higher sensitivities, of up to 0.57 nm/% RH, which is probably due to the individual NC's having sharper corners as will be discussed in section 7.5. This result is an improvement on previous systems based around plasmonic resonance shifts due changing polymer properties around single NP's, the best of which, by Wang et al, where gold nanorods were embedded in a nanowire made from a polymer with a refractive index that shifts with RH, produced a sensitivity of ∼0.19 nm/% RH.[81] This result in itself is an order of magnitude improvement on previous work using bare nanoparticles.[30]

7.4.2 Red laser measurements

Another approach to measuring RH change is to illuminate the sample with monochromatic light with a resonance chosen so that under ambient conditions the illumination wavelength falls approximately half way up the scattering peak. Using monochromatic light allows for faster and more precise observation of a signal change, and is a more scalable method as it does not require a bulky and expensive spectrometer to measure shifts.

FDTD simulations show that the scattering spectrum of a 75 nm, 10 nm RoC NC, is well approximated by a straight line (with an R^2 coefficient of determination of 0.989) within 75 % the distance from the FWHM to the peak, (Fig. 7.12(a)) meaning that careful tuning of the NC resonance is required for monochromatic sensing. Data from this approach can be seen in Fig. 7.12, where a 633 nm red laser was used to illuminate an individual NC. In this plot, an NC with an ambient peak of 653 nm was illuminated and the RH varied between 45-80%. The measured intensity of the NC scattering is well matched to the RH shifts recorded using a commercial electrochemical sensor, except for at an RH of 45 % where the response of the Nafion film to RH ceases to be linear, and an inferior response is to be expected in this region. This results justifies

the assumptions of linearity made in this chapter. Through examining the change in photon count in the SPAD with RH shift, this approach was found to produce a RH sensitivity of 0.09 dB/% RH, which again is a marked improvement on previous single NP humidity sensors.[81]

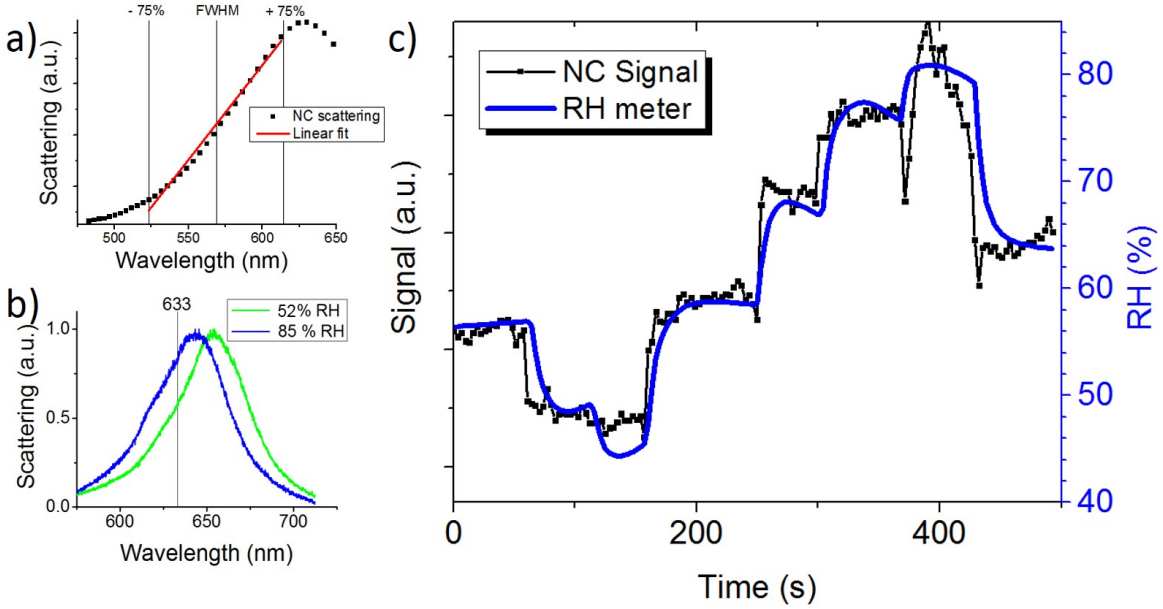

Figure 7.12: (a) FDTD simulation of scattering from an NC above a 12 nm spacer showing a linear fit to the slope of the peak. (b) White-light scattering spectra of a single NC above a 10.9 nm spacer under changing humidity conditions showing the position of the laser wavelength. (c) Scattering intensity of the NC illuminated by 633 nm laser emission as RH is varied, compared to the readings from a commercial electrochemical sensor.

Whilst this is an excellent result, there is still some noise in the system which must be accounted for to advance further. This can be studied by examining the laser power scattered by the NC's at a constant RH as shown in Figure 7.13(a). The Allan Variance technique[234] was used to analyse this signal to help determine the best averaging time to minimise noise. Allan variance examines the average difference between readings resampled across a given interval, and is an indicator of the stability of a signal as a function of the sampling time. It can be seen in Fig. 7.13 that the Allan variance is large for low interval times, reaches a minimum at ~3.2 s and then slowly climbs for larger values. This indicates that there is a significant amount of higher frequency noise, which can be reduced by increasing the sample time, but for larger sampling times low frequency drift of the system becomes a problem.

The re-sampled data is shown in Fig. 7.13(c), demonstrating a much cleaner signal but which still contains significant deviations on the ∼10 s timescale. Thus there can be said to be at least two significant sources of noise in the dataset. The high frequency noise was shown to have a signal to noise ratio that was found to not vary significantly with incident laser power. This indicates that the high frequency noise is unlikely to be the shot noise of the detector. It is most likely vibrational background from the lab building and the road nearby (typically around ∼10 Hz [235]). It was found that the use of the pinhole to select individual NC's made this system particularly sensitive to vibrations and this is something that might be improved in the future.

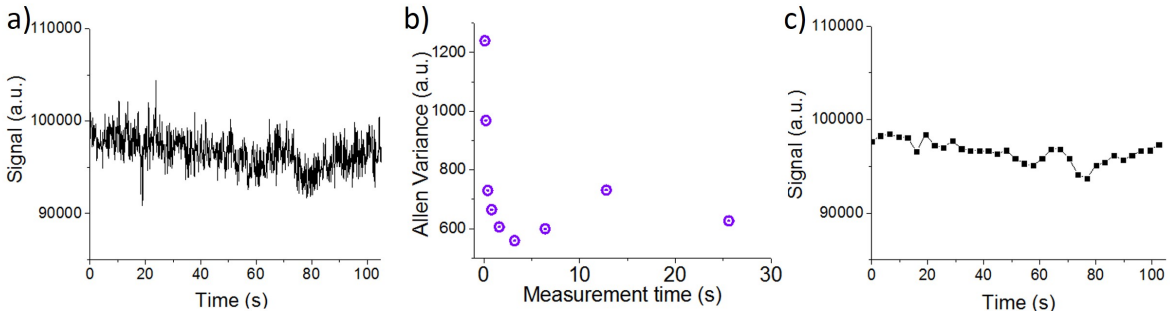

Figure 7.13: (a) Photon count from a single NC under 633 nm illumination at a constant RH as detected at the SPAD with a 0.1 s sampling time. (b) The Allan variance for the data in (a). (c) The signal in (a) with a sampling time of 3.2s.

The lower frequency variation is possibly due to the Nafion film. Satterfield et al. examined the mass change of Nafion membranes and found variations on a similar timescale which were attributed to polymer chain rearrangement and relaxation associated with polymer swelling.[236] If this is the case then this behaviour would fundamentally limit the resolution of this sensor and further investigation is required in this area.

The data shown in Fig. 7.12 is averaged over 3.2 s, and the r.m.s. variance of the data gives a noise-limited resolution for the sensor of 0.9 % RH, although this is dependent on the assumptions of linearity of both the film expansion and the slope of the NC scattering peak. These tests were repeated using three NP's in separate samples; the results from a separate NP are shown in Fig. 7.14 for completeness and to demonstrate the reproducability of the results.

It is likely that a similar result could be achieved with a much lower spec photodetector

than the SPCM used, which would reduce the cost of the setup and be beneficial for later device integration. The photon count for red laser scattering from a single NC is of the order of 10^6 photons/second, which relates to an incident power of $\sim$ 0.3 pW. Many basic photodiodes have noise-equivalent powers (NEP) in the fW/Hz$^{1/2}$ range[237, 238], which could therefore easily detect scattering from single NC's. The noise from the detector would surely be increased compared to the SPCM however, as the incident power would only be a couple orders of magnitude from the NEP, and so care would have to be taken to ensure that this noise did not surpass that due to vibrations and polymer processes, which would reduce the sensitivity of the setup.

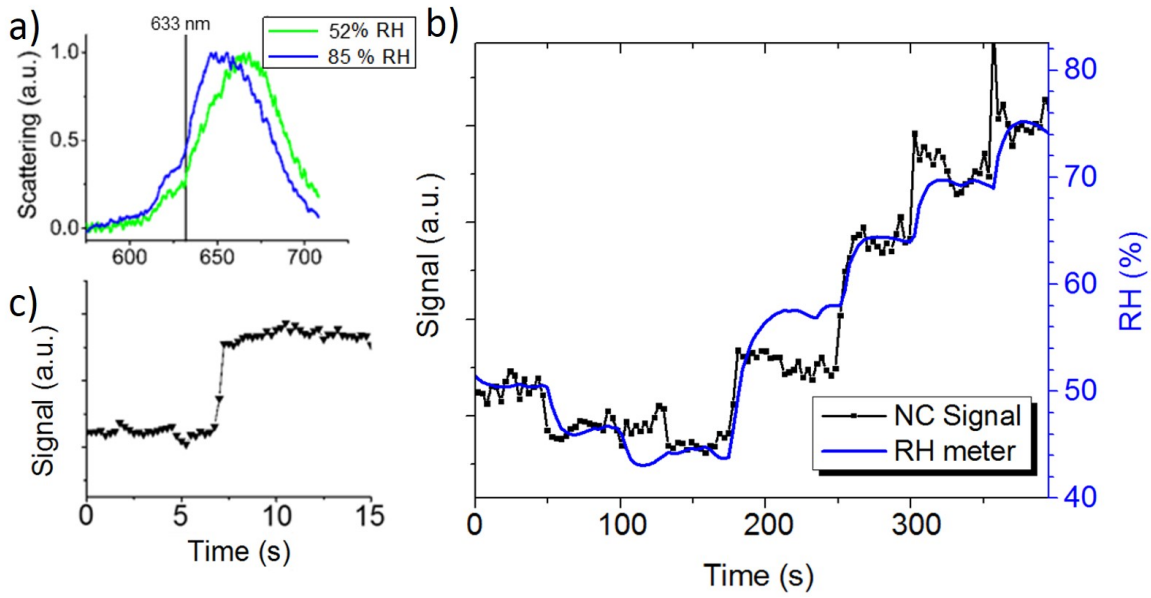

Figure 7.14: (a) White-light scattering spectra of peaks of a second NC under changing humidity conditions. (b) Scattering intensity of the NC above a 10.9 nm spacer illuminated by 633 nm laser emission as RH is varied, compared to the readings from a commercial electrochemical sensor. (c) Highlighting the fast response time of the NC system for a measured RH change of 50-67 %.

Determining an accurate value for the response time is difficult, as the scattering intensity has a tendency to sometimes 'overshoot' somewhat before settling when moist air is added, as can be observed around 300 and 350 s in Fig. 7.14(b). This has been attributed to unstable water diffusion processes in previous studies,[239] but could equally be related to uneven injection of gas into the chamber or small vibrations associated with gas injection. The initial response of the sensor to a change in humidity is extremely rapid, Fig. 7.14(c) shows a step with an RH shift of 17 % and the response

here for 90% of the signal change occurs across 200 ms, although this could be limited by the rate moist air is injected into the system and the actual maximum could be significantly higher. Nafion is known to have a quick response time to humidity change, Santos et al found a response of 242 ms for a 3% RH variation with 35 μm films,[215] and so this is not surprising, especially as these films are only 10-20 nm thick and the hydrophilic domain size is estimated to be 1-3 nm,[240] so there are very few layers of molecules that the water must diffuse through before it has completely permeated the polymer.

In many cases however, there is an overshoot settling time after the initial rapid shift, which occurs for both increases and decreases in RH. Taking this into account, the response time for a significant change in RH can be over an order of magnitude slower. This is still considerably faster than the electrochemical TSP01 sensor from Thorlabs used as a control, and is a comparable time to other sensor types in the literature.[241] This system shows the potential for truly rapid response times but further work to minimise noise and solve the overshoot problem is required before this can be achieved.

7.5 Increasing the sensitivity

It has been demonstrated that thinner spacers produce more sensitive detectors, due to the reciprocal relationship between thickness and the effective refractive index of the mode. It is also possible to tune the resonance and the sensitivity by changing the size and shape of the nanocubes.

7.5.1 Changing cube size

Figure 7.15(a) illustrates the effect of cube size on the scattering spectra of NC's with 10 nm corners above a spacer of 13 nm, while 7.15(b) shows that the cube size is more significant in determining the resonance conditions than spacer thickness for films between 5-20 nm, that are thin enough to allow strong near-field coupling across the

gap but thick enough to produce an even layer.[232] An increase in sensitivity for larger NC's can be seen in Fig. 7.15(c), but reducing the film thickness is shown to be a much more significant factor. For cubes above a 5 nm spacer, where the values for varying cube size are the most divergent, the sensitivity only changes by ∼8 nm/nm for a 40 nm change in size, whereas by changing spacer thickness, the sensitivity varies between 2 - 22 nm/nm for the values considered.

This behaviour fits well with an understanding of the patch antenna model. It has been stated that the resonance wavelength is dependent on both NC size and spacer thickness: $\lambda_{pk} \sim w$ and, loosely $\lambda_{pk} \sim 1/t$. The sensitivity of the peak to a change in spacer thickness, $S_t = d\lambda_{pk}/dt$ comes down to a derivative of the expression in eq. 3.15 and will therefore be extremely sensitive to thickness changes in thin films, whilst the size dependence remains linear. For tuning λ_{pk}, the greater range of sizes accessible for NC fabrication make it the more useful parameter, and as long as the films are very thin, this can be achieved without too much loss of sensitivity.

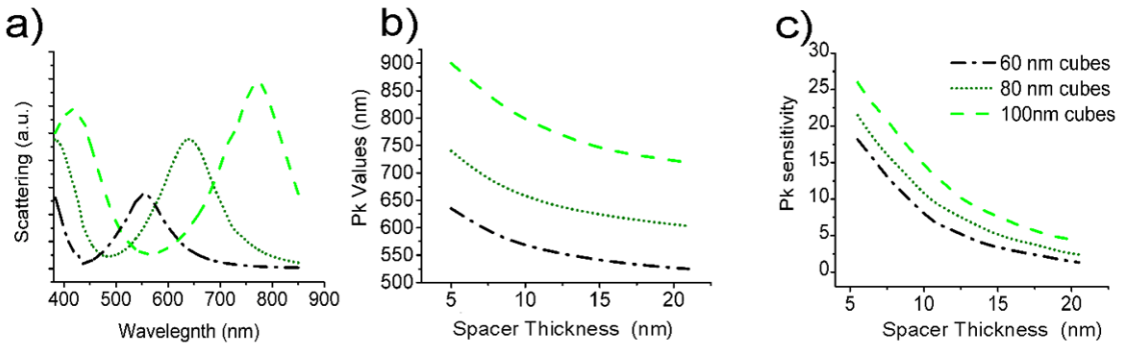

Figure 7.15: (a) FDTD simulation of the scattering spectra of Ag NC's with 10 nm RoC above a 12 nm film with a 2 nm PVP layer as the cube width is varied from 60-100 nm. (b) Plotting the resonance peaks of the NC's for spacer thicknesses from 5-22 nm. (c) Plotting the sensitivities of the peak position to a 1 nm increase in spacer thickness for 60-100 nm NC's.

7.5.2 Corner sharpness

The effect the corner radius of curvature has on the modes is more complex: Reducing the RoC produces both a pronounced redshift of the peak and a significant increase in the sensitivity. This behaviour is displayed in Fig. 7(a-c) for 75 nm NC's with a RoC from 1 nm to 37.5 nm (a spherical particle). Examining the electric field intensity of the

modes in Fig. 7(d-g), the points of greatest field strength in the film are separated by 73 nm for a NC with 1 nm corners, but only 53 nm for a cube with 10 nm RoC corners. It can be seen that the mode maxima is located close to the start of the corner curve, so even the slightest beveling appears to have a significant effect on the plasmon resonance. Bowen and Smith[161] found that defining an effective width for NC's with rounded corners was necessary to accurately model the scattering behaviour. We postulate that reduced λ_{pk} values for more rounded corners are due to scattering of the free elections that make up the surface plasmons at the start of the curved edges. This reduces the effective size of the plasmon cavity, which leads to resonances at shorter wavelengths than would be expected for a given size of cube.

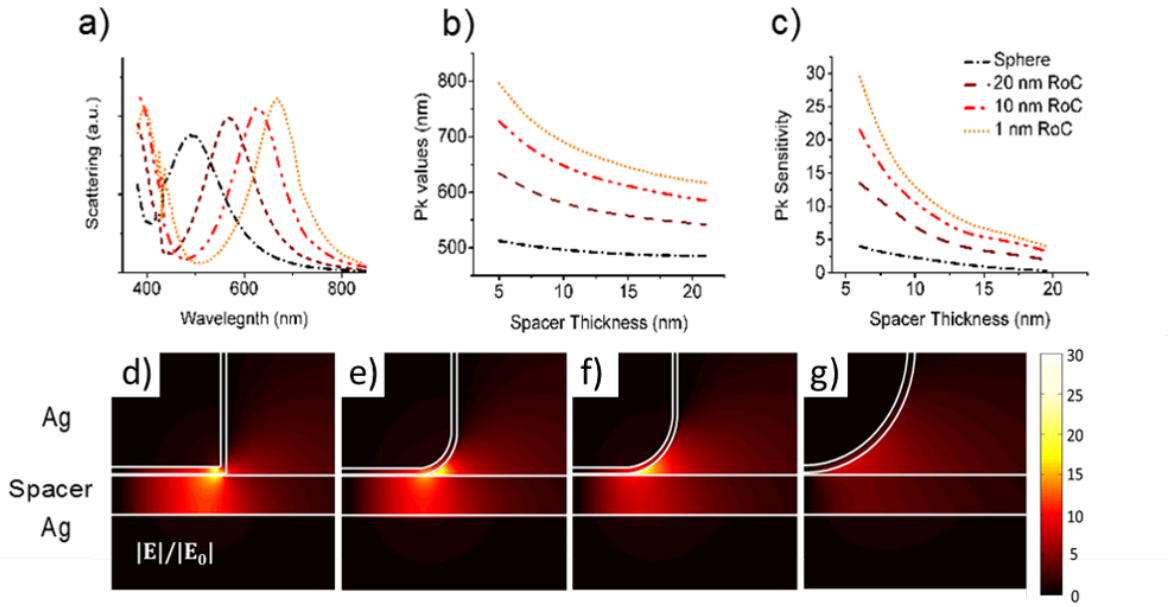

Figure 7.16: (a) FDTD simulation of the scattering spectra of 75 nm Ag NC's above a 12 nm film with a 2 nm PVP layer as the RoC of the corners is varied from 1-37.5 nm at which point the NC becomes a sphere. (b) Plotting the resonance peaks of the NC's for spacer thicknesses from 5-21 nm. (c) Plotting the sensitivities of the peak position to a 1 nm increase in spacer thickness. (d-g) Electric field intensity plots showing the mode geometry about the corners as the RoC increases from 1 nm (d) to 37.5 nm (g).

As well as scattering of the free electrons, the addition of the corners also promotes the formation of gap modes between the NC and the spacer. Here the evanescent field becomes highly concentrated in the small gap due to its low refractive index,[34] at the cost of the mode in the film, and the simulations show that for any corner rounding at all, by far the strongest field concentration is in this gap. In Fig. 7(d-g), as the RoC is

increased a clear reduction of the electric field strength in the spacer can be observed, meaning that the resonance conditions of this system will become less sensitive to what is happening in the film as RoC is increased, which is highly undesirable for a sensor which depends on the film response. For a doubling of the corner RoC from 10-20 nm for 75 nm NC's above a 13 nm film, a 40% decrease in the sensitivity is predicted.

This modelling suggests that the sensitivity of the device can be greatly enhanced. For a 100 nm NC, with 5 nm corners above a 5 nm Nafion film, parameters which have been shown to be achievable,[148, 232, 242] a peak sensitivity to thickness change of around 43 nm/nm is expected, which translates to a humidity sensitivity of 1.3 nm/% RH, over three times better than the best average from this investigation, and more than double the best individual result.

7.6 Future research

One of the features of using the nanocube patch antenna structure as a sensor is that the system is highly dependant on the properties of the spacer material. In this investigation we have seen that this can be both beneficial and problematic - Nafion is robust and relatively easy to work with and produces a significant expansion over a large humidity range. However, it also has a significant surface roughness, which would be a problem for creating a large-area metamaterial, although this could probably be improved through refining the fabrication process, and did not expand greatly for humidities below 50 %RH, which would hinder its use commercially. Through choosing a different spacer, many of these difficulties could be overcome and careful selection would enable the detection of a variety of other gases.

There is a wide array of materials which expand in response to a small concentration of gas, and it should be possible to construct nanocube sensors for several chemicals of commercial interest: Smith et al have shown that the expansion of Polystyrene can be used to detect ethanol vapour,[243] and other work from this group has demonstrated that PMMA can be functionalised to expand in response to other alcohols.[244]

Graphite oxide can also change its interlayer spacing by up to 20% when in contact with methanol.[245] There has been recent interest in detecting nitroaromatic explosive compounds using poly(4-vinylpyridine),[246–248] which has been shown to expand up to 40% in the presence of TNT and its analogues.[248] There are also further options with humidity detection, Nafion was used here as it is well studied and commercially available, but there are other, newer materials that are significantly more expansive: Si et al found that by grafting long-tail alkylbenzenes on to poly(para-phenylene disulfonic acid) a hybrid polymer was produced with expansions close to 50% of the original thickness when the humidity changed from 10-85 %RH,[249] which is more than 2.5 times the expansion seen with Nafion.

Many of these polymers have the potential for layer-by-layer deposition which would give much greater control over thickness than spin-coating, although there will surely be some challenges associated with the processing of individual materials to overcome. The potential exists for the creation of chip-scale arrays capable of detecting a whole smorgasbord of chemicals using the same basic structure. Whether these will be able to compete with some of the techniques described in section 7.1 and beyond remains to be seen, but the minute scale and ease of production for these devices is a cause for optimism of their future utility.

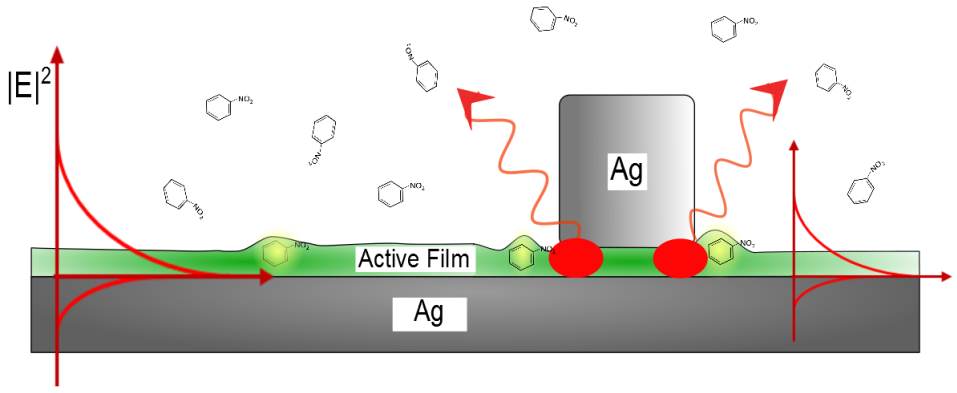

Figure 7.17: : Surface-plasmon excited NC modes: A surface plasmon wave is launched down a metal waveguide coated in a polymer which expands in response to gas stimulant. The plasmon excites resonant cavity modes between the cube and the metal, which scatter a portion of the light away, producing an attenuation of the detected wave strongly dependent on the gas concentration.

Further work could also focus on the integration of this sensor with a plasmonic circuit.

If a single NC was deposited above a metal waveguide with a <10 nm Nafion spacer, the humidity response of the system would result in a difference in the attenuation of a surface plasmon polariton sent down the waveguide. The general principle is displayed in Fig. 7.17. It has been shown that the electric field of the mode excited between a spherical Ag NP and a metal substrate excited by a surface plasmon wave can be up to two orders of magnitude greater than that of a SPP wave across a bare film[250] and thus it is anticipated that this system would be significantly more sensitive than detectors using a waveguide coated with solely a reactive polymer layer. Thus this system has the potential to operate as a fully integrated component in a plasmonic circuit, opening the way to a new class of on-chip nanoscale sensors.

7.7 Conclusions

Their extreme sensitivity to their dielectric surroundings, rapid response times and potential for integration with on-chip photonic circuitry make localised surface plasmons an ideal platform for optical sensing. In this chapter the operation of the nanocube patch antenna system as a gas sensor has been demonstrated for the first time using a Nafion spacer layer to measure relative humidity.

The response of very thin films of Nafion to changing RH was observed and discussed in the context of previous work. It was shown that using Nafion as the spacer layer between a silver nanocube and silver sheet produces a nanoscale humidity sensor with a fast response time and higher sensitivity than any other single-particle plasmonic humidity sensor recorded. An appropriate choice of alternative spacer materials would enable this structure to detect a variety of other gases. Sensitivities up to 0.57 nm/% RH are recorded, and a resolution of better than 1 % RH achieved. Sources of noise were analysed and their impact on device performance discussed. FDTD models predict that the sensitivity can be more than doubled from the recorded maximum through careful choice of structural parameters. This system is easy to fabricate and is an extremely scalable design - large arrays of NC's could be created to form a large-scale metamaterial, or kept as a single-NC system with a sub-wavelength footprint and the

potential to be integrated into plasmonic circuitry.

Chapter 8

Conclusions

This thesis presents a detailed description of the behaviour of plasmon modes excited within metal nanoparticles in thin dielectric films. The investigation was motivated by the growing interest in utilising the properties of localised surface plasmons to enhance the efficiencies of planar optical and optoelectronic devices, which increasingly involves their placement within a thin-film structure. It has been shown that this geometry can have a marked effect on the near and far field response of the excited surface plasmons. By careful tuning of the parameter space, control over the fraction of light coupled into the substrate, the directionality of light and the plasmon mode structure can be achieved. In the final chapter the nanocube patch antenna geometry was utilised to create a novel gas sensor, producing superior results to other single-particle designs and demonstrating a flexible platform with the potential to detect a variety of gases.

For the simplest case of spherical nanoparticles placed above a high index substrate, the addition of an overcoating film was shown to redshift the modes, alter the directional scattering of the dipolar mode, and remove unwanted backscatter, both from dipolar emission and from the Fano resonance created by interference between different mode orders. As long as the condition $n_{air} < n_{film} < n_{subs}$ was fulfilled, the forward scattering into the substrate was enhanced compared to the case of a particle at a bare interface through coupling of light to the quasi-waveguide modes of the layer, which then leak into the substrate whilst the RI gradient prevents leakage at the film-air boundary. The

interference of light in the film also resulted in increased large angle scattering under these conditions, leading to greater path lengths in the substrate.

A custom dark-field Fourier-space microscope was designed and built to experimentally measure the scattering from metal nanoparticles in thin-films for the first time. This setup allowed for the observation of scattering over a much greater angular range than previous designs due to the dual use of a rod mirror to direct light onto the sample and to act as a patch stop to block noise and specular reflection. The observed Fourier-space scattering patterns were found to agree well with simulations and confirmed the results of the FDTD study. Scattering into the substrate from individual silver nanowires at a bare interface and in a film was also observed for the first time using this apparatus.

Cubes and hemispheres were also investigated as these are easily fabricable nanoparticle geometries that have shown potential for light trapping applications. It was found that the mode hybridisation induced in flat sided particles due to image charges in the substrate was weakened due to the presence of the film reducing the refractive index gradient at the interface. However, the potentially negative effects of weaker substrate coupling due to the lessened RI gradient was mitigated by the interference properties of the film, and enhancements in wide-angle emission and forward scattering across the spectrum were still observed. If placed in a thin film where $n_{subs} < n_{film} < n_{air}$, it was suggested nanocubes could make a much greater contribution to plasmonic light trapping studies than they have to date and as they can be wet synthesised and easily processed they could prove an attractive alternative to hemispheres.

This part of this investigation provides a holistic description of the impact of a thin film structure on the behaviour of plasmonic nanoparticles and how this differs from their behaviour at a bare interface. This has not been investigated previously and has led to incorrect assumptions in some previous reports. It was shown that careful tuning of the parameter space can significantly enhance forward coupling, increase path length in a substrate and reduce short wavelegnth losses. This is achieved using nanoparticles that can be easily synthesised en masse and structures that can be produced using wet

synthesis methods, or other well-established planar deposition procedures without the need for any complex fabrication steps. This will be of interest to anyone looking to control the scattering properties of such particles within a thin-film device and would provide a good starting point for the design of light trapping structures. In order to keep the discussion general, there are aspects of planar devices that have not been discussed here such as the impact of the substrate thickness, absorption in the layers and the effect of metal back contacts. These effects would have to be considered individually for a given device design, but the findings of this report will be of general use for any thin-film planar structure. Further work here would focus on the integration of metal nanoparticles in a thin-film solar cell to attempt to produce significant absorption enhancements with a clear view as to the mechanisms responsible. A good starting choice would be an amorphous Silicon cell due to their stability and the absence of problematic TCO coverings.

One of the most interesting aspects of the thin film interference is that it can produce scattering into a tightly controlled angular range, which could be of significant use in nanoantenna applications. Scattering from silver nanowires in thin films was investigated and it was discovered that 55% of the scattered light could be emitted within 10 degrees of two, high-angle lobes, with the optimal results producing levels of confinement comparable to previous nanoantenna designs[134] if a very small angular range is desired, despite not being unidirectional. A thin-film geometry could also be used to improve the directionality of other antenna structures described in the literature in an easily fabricable manner. Further work would seek to excite the NW's using a photonic waveguide following the procedure of Arnaud et al[79] and explore the use of these findings for photonic circuitry.

A study was conducted to examine how much light could be emitted beyond the critical angle into the guided modes of the film-substrate structure. It was found that this could be maximised by careful tuning of the film height above the particle and that cubes were the best geometry for efficient scattering at large angles due to their large surface contact with the substrate allowing for enhanced near field coupling. The dependence of angular scattering on z_+, the height of the film above the particle centrewas the

basis of a suggestion for a novel sensing architecture where the overcoating film was made up of Nafion, a moisture sensitive polymer which expands with relative humidity. Initial experimental results showed that the scattering pattern from a NW in a Nafion film was significantly altered by the RH shift, proving the viability of the idea but simulations showed that due to the mechanics of thin film interference from dipolar scatterers, the invariance of large angle scattering with z_+ meant that this design can never beat a Fábry-Perot geometry.[215] It was suggested that this method could be of use in sensing applications where coupling from planar emission into a waveguide was required, or could be used to couple the modes of photonic waveguides to the farfield.

The final chapter focused on the geometry of a silver nanocube separated from a metal surface by a thin dielectric spacer and demonstrated the utilisation of this system as a subwavelength gas sensor for the first time. This method is attractive due to its ease of fabrication compared with other coupled NP techniques, and the ability to act as a subwavelength sensing element or a larger-scale metamaterial. Nafion was again chosen as the spacer and sensitivities of 0.57 nm/% RH were obtained from illumination with a white lamp and 0.09 dB/% RH from illumination using a red laser, which is an improvement on other single particle plasmon gas sensors. The sensor was found to have a fast response time but was limited by an "overshoot" problem possibly due to uneven diffusion in the ultrathin film. The noise-limited resolution of just below 1 % RH was comparable with other plasmonic designs, and appears to be limited by the material properties of Nafion. The Nafion polymer showed significantly greater expansion for RH values above $\sim$ 50 % and so sensitivity was reduced for low humidities. Whilst the experimental results agreed well with simulations, imperfect monodispersity in the cubes and surface roughness of the Nafion spacer led to large error bars, which would be problematic for the creation of a large-area metamaterial sensor, although these could be overcome via better NC synthesis and different deposition techniques. Routes to increased sensitivity were suggested following further simulations and it was postulated that the current sensitivities could be tripled through improving the fabrication using available materials and procedures.

Further work on this would focus on demonstrating these efficiency enhancements experimentally and also demonstrating the detection of other gases through careful choice of spacer layer. For example Poly(styrene-block-4-vinylpyridine) has been shown to expand significantly in the presence of nitroaromatic compounds used in explosives.[246, 247] It is suggested that the antenna modes could be excited by travelling surface plasmons instead of free space illumination, and so the integration of the patch antenna with a plasmonic waveguide as a stepping stone towards integration with optical circuitry would make an exciting extension to this research.

Chapter 9

Bibliography

[1] R. B. e. a. Konda, "Surface plasmon excitation via au nanoparticles in n-cdse/p-si heterojunction diodes.," *Appl. Phys. Lett.*, vol. 91, p. 191111, 2007.

[2] X. Gu, T. Qiu, W. Zhang, and P. Chu, "Light-emitting diodes enhanced by localized surface plasmon resonance," *Nanoscale Research Letters*, vol. 6, no. 1, p. 199, 2011.

[3] S.-H. Chuang, C.-S. Tsung, C.-H. Chen, S.-L. Ou, R.-H. Horng, C.-Y. Lin, and D.-S. Wuu, "Transparent conductive oxide films embedded with plasmonic nanostructure for light-emitting diode applications," *ACS Applied Materials & Interfaces*, vol. 7, no. 4, pp. 2546–2553, 2015. PMID: 25562635.

[4] H. Atwater and P. Polman, "Plasmonics for improved photovoltaic devices," *Nature Materials*, vol. 9, pp. 205–213, 2010.

[5] K. R. Catchpole and A. Polman, "Design principles for particle plasmon enhanced solar cells," *Appl. Phys. Lett.*, vol. 93, p. 191113, 2008.

[6] K. Catchpole and A. Polman, "Plasmonic solar cells," *Optics Express*, vol. 16, p. No. 26, 2008.

[7] S. Pillai, K. Cathpole, T. Trupke, and M. A. Green, "Surface plasmon enhanced solar cells," *J. Appl. Phys.*, vol. 101, p. 093105, 2007.

[8] Z. Sun, X. Zuo, and Y. Yang, "Role of surface metal nanoparticles on the absorption in solar cells," *Optics Express*, vol. 37, pp. 641–643, 2012.

[9] X. Zhao, C. Duan, Z. Liang, and H. Shen, "Preparation of self-assembled ag nanoparticles for effective light-trapping in crystalline silicon solar cells," *RSC Adv.*, vol. 4, pp. 13757–13763, 2014.

[10] H. Choi, W. T. Chen, and P. V. Kamat, "Know thy nano neighbor. plasmonic versus electron charging effects of metal nanoparticles in dye-sensitized solar cells," *ACS Nano*, vol. 6, no. 5, pp. 4418–4427, 2012.

[11] J. N. Anker, W. P. Hall, O. Lyandres, N. C. Shah, J. Zhao, and R. P. V. Duyne, "Biosensing with plasmonic nanosensors," *Nature Materials*, vol. 7, p. 422, 2008.

[12] B. Liedberg, C. Nylander, and I. LunstrÃűm, "Surface plasmon resonance for gas detection and biosensing," *Sensors and Actuators*, vol. 4, pp. 299 – 304, 1983.

[13] K. M. Mayer and J. H. Hafner, "Localized surface plasmon resonance sensors," *Chemical Reviews*, vol. 111, no. 6, pp. 3828–3857, 2011. PMID: 21648956.

[14] A. Tittl, H. Giessen, and N. Liu, "Plasmonic gas and chemical sensing," *Nanophotonics*, vol. 3, no. 3, pp. 157–180, 2014.

[15] S. A. Maier, *Plasmonics: Fundamentals and Applications*. Springer, 2007.

[16] W. C. Dror Sarid, *Modern Introduction to Surface Plasmons: Theory, Mathematica Modeling, and Applications*. Cambridge Univ Press, 2010.

[17] C. Dupas, M. Lahmani, and P. Houdy, eds., *Nanoscience: Nanotechnologies and Nanophysics*. Springer, 2006.

[18] I. Freestone, N. Meeks, M. Sax, and C. Higgitt, "The lycurgus cup âĂŤ a roman nanotechnology," *Gold Bulletin*, vol. 40, no. 4, pp. 270–277, 2007.

[19] K. Chang, "Tiny is beautiful: Translating 'nano' into practical," *NYTimes.com - Science*, 2005.

[20] H. Summers, ed., *Frontiers of Nanoscience, Volume 5 : Nanomedicine*. Elvesier, 2013.

[21] N.-I. Corp., "http://www.natural-immunogenics.com/,"

[22] Y. Kim, H. S. Suh, H. J. Cha, S. H. Kim, K. S. Jeong, and D. H. Kim, "A case of generalized argyria after ingestion of colloidal silver solution," *American Journal of Industrial Medicine*, vol. 52, no. 3, pp. 246–250, 2009.

[23] A. Cheak, *Alchemical Traditions: From Antiquity to the Avant-Garde*. Numen Books, 2013.

[24] G. Mie, "Contributions to the optics of turgid media, particularly solutions of colloidal metals," *Ann. Phys.*, vol. 25, p. 377, 1908.

[25] G. B. Matthew Pelton, *Introduction to Metal-Nanoparticle Plasmonics*. Wiley, 2013.

[26] D. Jeanmaire and R. V. Duyne, "Surface raman spectroelectrochemistry part i. heterocyclic, aromatic, and aliphatic amines adsorbed on the anodized silver electrode," *J. Electroanal. Chem.*, vol. 84, pp. 1–20, 1977.

[27] C. Hägglund, M. Zäch, G. Petersson, and B. Kasemo, "Electromagnetic coupling of light into a silicon solar cell by nanodisk plasmons," *Appl. Phys. Lett.*, vol. 92, p. 053110, 2008.

[28] H. Jans and Q. Huo, "Gold nanoparticle-enabled biological and chemical detection and analysis," *Chemical Society Reviews*, vol. 41, no. 7, pp. 2849–2866, 2012.

[29] T. Chung, S.-Y. Lee, E. Y. Song, H. Chun, and B. Lee, "Plasmonic nanostructures for nano-scale bio-sensing," *Sensors*, vol. 11, no. 11, pp. 10907–10929, 2011.

[30] J. M. Bingham, J. N. Anker, L. E. Kreno, and R. P. Van Duyne, "Gas sensing with high-resolution localized surface plasmon resonance spectroscopy," *Journal of the American Chemical Society*, vol. 132, no. 49, pp. 17358–17359, 2010.

[31] V. J. Sorger, R. F. Oulton, R.-M. Ma, and X. Zhang, "Toward integrated plasmonic circuits," *MRS bulletin*, vol. 37, no. 08, pp. 728–738, 2012.

[32] H. R. Stuart and D. G. Hall, "Absorption enhancement in silicon-on-insulator waveguides using metal island films," *Applied Physics Letters*, vol. 69, no. 16, pp. 2327–2329, 1996.

[33] J. Nelson, *The Physics of Solar Cells*. Imperial College Press, 2003.

[34] M. A. Green, "Enhanced evanescent mode light trapping in organic solar cells and other low index optoelectronic devices," *Progress in Photovoltaics: Research and Applications*, vol. 19, no. 4, pp. 473–477, 2011.

[35] D. Derkacs, S. H. Lim, P. Matheu, W. Mar, and E. T. Yu, "Improved performance of amorphous silicon solar cells via scattering from surface plasmon polaritons in nearby metallic nanoparticles," *Applied Physics Letters*, vol. 89, no. 9, p. 093103, 2006.

[36] A. J. Morfa and K. L. Rowlen, "Plasmon-enhanced solar energy conversion in organic bulk heterojunction photovoltaics," *Appl. Phys. Lett.*, vol. 92, p. 013504, 2008.

[37] F. J. Beck, A. Polman, and K. R. Catchpole, "Tunable light trapping for solar cells using localized surface plasmons," *J. Appl. Phys.*, vol. 105, p. 114310, 2009.

[38] F. J. Beck, S. Mokkapati, A. Polman, and K. R. Catchpole, "Asymmetry in photocurrent enhancement by plasmonic nanoparticle arrays located on the front or on the rear of solar cells," *Appl. Phys. Lett.*, vol. 96, p. 033113, 2010.

[39] S. Pillai, F. J. Beck, K. R. Catchpole, Z. Ouyang, and M. A. Green, "The effect of dielectric spacer thickness on surface plasmon enhanced solar cells for front and rear side depositions," *J. Appl. Phys.*, vol. 109, p. 073105, 2011.

[40] M. D. Brown, T. Suteewong, R. S. S. Kumar, V. DâĂŹInnocenzo, A. Petrozza, M. M. Lee, U. Wiesner, and H. J. Snaith, "Plasmonic dye-sensitized solar cells using core-shell metal-insulator nanoparticles," *Nano Letters*, vol. 11, no. 2, pp. 438–445, 2011.

[41] I. Diukman and M. Orenstein, "How front side plasmonic nanostructures enhance solar cell efficiency," *Solar Energy MAterials & Solar Cells*, vol. 95, pp. 2628–2631, 2011.

[42] A. Basch, F. Beck, T. Soderstrom, S. Varlamov, and K. Catchpole, "Combined plasmonic and dielectric rear reflectors for enhanced photocurrent in solar cells," *Appl. Phys. Lett.*, vol. 100, p. 243903, 2012.

[43] B. Chen, W. Zhang, X. Zhou, X. Huang, X. Zhao, H. Wang, M. Liu, Y. Lu, and S. Yang, "Surface plasmon enhancement of polymer solar cells by penetrating au/sio2 core/shell nanoparticles into all organic layers," *Nano Energy*, vol. 2, no. 5, pp. 906 – 915, 2013.

[44] W. Ren, G. Zhang, Y. Wu, H. Ding, Q. Shen, K. Zhang, J. Li, N. Pan, and X. Wang, "Broadband absorption enhancement achieved by optical layer mediated plasmonic solar cell," *Optics Express*, vol. 19, p. 27, 2011.

[45] A. Ji, Sangita, and R. P. Sharma, "A study of nanoellipsoids for thinthin-film plasmonic solar cell applications," *J. Phys. D: Appl. Phys.*, vol. 45, p. 275101, 2012.

[46] T. Temple, G. Mahanama, H. Reehal, and D. Bagnall, "Influence of localized surface plasmon excitation in silver nanoparticles on the performance of silicon solar cells," *Solar Energy Materials & Solar Cells*, vol. 93, pp. 1978–1985, 2009.

[47] domainb, "Cheap, efficient metal-based solar cells through plasmonics - see more at:," *domain-b.com*, 2015.

[48] J. Ayre, "New plasmonic polymer solar cells achieve record efficiency of 8.92

[49] D. Borghino, "Aluminum studs could boost the performance of any solar cell," *Gizmag*, 2013.

[50] K. Ding, T. Kirchartz, B. E. Pieters, C. Ulbrich, A. M. Ermes, S. Schicho, A. Lambertz, R. Carius, and U. Rau, "Characterization and simulation of a-si:h/c-si:h tandem solar cells," *Solar Energy Materials and Solar Cells*, vol. 95, no. 12, pp. 3318 – 3327, 2011.

[51] R. J. Veenkamp and W. N. Ye, "Plasmonic metal nanocubes for broadband light absorption enhancement in thin-film a-si solar cells," *Journal of Applied Physics*, vol. 115, no. 12, pp. –, 2014.

[52] F. Monestier, J.-J. Simona, P. Torchioa, L. Escoubasa, F. Florya, S. Bailly, R. de Bettignies, S. Guillerez, and C. Defranoux, "Modeling the short-circuit current density of polymer solar cells based on p3ht:pcbm blend," *Sol. Energy Mater. Sol. Cells*, pp. 1–6, 2006.

[53] H. Hoppe, N. S. Sariciftci, and D. Meissner, "Optical constants of conjugated polymer/fullerene based bulk-heterojunction organic solar cells," *Mol. Cryst. Liq. Cryst.*, vol. 385, 2002.

[54] H. Hoppe and N. S. Sariciftci, "Organic solar cells: An overview," *J. Mater. Res.*, vol. 19, p. 7, 2004.

[55] D. C. J. Neo, C. Cheng, S. D. Stranks, S. M. Fairclough, J. S. Kim, A. I. Kirkland, J. M. Smith, H. J. Snaith, H. E. Assender, and A. A. R. Watt, "Influence of shell thickness and surface passivation on pbs/cds core/shell colloidal quantum dot solar cells," *Chemistry of Materials*, vol. 26, no. 13, pp. 4004–4013, 2014.

[56] S. Willis, J. Dimmock, F. Tutu, H. Liu, M. Peinado, H. Assender, A. Watt, and I. Sellers, "Defect mediated extraction in inas/gaas quantum dot solar cells," *Solar Energy Materials and Solar Cells*, vol. 102, pp. 142 – 147, 2012. Organic, Dye sensitized and Innovative approaches for Photovoltaic Applications.

[57] A. Shah, P. Torres, R. Tscharner, N. Wyrsch, and H. Keppner, "Photovoltaic technology: the case for thin-film solar cells," *Science*, vol. 285, pp. 692–698, 1999.

[58] M. Schmid, R. Klenk, M. C. Lux-Steiner, M. Topic, and J. Krč, "Modeling plasmonic scattering combined with thin-film optics," *Nanotechnology*, vol. 22, p. 025204, 2010.

[59] X. Chen, B. Jia, J. K. Saha, B. Cai, N. Stokes, Q. Qiao, Y. Wang, Z. Shi, and M. Gu, "Broadband enhancement in thin-film amorphous silicon solar cells enabled by nucleated silver nanoparticles," *Nano Letters*, vol. 12 (5), pp. 2187–92, 2012.

[60] A. Paris, A. Vaccari, A. CalÃă Lesina, E. Serra, and L. Calliari, "Plasmonic scattering by metal nanoparticles for solar cells," *Plasmonics*, vol. 7, pp. 525–534, 2012.

[61] A. G. Curto, G. Volpe, T. H. Taminiau, M. P. Kreuzer, R. Quidant, and N. F. van Hulst, "Unidirectional emission of a quantum dot coupled to a nanoantenna," *Science*, vol. 329, no. 5994, pp. 930–933, 2010.

[62] A. G. Curto, T. H. Taminiau, G. Volpe, M. P. Kreuzer, R. Quidant, and N. F. van Hulst, "Multipolar radiation of quantum emitters with nanowire optical antennas," *Nat Commun*, vol. 4, p. 1750, 2013.

[63] R. S. Pavlov, A. G. Curto, and N. F. V. Hulst, "Log-periodic optical antennas with broadband directivity," *Optics Communications*, vol. 285, no. 16, pp. 3334 – 3340, 2012.

[64] A. V. Akimov, A. Mukherjee, C. L. Yu, D. E. Chang, A. S. Zibrov, P. R. Hemmer, H. Park, and M. D. Lukin, "Generation of single optical plasmons in metallic nanowires coupled to quantum dots," *Nature*, vol. 450, pp. 402–406, 2007.

[65] N. Hartmann, D. Piatkowski, R. Ciesielski, S. Mackowski, and A. Hartschuh, "Radiation channels close to a plasmonic nanowire visualized by back focal plane imaging," *ACS Nano*, no. 0, 2013.

[66] K. G. Lee, X. W. Chen, H. Eghlidi, P. Kukura, R. Lettow, A. Renn, and V. S. S. Götzinger, "A planar dielectric antenna for directional single-photon emission and near-unity collection efficiency," *Nature Photonics*, vol. 5, pp. 166–169, 2011.

[67] L. Luan, P. R. Sievert, W. Mu, Z. Hong, and J. B. Ketterson, "Highly directional fluorescence emission from dye molecules embedded in a dielectric layer adjacent to a silver film," *New Journal of Physics*, vol. 10, p. 073012, 2006.

[68] . Bionavis, "http://www.bionavis.com/products/."

[69] G. Lifesciences, "http://www.gelifesciences.com/webapp/wcs/stores/servlet/categorydisplay?categoryid=1171071&catalogid=10101&productid=&top=y&storeid=12751&langid=-1," 2015.

[70] I. Tokareva, S. Minko, J. H. Fendler, and E. Hutter, "Nanosensors based on responsive polymer brushes and gold nanoparticle enhanced transmission surface plasmon resonance spectroscopy," *Journal of the American Chemical Society*, vol. 126, no. 49, pp. 15950–15951, 2004. PMID: 15584714.

[71] Z. mei Qi, I. Honma, and H. Zhou, "Humidity sensor based on localized surface plasmon resonance of multilayer thin films of gold nanoparticles linked with myoglobin," *Opt. Lett.*, vol. 31, pp. 1854–1856, Jun 2006.

[72] T. Karakouz, A. Vaskevich, and I. Rubinstein, "Polymer-coated gold island films as localized plasmon transducers for gas sensingâĂă," *The Journal of Physical Chemistry B*, vol. 112, no. 46, pp. 14530–14538, 2008.

[73] D. Suzuki and H. Kawaguchi, "Hybrid microgels with reversibly changeable multiple brilliant color," *Langmuir*, vol. 22, no. 8, pp. 3818–3822, 2006. PMID: 16584261.

[74] K. Akamatsu, M. Shimada, T. Tsuruoka, H. Nawafune, S. Fujii, and Y. Nakamura, "Synthesis of ph-responsive nanocomposite microgels with size-controlled gold nanoparticles from ion-doped, lightly cross-linked poly(vinylpyridine)," *Langmuir*, vol. 26, no. 2, pp. 1254–1259, 2010. PMID: 19817404.

[75] P. Mohan, R. Shinta, J. Fujiwara, H. Takahashi, D. Mott, Y. Matsumura, G. Mizutani, K. Iwami, N. Umeda, and S. Maenosono, "Boehmite nanorod/gold nanoparticle nanocomposite film for an easy-to-use optical humidity sensor," *Sensors and Actuators B: Chemical*, vol. 168, pp. 429 – 435, 2012.

[76] P. J. Rivero, A. Urrutia, J. Goicoechea, and F. Arregui, "Optical fiber humidity sensors based on localized surface plasmon resonance (lspr) and lossy-mode resonance (lmr) in overlays loaded with silver nanoparticles," *Sensors and Actuators B: Chemical*, vol. 173, pp. 244 – 249, 2012.

[77] N. Liu, M. L. Tang, M. Hentschel, H. Giessen, and A. P. Alivisatos, "Nanoantenna-enhanced gas sensing in a single tailored nanofocus," *Nature materials*, vol. 10, no. 8, pp. 631–636, 2011.

[78] J. Nelayah, M. Kociak, O. Stéphan, F. J. G. de Abajo, M. Tencé, L. Henrard, D. Taverna, I. Pastoriza-Santos, L. M. Liz-Marzán, and C. Colliex, "Mapping surface plasmons on a single metallic nanoparticle," *Nature Physics*, vol. 3, no. 5, pp. 348–353, 2007.

[79] L. Arnaud, A. Bruyant, M. Renault, Y. Hadjar, R. Salas-Montiel, A. Apuzzo, G. Lérondel, A. Morand, P. Benech, E. L. Coarer, and S. Blaize, "Waveguide-coupled nanowire as an optical antenna," *J. Opt. Soc. Am. A*, vol. 30, pp. 2347–2355, Nov 2013.

[80] F. Gu, L. Zhang, X. Yin, and L. Tong, "Polymer single-nanowire optical sensors," *Nano Letters*, vol. 8, no. 9, pp. 2757–2761, 2008. PMID: 18672942.

[81] P. Wang, L. Zhang, Y. Xia, L. Tong, X. Xu, and Y. Ying, "Polymer nanofibers embedded with aligned gold nanorods: A new platform for plasmonic studies and optical sensing," *Nano Letters*, vol. 12, no. 6, pp. 3145–3150, 2012. PMID: 22582809.

[82] A. Moreau, C. Ciracì, J. J. Mock, R. T. Hill, Q. Wang, B. J. Wiley, A. Chilkoti, and D. R. Smith, "Controlled-reflectance surfaces with film-coupled colloidal nanoantennas," *Nature*, vol. 492, no. 7427, pp. 86–89, 2012.

[83] J. B. Lassiter, F. McGuire, J. J. Mock, C. CiracÃň, R. T. Hill, B. J. Wiley, A. Chilkoti, and D. R. Smith, "Plasmonic waveguide modes of film-coupled metallic nanocubes," *Nano Letters*, vol. 13, no. 12, pp. 5866–5872, 2013. PMID: 24199752.

[84] G. M. Akselrod, C. Argyropoulos, T. B. Hoang, C. Ciracì, C. Fang, J. Huang, D. R. Smith, and M. H. Mikkelsen, "Probing the mechanisms of large purcell enhancement in plasmonic nanoantennas," *Nature Photonics*, 2014.

[85] A. Rose, T. B. Hoang, F. McGuire, J. J. Mock, C. CiracÃň, D. R. Smith, and M. H. Mikkelsen, "Control of radiative processes using tunable plasmonic nanopatch antennas," *Nano Letters*, vol. 14, no. 8, pp. 4797–4802, 2014. PMID: 25020029.

[86] L. Yousefi and A. C. Foster, "Waveguide-fed optical hybrid plasmonic patch nano-antenna," *Opt. Express*, vol. 20, pp. 18326–18335, Jul 2012.

[87] C. F. Bohren and D. R. Huffman, *Absorption and Scattering of Light by Small Particles*. Wiley VCH, 1998.

[88] C. S. Kumar, ed., *UV-VIS and Photoluminescence Spectroscopy for Nanomaterials Characterization*. Springer, 2013.

[89] B. Ung and Y. Sheng, "Interference of surface waves in a metallic nanoslit," *Optics express*, vol. 15, no. 3, pp. 1182–1190, 2007.

[90] P. B. Johnson and R.-W. Christy, "Optical constants of the noble metals," *Physical Review B*, vol. 6, no. 12, p. 4370, 1972.

[91] M. V. U. Kriebig, *Optical Properties of Metal Clusters*. Springer, 1995.

[92] K. M., *The Scattering of Light and Other Electromagnetic Radiation*. New York Academic Press, 1969.

[93] C. Burrows, *Plasmonic resonances of metallic nanoparticles in arrays and in isolation*. PhD thesis, University of Exeter, 2010.

[94] A. Trugler, *Optical properties of metallic nanoparticles*. PhD thesis, KarlŰFranzensŰUniversität Graz, 2011.

[95] M. Garcia, "Surface plasmons in metallic nanoparticles: fundamentals and applications," *Journal of Physics D*, vol. 44, p. 283001, 2011.

[96] M. Meier and A. Wokaun, "Enhanced fields on large metal particles: dynamic depolarization," *Opt. Lett.*, vol. 8, pp. 581–583, Nov 1983.

[97] K. L. Kelly, E. Coronado, L. L. Zhao, and G. C. Schatz, "The optical properties of metal nanoparticles- the influence of size, shape, and dielectric environment," *The Journal of Physical Chemistry B*, vol. 107, pp. 668–677, 2003.

[98] X. Rui, W. Xiao-Dong, L. Wen, X. Xiao-Na, L. Yue-Qiang, J. An, Y. Fu-Hua, and L. Jin-Min, "Dielectric layer-dependent surface plasmon effect of metallic nanoparticles on silicon substrate," *Chinese Physics B*, vol. 21, no. 2, p. 025202, 2012.

[99] N. E. Motl, E. Ewusi-Annan, I. T. Sines, L. Jensen, and R. E. Schaak, "Au-cu alloy nanoparticles with tunable compositions and plasmonic properties: Experimental determination of composition and correlation with theory," *The Journal of Physical Chemistry C*, vol. 114, no. 45, pp. 19263–19269, 2010.

[100] L. Yang, X. Li, X. Tuo, T. T. V. Nguyen, X. Luo, and M. Hong, "Alloy nanoparticle plasmon resonance for enhancing broadband antireflection of laser-textured silicon surfaces," *Opt. Express*, vol. 19, pp. A657–A663, Jul 2011.

[101] P. C. Wu, T.-H. Kim, A. Suvorova, M. Giangregorio, M. Saunders, G. Bruno, A. S. Brown, and M. Losurdo, "Gamg alloy nanoparticles for broadly tunable plasmonics," *Small*, vol. 7, no. 6, pp. 751–756, 2011.

[102] A. Mooradian, "Photoluminescence of metals," *Phys. Rev. Lett.*, vol. 22, pp. 185–187, Feb 1969.

[103] J. Heber, "Surfing the wave," *Nature*, vol. 461, pp. 720–722, 2009.

[104] T. L. Temple and D. Bagnall, "Optical properties of gold and aluminium nanoparticles for silicon solar cell applications," *Journal of applied physics*, vol. 109, p. 084343, 2011.

[105] V. Kochergin, L. Neely, C.-Y. Jao, and H. D. Robinson, "Aluminum plasmonic nanostructures for improved absorption in organic photovoltaic devices," *Appl. Phys. Lett.*, vol. 98, p. 133305, 2011.

[106] H. Robinson, L. Neely, C.-Y. Jao, and V. Kochergin, "Enhanced absorption in organic semiconductors with embedded aluminum nanoparticles," in *Photonics Conference (PHO), 2011 IEEE*, pp. 863 –864, oct. 2011.

[107] B. Wu, X. Liu, T. Z. Oo, G. Xing, N. Mathews, and T. C. Sum, "Resonant aluminum nanodisk array for enhanced tunable broadband light trapping in ultrathin bulk heterojunction organic photovoltaic devices," *Plasmonics, Online First*, 2012.

[108] X. Fan, W. Zheng, and D. J. Singh, "Light scattering and surface plasmons on small spherical particles," *Light: Science & Applications*, vol. 3, no. 6, p. e179, 2014.

[109] F. Hao, Y. Sonnefraud, P. V. Dorpe, S. A. Maier, N. J. Halas, and P. Nordlander, "Symmetry breaking in plasmonic nanocavities: Subradiant lspr sensing and a tunable fano resonance," *Nano Letters*, vol. 8, no. 11, pp. 3983–3988, 2008. PMID: 18831572.

[110] B. Luk'yanchuk, N. I. Zheludev, S. A. Maier, N. J. Halas, P. Nordlander, H. Giessen, and C. T. Chong, "The fano resonance in plasmonic nanostructures and metamaterials," *Nature Materials*, vol. 9, pp. 707–715, 2010.

[111] B. Luk'yanchuk, M. Tribelsky, Z. Wang, Y. Zhou, M. Hong, L. Shi, and T. Chong, "Extraordinary scattering diagram for nanoparticles near plasmon resonance frequencies," *Applied Physics A: Materials Science & Processing*, vol. 89, pp. 259–264, 2007. 10.1007/s00339-007-4099-1.

[112] B. S. Luk'yanchuk, A. E. Miroshnichenko, and Y. S. Kivshar, "Fano resonances and topological optics: an interplay of far- and near-field interference phenomena," *Journal of Optics*, vol. 15, no. 7, p. 073001, 2013.

[113] L. J. Sherry, S.-H. Chang, G. C. Schatz, R. P. Van Duyne, B. J. Wiley, and Y. Xia, "Localized surface plasmon resonance spectroscopy of single silver nanocubes," *Nano Letters*, vol. 5, no. 10, pp. 2034–2038, 2005. PMID: 16218733.

[114] S. Zhang, K. Bao, N. J. Halas, H. Xu, and P. Nordlander, "Substrate-induced fano resonances of a plasmonic nanocube: A route to increased-sensitivity localized surface plasmon resonance sensors revealed," *Nano Letters*, vol. 11, no. 4, pp. 1657–1663, 2011. PMID: 21410217.

[115] H. Chen, L. Shao, T. Ming, K. C. Woo, Y. C. Man, J. Wang, and H.-Q. Lin, "Observation of the fano resonance in gold nanorods supported on high-dielectric-constant substrates," *ACS Nano*, vol. 5, no. 8, pp. 6754–6763, 2011. PMID: 21786827.

[116] R. Adato, A. A. Yanik, J. J. Amsden, D. L. Kaplan, F. G. Omenetto, M. K. Hong, S. Erramilli, and H. Altug, "Ultra-sensitive vibrational spectroscopy of protein monolayers with plasmonic nanoantenna arrays," *Proceedings of the National Academy of Sciences*, vol. 106, no. 46, pp. 19227–19232, 2009.

[117] F. J. Beck, E. Verhagen, S. Mokkapati, A. Polman, and K. R. Catchpole, "Resonant spp modes supported by discrete metal nanoparticles on high-index substrates," *Optics Express*, vol. 19, p. S2, 2011.

[118] S.-Y. Wang, D.-A. Borca-Tasciuc, and D. A. Kaminski, "The effect of particle vertical positioning on the absorption enhancement in plasmonic organic solar cells," *Journal of Applied Physics*, vol. 111, no. 12, p. 124301, 2012.

[119] H. Chen, X. Kou, Z. Yang, W. Ni, and J. Wang, "Shape-and size-dependent refractive index sensitivity of gold nanoparticles," *Langmuir*, vol. 24, no. 10, pp. 5233–5237, 2008.

[120] S.-W. Lee, S.-H. Chang, Y.-S. Lai, C.-C. Lin, C.-M. Tsai, Y.-C. Lee, J.-C. Chen, and C.-L. Huang, "Effect of temperature on the growth of silver nanoparticles using plasmon-mediated method under the irradiation of green leds," *Materials*, vol. 7, no. 12, p. 7781, 2014.

[121] J. J. Mock, M. Barbic, D. R. Smith, D. A. Schultz, and S. Schultz, "Shape effects in plasmon resonance of individual colloidal silver nanoparticles," *The Journal of Chemical Physics*, vol. 116, no. 15, pp. 6755–6759, 2002.

[122] V. Rivera, F. Ferri, and E. Marega, *Localized Surface Plasmon Resonances: Noble Metal Nanoparticle Interaction with Rare-Earth Ions, Plasmonics - Principles and Applications*. InTech, 2012.

[123] A. Sommerfeld, "New formulas for the electromagnetic field of a vertical electric dipole in a dielectric or conducting half-space near its horizontal interface," *Ann. Phys.*, vol. 81, p. 1135, 1926.

[124] S. Scheel, "Single-photon sourcesŮan introduction," *J. Mod. Opt.*, vol. 56, pp. 141–160, 2009.

[125] K. Koyama, M. Yoshita, M. Baba, T. Suemoto, and H. Akiyama, "High collection efficiency in fluorescence microscopy with a solid immersion lens," *Appl. Phys. Lett.*, vol. 75, pp. 1667–1669, 1999.

[126] T. L. Temple and D. M. Bagnall, "Broadband scattering of the solar spectrum by spherical metal nanoparticles," *Prog. Photovolt: Res. Appl.*, 2012.

[127] W. Lukosz, "Theory of optical-environment-dependent spontaneous-emission rates for emitters in thin layers," *Phys. Rev. B*, vol. 22, p. 3030Ű3038, 1980.

[128] W. Lukosz, "Light emission by multipole sources in thin layers. i. radiation patterns of electric and magnetic dipoles," *J. Opt. Soc. Am.*, vol. 71, pp. 744–754, Jun 1981.

[129] K. A. Neyts, "Simulation of light emission from thin-film microcavities," *J. Opt. Soc. Am.*, vol. 15, pp. No, 4, 1999.

[130] J. Dorfmüller, R. Vogelgesang, R. T. Weitz, C. Rockstuhl, C. Etrich, T. Pertsch, F. Lederer, and K. Kern, "Fabry-pÃĭrot resonances in one-dimensional plasmonic nanostructures," *Nano Letters*, vol. 9, no. 6, pp. 2372–2377, 2009. PMID: 19472987.

[131] Z. Li, K. Bao, Y. Fang, Y. Huang, P. Nordlander, and H. Xu, "Correlation between incident and emission polarization in nanowire surface plasmon waveguides," *Nano Letters*, vol. 10, no. 5, pp. 1831–1835, 2010. PMID: 20369891.

[132] L. Piazza, T. Lummen, E. Quinonez, Y. Murooka, B. Reed, B. Barwick, and F. Carbone, "Simultaneous observation of the quantization and the interference pattern of a plasmonic near-field," *Nature communications*, vol. 6, 2015.

[133] V. D. Miljković, T. Shegai, P. Johansson, and M. Käll, "Simulating light scattering from supported plasmonic nanowires," *Opt. Express*, vol. 20, pp. 10816–10826, May 2012.

[134] T. Shegai, V. D. Miljković, K. Bao, H. Xu, P. Nordlander, P. Johansson, and M. KaÌĹll, "Unidirectional broadband light emission from supported plasmonic nanowires," *Nano Letters*, vol. 11, no. 2, pp. 706–711, 2011.

[135] E. Zgraggen, O. Scholder, G.-L. Bona, F. Fontana, E. Alberti, A. Crespi, R. Osellame, T. Scharf, and I. Shorubalko, "Optical properties of waveguide-coupled nanowires for sub-wavelength detection in microspectrometer applications," *Journal of Optics*, vol. 17, no. 2, p. 025801, 2015.

[136] M.-G. Kang, T. Xu, H. J. Park, X. Luo, and L. J. Guo, "Efficiency enhancement of organic solar cells using transparent plasmonic ag nanowire electrodes," *Advanced Materials*, vol. 22, no. 39, pp. 4378–4383, 2010.

[137] I. Sersic, C. Tuambilangana, and A. F. Koenderink, "Fourier microscopy of single plasmonic scatterers," *New Journal of Physics*, vol. 13, no. 8, p. 083019, 2011.

[138] J. Dorfmüller, R. Vogelgesang, W. Khunsin, C. Rockstuhl, C. Etrich, and K. Kern, "Plasmonic nanowire antennas: Experiment, simulation, and theory," *Nano Letters*, vol. 10, no. 9, pp. 3596–3603, 2010. PMID: 20726567.

[139] O. Demichel, M. Petit, G. C. des Francs, A. Bouhelier, E. Hertz, F. Billard, F. de Fornel, and B. Cluzel, "Selective excitation of bright and dark plasmonic resonances of single gold nanorods," *Opt. Express*, vol. 22, pp. 15088–15096, Jun 2014.

[140] P. Torok, P. D. Higdon, and T. Wilson, "Theory for confocal and conventional microscopes imaging small dielectric scatterers," *Journal of Modern Optics*, vol. 45, no. 8, pp. 1681–1698, 1998.

[141] O. Haeberlé, M. Ammar, H. Furukawa, K. Tenjimbayashi, and P. Török, "Point spread function of optical microscopes imaging through stratified media," *Opt. Express*, vol. 11, pp. 2964–2969, Nov 2003.

[142] A. Powell, N. Hjerrild, A. Watt, H. Assender, and J. Smith, "Directional plasmonic scattering from metal nanoparticles in thin-film environments," *Applied Physics Letters*, vol. 104, no. 8, p. 081110, 2014.

[143] E. Prodan, C. Radloff, N. J. Halas, and P. Nordlander, "A hybridization model for the plasmon response of complex nanostructures," *Science*, vol. 302, no. 5644, pp. 419–422, 2003.

[144] Y. Wu and P. Nordlander, "Finite-difference time-domain modeling of the optical properties of nanoparticles near dielectric substrates," *The Journal of Physical Chemistry C*, vol. 114, no. 16, pp. 7302–7307, 2010.

[145] M. W. Knight, Y. Wu, J. B. Lassiter, P. Nordlander, and N. J. Halas, "Substrates matter: Influence of an adjacent dielectric on an individual plasmonic nanoparticle," *Nano Letters*, vol. 9, no. 5, pp. 2188–2192, 2009. PMID: 19361166.

[146] J. M. McMahon, Y. Wang, L. J. Sherry, R. P. Van Duyne, L. D. Marks, S. K. Gray, and G. C. Schatz, "Correlating the structure, optical spectra, and electrodynamics of single silver nanocubes," *The Journal of Physical Chemistry C*, vol. 113, no. 7, pp. 2731–2735, 2009.

[147] M. A. Mahmoud, M. Chamanzar, A. Adibi, and M. A. El-Sayed, "Effect of the dielectric constant of the surrounding medium and the substrate on the surface plasmon resonance spectrum and sensitivity factors of highly symmetric systems: silver nanocubes," *Journal of the American Chemical Society*, vol. 134, no. 14, pp. 6434–6442, 2012.

[148] Nanocomposix, "75 nm ag cubes." Website, 2015.

[149] H. Chen, T. Ming, S. Zhang, Z. Jin, B. Yang, and J. Wang, "Effect of the dielectric properties of substrates on the scattering patterns of gold nanorods," *Acs Nano*, vol. 5, no. 6, pp. 4865–4877, 2011.

[150] Y. Cheng, M. Wang, G. Borghs, and H. Chen, "Gold nanoparticle dimers for plasmon sensing," *Langmuir*, vol. 27, no. 12, pp. 7884–7891, 2011.

[151] K. Lee and J. Irudayaraj, "Correct spectral conversion between surface-enhanced raman and plasmon resonance scattering from nanoparticle dimers for single-molecule detection," *small*, vol. 9, no. 7, pp. 1106–1115, 2013.

[152] H. Chen, X. Kou, Z. Yang, W. Ni, and J. Wang, "Shape- and size-dependent refractive index sensitivity of gold nanoparticles," *Langmuir*, vol. 24, no. 10, pp. 5233–5237, 2008. PMID: 18435552.

[153] R. T. Hill, J. J. Mock, A. Hucknall, S. D. Wolter, N. M. Jokerst, D. R. Smith, and A. Chilkoti, "Plasmon ruler with angstrom length resolution," *ACS Nano*, vol. 6, no. 10, pp. 9237–9246, 2012. PMID: 22966857.

[154] R. T. Hill, K. M. Kozek, A. Hucknall, D. R. Smith, and A. Chilkoti, "Nanoparticle-film plasmon ruler interrogated with transmission visible spectroscopy," *ACS Photonics*, vol. 1, no. 10, pp. 974–984, 2014.

[155] J. J. Mock, R. T. Hill, A. Degiron, S. Zauscher, A. Chilkoti, and D. R. Smith, "Distance-dependent plasmon resonant coupling between a gold nanoparticle and gold film," *Nano Letters*, vol. 8, no. 8, pp. 2245–2252, 2008. PMID: 18590340.

[156] C. Tabor, R. Murali, M. Mahmoud, and M. A. El-Sayed, "On the use of plasmonic nanoparticle pairs as a plasmon ruler: The dependence of the near-field dipole plasmon coupling on nanoparticle size and shapeâĂă," *The Journal of Physical Chemistry A*, vol. 113, no. 10, pp. 1946–1953, 2009. PMID: 19090688.

[157] P. K. Jain, , and M. A. El-Sayed, "Surface plasmon coupling and its universal size scaling in metal nanostructures of complex geometry:âĂŁ elongated particle pairs and nanosphere trimers," *The Journal of Physical Chemistry C*, vol. 112, no. 13, pp. 4954–4960, 2008.

[158] "http://www.antenna-theory.com/antennas/patches/antenna.php."

[159] C. Cirací, J. Britt Lassiter, A. Moreau, and D. R. Smith, "Quasi-analytic study of scattering from optical plasmonic patch antennas," *Journal of Applied Physics*, vol. 114, no. 16, p. 163108, 2013.

[160] S. I. Bozhevolnyi and T. Søndergaard, "General properties of slow-plasmon resonant nanostructures: nano-antennas and resonators," *Opt. Express*, vol. 15, pp. 10869–10877, Aug 2007.

[161] P. T. Bowen and D. R. Smith, "Coupled-mode theory for film-coupled plasmonic nanocubes," *Phys. Rev. B*, vol. 90, p. 195402, Nov 2014.

[162] J. Henson, J. DiMaria, and R. Paiella, "Influence of nanoparticle height on plasmonic resonance wavelength and electromagnetic field enhancement in two-dimensional arrays," *Journal of Applied Physics*, vol. 106, no. 9, pp. –, 2009.

[163] Lumerical-Solutions, 2015. http://www.lumerical.com/.

[164] K. S. Yee *et al.*, "Numerical solution of initial boundary value problems involving maxwellŠs equations in isotropic media," *IEEE Trans. Antennas Propag*, vol. 14, no. 3, pp. 302–307, 1966.

[165] K. Kunz and R. Luebbers, *The Finite Difference Time Domain Method for Electromagnetics*, vol. Section 3.3. CRC Press, 1993.

[166] R. Courant, K. Friedrichs, and H. Lewy, "ÃIJber die partiellen differenzengleichungen der mathematischen physik," *Mathematische Annalen*, vol. 100, no. 1, pp. 32–74, 1928.

[167] S. D. Gedney, *Introduction to the Finite-Difference Time-Domain (FDTD) Method for Electromagnetics*. Morgan & Claypool, 2011.

[168] "Lumerical knowledge base : Cross sections and normalization," 2016.

[169] M. I. Mishchenko, J. W. Hovenier, and L. D. Travis, *Light Scattering by Nonspherical Particles: Theory, Measurements, and Applications*. Academic Press, 2000.

[170] Sigma-Aldritch, "Silver, dispersion," 2015. http://www.sigmaaldrich.com/catalog/product/aldrich/730777?lang=en/& region=GB.

[171] I. Rasband, W.S., "Imagej," 1997-2014. http://imagej.nih.gov/ij/.

[172] K. E. Korte, S. E. Skrabalak, and Y. Xia, "Rapid synthesis of silver nanowires through a cucl- or cucl2-mediated polyol process," *J. Mater. Chem.*, vol. 18, pp. 437–441, 2008.

[173] Dupont, "Ptfe af 1600," 2015. http://www2.dupont.com/Teflon_Industrial/en_US/products/product_by_name/teflon_af/.

[174] S.-J. Ding, P.-F. Wang, D. W. Zhang, J.-T. Wang, and W. W. Lee, "A novel structural amorphous fluoropolymer film with an ultra-low dielectric constant," *Materials Letters*, vol. 49, pp. 154–159, 2001.

[175] H. Zhang, S. Wang, and S. G. Weber, "Morphology and free volume of nanocomposite teflon {AF} 2400 films and their relationship to transport behavior," *Journal of Membrane Science*, vol. 443, pp. 115 – 123, 2013.

[176] 3M, "Fluorinert electronic liquid fc-40," 2015. http://multimedia.3m.com/mws/media/64888O/fluorinert-electronic-liquid-fc-40.pdf.

[177] Sigma-Aldritch, "Polyvinyl acetate," 2015. http://www.sigmaaldrich.com/catalog/product/aldrich/189480?lang=en/& region=GB.

[178] S. K. Dishari and M. A. Hickner, "Antiplasticization and water uptake of nafion thin films," *ACS Macro Letters*, vol. 1, no. 2, pp. 291–295, 2012.

[179] J. A. Dura, V. S. Murthi, M. Hartman, S. K. Satija, and C. F. Majkrzak, "Multilamellar interface structures in nafion," *Macromolecules*, vol. 42, no. 13, pp. 4769–4774, 2009.

[180] Y. Ogata, D. Kawaguchi, N. L. Yamada, and K. Tanaka, "Multistep thickening of nafion thin films in water," *ACS Macro Letters*, vol. 2, no. 10, pp. 856–859, 2013.

[181] M. A. Modestino, D. K. Paul, S. Dishari, S. A. Petrina, F. I. Allen, M. A. Hickner, K. Karan, R. A. Segalman, and A. Z. Weber, "Self-assembly and transport limitations in confined nafion films," *Macromolecules*, vol. 46, no. 3, pp. 867–873, 2013.

[182] S. A. Petrina, *Water sorption, visoelastic, and optical properties of thin Nafion films*. PhD thesis, Pennsylvania State University, 2013.

[183] Sigma-Aldritch, "Nafion perfluorinated resin solution," 2015. http://www.sigmaaldrich.com/catalog/product/aldrich/663492?lang=en/& region=GB.

[184] J. L. Elechiguerra, L. Larios-Lopez, C. Liu, D. Garcia-Gutierrez, A. Camacho-Bragado, and M. J. Yacaman, "Corrosion at the nanoscale: The case of silver nanowires and nanoparticles," *Chemistry of Materials*, vol. 17, no. 24, pp. 6042–6052, 2005.

[185] EdmundOptics, 2015. http://www.edmundoptics.co.uk/.

[186] C. Huang, A. Bouhelier, G. Colas des Francs, A. Bruyant, A. Guenot, E. Finot, J.-C. Weeber, and A. Dereux, "Gain, detuning, and radiation patterns of nanoparticle optical antennas," *Phys. Rev. B*, vol. 78, p. 155407, Oct 2008.

[187] T. Shegai, S. Chen, V. D. Miljković, G. Zengin, P. Johansson, and M. Käll, "A bimetallic nanoantenna for directional colour routing," *Nature communications*, vol. 2, p. 481, 2011.

[188] S. LOWENTHAL and D. JOYEUX, "Speckle removal by a slowly moving diffuser associated with a motionless diffuser," *J. Opt. Soc. Am.*, vol. 61, pp. 847–851, Jul 1971.

[189] S. Mahadevan, S. Halverson, L. Ramsey, and N. Venditti, "Suppression of fiber modal noise induced radial velocity errors for bright emission-line calibration sources," *The Astrophysical Journal*, vol. 786, no. 1, p. 18, 2014.

[190] ThorLabs, "2-channel compact usb temperature and humidity logger," 2015. http://www.thorlabs.de/newgrouppage9.cfm?objectgroup_ID=5884.

[191] A. Powell, A. Watt, H. Assender, and J. Smith, "Optimised plasmonic structures for thin-film solar cells," in *Poster presented at Photon12 IOP conference*, 2012.

[192] W. S. Wong and A. Salleo, *Flexible Electronics: Materials and Applications*. Springer, 2009.

[193] L. Yang, Y. Xuan, and J. Tan, "Efficient optical absorption in thin-film solar cells," *Optics Express*, vol. 19, p. S5, 2011.

[194] T. H. Taminiau, F. D. Stefani, F. B. Segerink, and N. F. van Hulst, "Optical antennas direct single-molecule emission," *Nature Photonics*, vol. 2, pp. 234–237, 2008.

[195] D. Duche, P. Torchioa, L. Escoubasa, F. Monestiera, J.-J. Simona, F. Floryb, and G. Mathiana, "Improving light absorbtion in organic solar cells by plasmonic contribution," *Solar Energy Materials and Solar Cells*, vol. 93, pp. 1377–1382, 2009.

[196] H. Shen, P. Bienstman, and B. Maes, "Plasmonic absorption enhancement in organic solar cells with thin active layers," *Journal of Applied Physics*, vol. 106, no. 7, p. 073109, 2009.

[197] M. Xue, L. Li, B. J. T. de Villers, H. Shen, J. Zhu, Z. Yu, A. Z. Stieg, Q. Pei, B. J. Schwartz, and K. L. Wang, "Charge-carrier dynamics in hybrid plasmonic organic solar cells with ag nanoparticles," *Applied Physics Letters*, vol. 98, no. 25, p. 253302, 2011.

[198] Z. Liu, J. Li, and F. Yan, "Package-free flexible organic solar cells with graphene top electrodes," *Advanced Materials*, vol. 25, no. 31, pp. 4296–4301, 2013.

[199] K. Kim, S.-H. Bae, C. T. Toh, H. Kim, J. H. Cho, D. Whang, T.-W. Lee, B. O?zyilmaz, and J.-H. Ahn, "Ultrathin organic solar cells with graphene doped by ferroelectric polarization," *ACS applied materials & interfaces*, vol. 6, no. 5, pp. 3299–3304, 2014.

[200] S. H. Lim, W. Mar, P. Matheu, D. Derkacs, and E. T. Yu, "Photocurrent spectroscopy of optical absorption enhancement in silicon photodiodes via scattering from surface plasmon polaritons in gold nanoparticles," *Journal of Applied Physics*, vol. 101, no. 10, p. 104309, 2007.

[201] S. Hayashi, D. V. Nesterenko, and Z. Sekkat, "Fano resonance and plasmon-induced transparency in waveguide-coupled surface plasmon resonance sensors," *Applied Physics Express*, vol. 8, no. 2, p. 022201, 2015.

[202] X. Sun, X. Chen, Z. Zhang, and Z. Sun, "Plasmon based antireflection coatings containing nanostructured ag and silica medium," *Applied Surface Science*, vol. 258, no. 8, pp. 3785 – 3788, 2012.

[203] R. S. Sesuraj, T. Temple, and D. M. Bagnall, "Tunable low-loss plasmonic mirror for diffuse optical scattering," *Applied Physics Express*, vol. 5, p. 125205, November 2012.

[204] K. M. A. El-Nour, A. Eftaiha, A. Al-Warthan, and R. A. Amma, "Synthesis and applications of silver nanoparticles," *Arabian Journal of Chemistry*, vol. 3, no. 3, pp. 135 – 140, 2010.

[205] R. Santbergen, T. L. Temple, R. Liang, A. H. M. Smets, R. A. C. M. M. van Swaaij, and M. Zeman, "Application of plasmonic silver island films in thin-film silicon solar cells," *Journal of Optics*, vol. 14, no. 2, p. 024010, 2012.

[206] S. Mokkapati, F. J. Beck, R. de Waele, A. Polman, and K. R. Catchpole, "Resonant nano-antennas for light trapping in plasmonic solar cells," *J. Phys. D: Appl. Phys*, vol. 44, p. 185101, 2011.

[207] F. Shan, T. Zhang, and S.-Q. Zhu, "Effects of ag nanocubes with different corner shape on the absorption enhancement in organic solar cells," *Journal of Nanomaterials*, 2014.

[208] N. S. King, Y. Li, C. Ayala-Orozco, T. Brannan, P. Nordlander, and N. J. Halas, "Angle- and spectral-dependent light scattering from plasmonic nanocups," *ACS Nano*, vol. 5, no. 9, pp. 7254–7262, 2011. PMID: 21761840.

[209] P. Spinelli, C. van Lare, E. Verhagen, and A. Polman, "Controlling fano lineshapes in plasmon-mediated light coupling into a substrate," *Opt. Express*, vol. 19, pp. A303–A311, May 2011.

[210] R. Lazzari and I. Simonsen, "Granfilm: a software for calculating thin-layer dielectric properties and fresnel coefficients," *Thin Solid Films*, vol. 419, no. 1âĂŞ2, pp. 124 – 136, 2002.

[211] L. Novotny and N. van Hulst, "Antennas for light," *Nature Photonics*, vol. 5, p. 83Ű90, 2011.

[212] T. Coenen, E. J. R. Vesseur, A. Polman, and A. F. Koenderink, "Directional emission from plasmonic yagiâĂŞuda antennas probed by angle-resolved cathodoluminescence spectroscopy," *Nano Letters*, vol. 11, no. 9, pp. 3779–3784, 2011. PMID: 21780758.

[213] www.fast.u psud.fr/ezyfit/, "Ezyfit - a free curve fitting toolbox for matlab."

[214] T. Kosako, Y. Kadoya, and H. F. Hofmann, "Directional control of light by a nano-optical yagiŰuda antenna," *Nature Photonics*, vol. 4, pp. 312–315, 2010.

[215] J. S. Santos, I. M. R. Jr., C. M. Cordeiro, C. R. Biazoli, C. A. Gouveia, and P. A. Jorge, "Characterisation of a nafion film by optical fibre fabryâĂŞperot interferometry for humidity sensing," *Sensors and Actuators B: Chemical*, vol. 196, no. 0, pp. 99 – 105, 2014.

[216] R. A. T. A. A. W. H. E. A. J. M. S. Alexander W. Powell, David M. Coles, "Plasmonic gas sensing using nanocube patch antennas," *Advanced Optical Materials*, 2016.

[217] S.-A. Jung, T.-S. Lee, W. M. Kim, K.-S. Lee, D. S. Jeong, W. S. Lee, and I. Kim, "Thickness dependence of surface plasmon resonance sensor response for metal ion detection," *Journal of Physics D: Applied Physics*, vol. 46, no. 31, p. 315104, 2013.

[218] S. Roh, T. Chung, and B. Lee, "Overview of the characteristics of micro-and nanostructured surface plasmon resonance sensors," *Sensors*, vol. 11, no. 2, pp. 1565–1588, 2011.

[219] J. K. Day, O. Neumann, N. K. Grady, and N. J. Halas, "Nanostructure-mediated launching and detection of 2d surface plasmons," *ACS nano*, vol. 4, no. 12, pp. 7566–7572, 2010.

[220] J. B. Khurgin, "How to deal with the loss in plasmonics and metamaterials," *Nature nanotechnology*, vol. 10, no. 1, pp. 2–6, 2015.

[221] C. Nylander, B. Liedberg, and T. Lind, "Gas detection by means of surface plasmon resonance," *Sensors and Actuators*, vol. 3, pp. 79 – 88, 1982.

[222] Y. Zhao, T. Walker, Y. B. Zheng, S.-C. S. Lin, A. A. Nawaz, B. Kiraly, J. Scott, and T. J. Huang, "Mechanically tuning the localized surface plasmon resonances of gold nanostructure arrays," *Journal of Nanotechnology in Engineering and Medicine*, vol. 3, no. 1, p. 011007, 2012.

[223] P. Vukusic, G. Bryan-Brown, and J. Sambles, "Surface plasmon resonance on gratings as a novel means for gas sensing," *Sensors and Actuators B: Chemical*, vol. 8, no. 2, pp. 155 – 160, 1992.

[224] M. Jory, P. Vukusic, and J. Sambles, "Development of a prototype gas sensor using surface plasmon resonance on gratings," *Sensors and Actuators B: Chemical*, vol. 17, no. 3, pp. 203 – 209, 1994.

[225] J. A. Gordon and R. W. Ziolkowski, "Investigating functionalized active coated nanoparticles for use in nano-sensing applications," *Opt. Express*, vol. 15, pp. 12562–12582, Oct 2007.

[226] J. A. Gordon and R. W. Ziolkowski, "The design and simulated performance of a coated nano-particle laser," *Opt. Express*, vol. 15, pp. 2622–2653, Mar 2007.

[227] R.-M. Ma, S. Ota, Y. Li, S. Yang, and X. Zhang, "Explosives detection in a lasing plasmon nanocavity," *Nature nanotechnology*, vol. 9, no. 8, pp. 600–604, 2014.

[228] Y.-Q. Chen and C.-J. Lu, "Surface modification on silver nanoparticles for enhancing vapor selectivity of localized surface plasmon resonance sensors," *Sensors and Actuators B: Chemical*, vol. 135, no. 2, pp. 492 – 498, 2009.

[229] J. B. Wright, K. N. Cicotte, G. Subramania, S. M. Dirk, and I. Brener, "Chemoselective gas sensors based on plasmonic nanohole arrays," *Opt. Mater. Express*, vol. 2, pp. 1655–1662, Nov 2012.

[230] N. C. Lindquist, M. A. Turner, and B. P. Heppner, "Template fabricated plasmonic nanoholes on analyte-sensitive substrates for real-time vapor sensing," *RSC Adv.*, vol. 4, pp. 15115–15121, 2014.

[231] F. Gu, H. Zeng, L. Tong, and S. Zhuang, "Metal single-nanowire plasmonic sensors," *Opt. Lett.*, vol. 38, pp. 1826–1828, Jun 2013.

[232] S. C. DeCaluwe, P. A. Kienzle, P. Bhargava, A. M. Baker, and J. A. Dura, "Phase segregation of sulfonate groups in nafion interface lamellae, quantified via neutron reflectometry fitting techniques for multi-layered structures," *Soft matter*, vol. 10, no. 31, pp. 5763–5776, 2014.

[233] S. Ata, K. Kuboyama, K. Ito, Y. Kobayashi, and T. Ougizawa, "Anisotropy and densification of polymer ultrathin films as seen by multi-angle ellipsometry and x-ray reflectometry," *Polymer*, vol. 53, no. 4, pp. 1028 – 1033, 2012.

[234] W. Demtröder, *Laser Spectroscopy: Vol. 1: Basic Principles*. Springer, 2008.

[235] , *Thorlabs Vibration Manual*. Thorlabs, 2015.

[236] M. B. Satterfieldă, , and J. B. Benziger*, "Non-fickian water vapor sorption dynamics by nafion membranes," *The Journal of Physical Chemistry B*, vol. 112, no. 12, pp. 3693–3704, 2008. PMID: 18314970.

[237] "Eotech silicon photodetectors," 2016.

[238] "Thorlabs photodetectors," 2016.

[239] N. Matsunaga, G. Sakai, K. Shimanoe, and N. Yamazoe, "Diffusion equation-based study of thin film semiconductor gas sensor-response transient," *Sensors and Actuators B: Chemical*, vol. 83, no. 1âĂŞ3, pp. 216 – 221, 2002. Selected Papers from {TRANSDUCERS} '01 {EUROSENSORS} {XV}.

[240] K. Malek, M. Eikerling, Q. Wang, Z. Liu, S. Otsuka, K. Akizuki, and M. Abe, "Nanophase segregation and water dynamics in hydrated nafion: Molecular modeling and experimental validation," *The Journal of Chemical Physics*, vol. 129, no. 20, p. 204702, 2008.

[241] A. Tripathy, S. Pramanik, J. Cho, J. Santhosh, and N. A. Abu Osman, "Role of morphological structure, doping, and coating of different materials in the sensing characteristics of humidity sensors," *Sensors*, vol. 14, no. 9, pp. 16343–16422, 2014.

[242] E. Martinsson, M. A. Otte, M. M. Shahjamali, B. Sepulveda, and D. Aili, "Substrate effect on the refractive index sensitivity of silver nanoparticles," *The Journal of Physical Chemistry C*, vol. 118, no. 42, pp. 24680–24687, 2014.

[243] C. L. C. Smith, J. U. Lind, C. H. Nielsen, M. B. Christiansen, T. Buss, N. B. Larsen, and A. Kristensen, "Enhanced transduction of photonic crystal dye lasers for gas sensing via swelling polymer film," *Opt. Lett.*, vol. 36, pp. 1392–1394, Apr 2011.

[244] H. Clevenson, P. Desjardins, X. Gan, and D. Englund, "High sensitivity gas sensor based on high-q suspended polymer photonic crystal nanocavity," *Applied Physics Letters*, vol. 104, no. 24, p. 241108, 2014.

[245] S. You, J. Yu, B. Sundqvist, L. A. Belyaeva, N. V. Avramenko, M. V. Korobov, and A. V. Talyzin, "Selective intercalation of graphite oxide by methanol in water/methanol mixtures," *The Journal of Physical Chemistry C*, vol. 117, no. 4, pp. 1963–1968, 2013.

[246] C. Petruczok, H. Choi, S. Y. Yang, A. Asatekin, K. Gleason, and G. Barbastathis, "Fabrication of a microscale device for detection of nitroaromatic compounds," *Microelectromechanical Systems, Journal of*, vol. 22, pp. 54–61, Feb 2013.

[247] M.-K. Bae, J. A. Lim, S. Kim, and Y.-W. Song, "Ultra-highly sensitive optical gas sensors based on chemomechanical polymer-incorporated fiber interferometer," *Opt. Express*, vol. 21, pp. 2018–2023, Jan 2013.

[248] W. E. Tenhaeff, L. D. McIntosh, and K. K. Gleason, "Synthesis of poly(4-vinylpyridine) thin films by initiated chemical vapor deposition (icvd) for selective nanotrench-based sensing of nitroaromatics," *Advanced Functional Materials*, vol. 20, no. 7, pp. 1144–1151, 2010.

[249] K. Si, D. Dong, R. Wycisk, and M. Litt, "Synthesis and characterization of poly (para-phenylene disulfonic acid), its copolymers and their n-alkylbenzene grafts as proton exchange membranes: high conductivity at low relative humidity," *Journal of Materials Chemistry*, vol. 22, no. 39, pp. 20907–20917, 2012.

[250] S. Zeng, X. Yu, W.-C. Law, Y. Zhang, R. Hu, X.-Q. Dinh, H.-P. Ho, and K.-T. Yong, "Size dependence of au np-enhanced surface plasmon resonance based on differential phase measurement," *Sensors and Actuators B: Chemical*, vol. 176, pp. 1128 – 1133, 2013.